PEOPLE'S DEMOCRATIC REPUBLIC OF ALGERIA
MINISTRY OF HIGHER EDUCATION AND SCIENTIFIC RESEARCH
UNIVERSITY OF 20 AOUT 1955 SKIKDA
FACULTY OF SCIENCES
DEPARTMENT OF PHYSICS

Doctoral Thesis in Science

Transition metal nitrides: synthesis, structure and energy storage

Presented by Djahida KERDOUD

Submitted in fulfilment of the requirements for the
Degree of Doctor of Physics
In Materials sciences

Jury members:

Chair	A. N. KABIR	Professor - University of Skikda
Examiner	C. BOUDERN	Professor - University of Constantine 1
Examiner	F. MERICHE	Professor - University of Jijel
Examiner	Z. SETIFI	Lecturer A - University of Skikda
Supervisor	N. BOUSSOUF	Professor - University Centre of Mila
Co-supervisor	C. BENHAMIDECHE	Professor - University of Skikda

Defended on December 2022

Dedicated to my parents

Mebarek KERDOUD

&

Fatima MERIKHI

Acknowledgements

It is my great pleasure that I am in a position to express my deep gratitude to some persons without their help the present research work could have not taken final shape.

At the outset, I would like to thank my supervisor Prof. Nora Boussouf and co-supervisor Prof. Chahrazed Benhamideche for their guidance at different stages of my thesis work.

I thank sincerely my government for the seven months PNE scholarship of the academic year 2019-2020, as it has helped me a lot to complete my research work smoothly and makes my goals that much.

I would like to express my cordial gratitude to Prof. Duncan H. Gregory for offering me the possibility to work in his research group during my research placement at University of Glasgow, and for making all the necessary materials and equipment I needed for my experimental work available, and especially for providing GSAS, the Rietveld software for my use. It is his immense commitment and desire to innovate that has often proven an inspiration to me in pursuit of my research work.

I am very much thankful to the University of Glasgow for giving me permission to do research work in the department of Chemistry, and for providing their facilities such as XRD, SEM, DR-UV-Vis and thermal analysis.

Special thanks are extended to all the members in the C3-13 lab at University of Glasgow, who have been there for support especially during initial stage, and for making the lab an enjoyable place to work.

I owe my gratitude to Dr. Faouzia Benkafada from university of Constantine, for the many fruitful discussions and argument I have had with her, which have helped shape my understanding of science and appreciation.

My gratitude goes also to all the members of the jury who accepted to examine and evaluate my work, particularly Pr. A. N. Kabir from university of Skikda, Pr. C. Boudern from university of Constantine 1, Pr. F. Meriche from university of Jijel and Mr. Z. Setifi, lecturer at university of Skikda.

Last but not the least, I would like to thank my parents for their blessings and support throughout the length of my career.

Abstract

The work presented in this thesis covers the investigation of different nitride materials. A variety of synthetic routes were performed in the preparation of transition metal nitrides of the composition Mn_4N, NbN, Mo_2N, TaN and ZrN. An important part has been devoted to the binary nitrides Li_3N and Mg_3N_2. The experimental work was focused on determining the optimum conditions of synthesis and the development of a general procedure to afford the desired material, and the in-depth study of the changes in crystal structure by applying the X-ray powder diffraction. The structure of the prepared nitride materials has been characterised by the Rietveld's X-ray whole profile fitting structure refinement method. Analysis of PXRD data may yield some useful information about phases present and their relative quantities in order to estimate the samples purity. Further, by the process of indexing diffraction data, unit cell parameters, atomic positions, crystal systems and cell symmetry for samples can be determined and refined. The effects of the synthetic parameters on the structural properties of synthesised nitrides have been described. Diffuse reflectance UV-Vis measurements were performed for band gap calculation. Thermal analysis TGA/DTA measurements under argon gas and scanning electron microscopy were only employed for some of the prepared nitrides.

Keywords: Transition metal nitrides, Li_3N, Mg_3N_2, X-ray powder diffraction, Rietveld refinement, band gap.

Résumé : « Nitrures de métaux de transition : synthèse, structure et stockage de l'énergie »

Le travail présenté dans cette thèse porte sur l'étude de différents matériaux à base de nitrures. Diverses méthodes de synthèse ont été employées dans la préparation de nitrures de métaux de transition de composition Mn_4N, NbN, Mo_2N, TaN et ZrN. Une partie importante a été consacrée aux nitrures binaires Li_3N et Mg_3N_2. Le travail expérimental a été basé sur la détermination des conditions optimales de synthèse et le développement d'une procédure expérimentale générale pour obtenir le matériau souhaité, et l'étude approfondie des changements de structure cristalline en utilisant la diffraction des rayons X. La structure des matériaux à base de nitrures préparés a été caractérisée par la méthode d'affinement Rietveld qui permet d'ajuster directement le profil global du diagramme de diffraction expérimental. L'analyse des données de diffraction des rayons X peut fournir des informations utiles sur les phases présentes et leurs quantités en pourcentage afin d'estimer la pureté des échantillons. En outre, par le processus d'indexation des données de diffraction, les paramètres de maille, positions atomiques, les systèmes cristallins et la symétrie peuvent être déterminés et affinés. Les effets des paramètres de synthèse ont été décrits. La Spectroscopie en réflectance diffuse (UV-Vis SRD) est utilisée pour calculer la bande interdite. Les mesures d'analyse thermique ATG/ATD sous gaz d'argon et la microscopie électronique à balayage (MEB) n'ont été utilisées que pour certains des nitrures préparés.

Mots clés : Nitrures de métaux de transition, Li_3N, Mg_3N_2, diffraction des rayons X, Affinement Rietveld, bande interdite.

ملخص : « نيتريدات المعادن الإنتقالية : التحضير، البنية و تخزين الطاقة »

يركز العمل المقدم في هذه الأطروحة على دراسة مختلف مواد النيتريدات. لقد تم استخدام طرق مختلفة في تحضير نيتريدات المعادن الإنتقالية ذات الصيغة: Mn_4N، NbN، Mo_2N، TaN و ZrN. كما تم تخصيص جزء مهم لتحضير النيتريديين الثنائيين Li_3N و Mg_3N_2. لقد تم التركيز في العمل التجريبي على تحديد الظروف المثلى للتحضير وتطوير الطريقة لذلك للحصول في الأخير على المركب المراد تشكيله وإنجاز دراسة معمقة للتغيرات البنيوية عن طريق حيود الأشعة السينية، أين سمحت طريقة ريتفالد بإعطاء معلومات حول أنواع الشوائب التي يمكن أن تتواجد في المركب، مع تحديد نسبها المئوية من أجل تقدير نقاوة المركب التي تم تحضيره. إن تحليل معلومات الأشعة السينية بطريقة ريتفالد يزودنا أيضا بنوع الشبكة البلورية، مواقع الذرات، الأنظمة البلورية والتماثل. تأثير الشروط التجريبية المستعملة تم وصفه، والتحليل الضوئي الإنعكاسي المنتشر تم توظيفه لحساب الفجوة النطاقية. أما قياسات التحليل الوزني الحراري والتحليل الحراري التفاضلي والمسح المجهري الإلكتروني استخدمت فقط لبعض النيتريدات.

الكلمات الدالة: النيتريدات، Li_3N، Mg_3N_2، حيود الأشعة السينية، طريقة ريتفالد، الفجوة النطاقية.

List of figures

List of tables

List of abbreviations

fcc :	Face centred cubic
hcp :	Hexagonal close packed
bcc :	Body centred cubic
orth	Orthorhombic
NH_3 :	Ammonia
$ZrCl_4$:	Zirconium tetrachloride
Ar :	Argon
NH_4Cl :	Ammonium chloride
MoO_3 :	Molybdenum trioxide
CH_4 :	Methane
$TaCl_5$:	Tantalum halide
Al_2O_3 :	Alumina
$BaSO_4$:	Barium sulphate
Ca. :	About or approximately
Sccm :	Standard cubic centimeters per minute (flow measurement), cm^3/min
ppm :	Parts per million (mg/l)
Oe :	Th oersted is the unit of the magnetic field H in the cm.g.s
PXD :	Powder X-ray diffraction
NMR :	Nuclear magnetic resonance spectroscopy
STA :	Simultaneous thermal analysis
TG :	Thermogravimetric analysis
DTA :	Differential thermal analysis
SEM :	Scanning electron microscopy
EDX :	Energy dispersive X-ray
DR-UV-Vis :	Diffusive reflectance ultraviolet and visible
UV-Vis :	Ultraviolet and visible
Eg :	Energy gap
ICSD :	Inorganic crystal structure database

ICDD PDF :	International centre for diffraction data powder diffraction file database
PDF :	Powder diffraction file database
COSSH :	Control of substances hazardous to health
GSAS :	General structure analysis system
EXPGUI :	Graphical user interface (GUI) editor for GSAS experiment (.EXP)
R_P :	R-profile
R_{WP} :	R-weighed profile
esd :	Estimated standard deviation
U_{iso} :	Measures the mean square displacement amplitude of the atom averaged over all directions in GSAS
a, b, c :	Cell parameters
x, y, z :	Atomic parameters
χ^2 :	Goodness of fit
COD :	Calculated, observed and difference plots

Table of Contents

General introduction

Significant and rapid progress in nitride chemistry has been made over the last decade or so because of their technological importance with improved classification and development of new synthetic routes leading to new nitride materials. Unlike oxide materials, which have been extensively studied, advances in nitrides area have been fundamental yet, there are relatively few nitrides compounds reported [1, 2, 3, 4, 5]. Despite this much of pioneering work in this area was actually performed back in 1920's and 1930's and was continued over a period of several decades by Juza and co-workers, synthesising and characterising and reporting a large number of metal and non-metal binary nitrides [6, 7, 8]. As a result of this work, a number of nitride materials have found application in industry, for example as semiconductors (Cu_3N, GaN) [9, 10], optoelectronic devices (TiN, BN, AlN, GaN and InN) [11, 4, 12, 13] and high temperature refractory ceramics (AlN, BN and TiN, Si_3N_4) [5, 14, 15] and more recently Indium gallium nitride which is used in blue LEDs.

The synthesis of nitrides is still very complex with large thermodynamic barriers which occur from the making and breaking of N≡N bonds (945 $KJmol^{-1}$ for N≡N compared to 498 $kJmol^{-1}$ for O=O) [16], which is energetically unfavourable. Furthermore, nitrogen requires the electron affinity of N^{-3} from N is rather large (+2300 $kJmol^{-1}$, over three times that of O to form O^{2-}, +700 $kJmol^{-1}$). The implication of these factors is that nitrides are less stable than oxides, with respect to the decomposition at high temperature into the elements and have lower thermal stability [17]. Also, nitrogen does not form predominately ionic bonds except with the most electropositive of elements, whose significance in stabilising bonding environments which would be otherwise unattainable cannot be overemphasised.

The study of ternary and higher nitrides has only really developed as an independent field in the decade or so, with fewer than 400 unique ternary metal nitrides catalogued in the Inorganic Crystal Structure Database (ICSD) in contrast to over 4,000 ternary metal oxides. The paucity of known nitrides [1, 5] can largely be attributed to the challenging requirements of nitrides synthesis, but also due to the limitations of analytical methods such as powder X-ray diffraction [5]. Perhaps it is this that has led to the low abundance of nitride compounds, compared to those of the oxides or carbides [5].

Many nitrides are air and moisture sensitive and rapidly form oxides, hydroxides and ammonia upon contact with oxygen or moisture. They must be synthesised in oxygen- and water-free atmospheres to achieve high purity [18, 19, 20, 21]. Synthetic approaches using more activated forms of nitrogen can be used to overcome the inertness of N_2, but increased exothermicity can also result in diminished stoichiometric control and the activation of deleterious competing pathways.

These stringent synthesis constraints, coupled with the poor intrinsic stabilities of nitrides, impose significant risk on the exploratory synthesis of novel nitride materials [22, 5]. Recent developments in the handling methods for air sensitive samples and improved diffraction techniques have led to a revival in the area of nitride chemistry and thus a large increase in research [1, 2, 4].

As the research articles on different metal nitrides are very vast and discussions on all these articles are beyond the scope of this dissertation, the review work has been concentrated on transition metal nitrides and binary nitrides relevant to the present research work.

The present dissertation is sub divided in two parts. Part-I consists of three chapters. The first chapter is dedicated to the description of the research background. It presents a brief introduction with an overview of related literature and objectives of the study. The second chapter provides experimental details of materials preparation. The characterisation techniques used throughout this project are given in chapter three. Part-II consisted of three chapters and is concerned with the experimental data analyses, the general discussion of the results and conclusions.

Most of the experimental investigation have been carried out during the research placement at the University of Glasgow (United Kingdom). The scholarship of seven months was part of the National Exceptional PNE Program for the academic year 2019-2020.

Part-I Theoretical Aspect

Chapter-1: Review in Metal Nitrides Research

1 Introduction

Recent trends in inorganic metal nitrides research developed due to their promising features. Although the number of applications in which nitrides are utilised has grown significantly, these are still somewhat limited and it is apparent that much work is needed to develop other potential uses. One group of the most appealing transition metal nitrides. Literature and previous investigations had been very thorough in the study of binary nitrides in both the formation and their structure.

1.1 Background

1.1.1 Transition metal nitrides

Transition-metal nitrides attracted interest at an early stage because of their striking properties such as hardness, high melting point, metallic lustre with sometimes vivid colours [23] and simple metallic structures combined with excellent electrical and thermal conductivities. This combination of these properties has attracted considerable attention and has resulted in numerous technical applications [24, 25].

Lengauer [26] has compiled several data and features of transition metal nitrides and carbonitrides. Many of the nitride phases closely resemble metallic alloys, with broad ranges of homogeneity, particularly if the structure of the metallic host lattice is one of the types encountered in typical metals. They often form solid solutions with structurally related compounds, such as other transition metal nitrides or carbides, and are easily wetted by liquid metals of the iron group.

Transition metal nitrides are of great interest in various industry applications [27, 28] including packaging materials for semiconductors [29, 30], coatings for high-speed alloy cutting [31] and high-temperature structural ceramics for nuclear materials [32], etc., owing to their excellent physical, chemical and mechanical properties [33, 34]. Among the transition metal nitrides those containing d-block elements: Mn_4N, NbN, Mo_2N, TaN and ZrN.

Mn_4N

There are several manganese nitride phases known in the Mn–N system depending on the temperature range and equilibrium Mn/N ratio [35]. The highest manganese content phase e-Mn_4N has a regular fcc crystallographic structure. The phase f that is found for such compositions as Mn_5N_2, Mn_2N, and $Mn_2N_{0.86}$ shows a hexagonal hcp structure, whereas the phases g-Mn_3N_2 and h-MnN are tetragonal face centered [36, 37]. These phases have different magnetic properties with the g and h polytypes

being antiferromagnetic [38] and e polytype reported to be ferrimagnetic (T_c = 738 K) [39].

The synthesis has predominantly been accomplished by nitridation of manganese metal in flowing ammonia NH_3 or nitrogen gas N_2. In this way, for instance, the microcrystalline MnN polytype was synthesised [40]. Reactions of nitrogen or ammonia with Mn-amalgams yielded the g and h manganese nitride phases with no reference to their crystallinity [41]. High-energy ball-milled manganese metal when nitride with N_2 at 823–1023 K resulted in Mn_4N and $Mn_2N_{0.86}$ [36]. Microwave energy was used to produce mixtures of Mn_2N and Mn_4N using metallic Mn and N_2/H_2 as precursor systems [42]. Two more ways described in the literature include high-pressure autoclave methods [43].

ZrN

Zirconium nitride (ZrN) has attracted much attention due to its good physical and chemical properties [44]. It possesses high melting point (2980 ± 50°C), high hardness (~15 GPa), good abrasive resistance [45], corrosion resistance and good chemical compatibility with actinides [46, 47]. ZrN has been proposed as coatings [48, 49] for thermal barrier layers and tooling setups for materials processing [50, 51], refractory materials [52], diffusion barriers [53] and Josephson junction in electronics [54, 55]. Particularly, based on its low neutron capture cross-section and good chemical compatibility with actinides, zirconium nitride is an important material used as ceramic matrix of inert matrix fuel (IMF) to transmute long-lived actinides and as advanced fuel particle coatings [56, 57, 58]. Moreover, it is a surrogate for uranium nitride in order to optimize the process parameters for nitride fuel fabrication, which is being considered for application in space power reactors [59] and advanced accident-tolerant fuels for nuclear reactors [60, 61].

The synthesis of zirconium nitride powders mainly includes direct nitridation of Zr metal with nitrogen [62, 63], high energy reactive ball milling (RBM) [64], microwave plasma method [65], benzene-thermal method [66], aluminium reduction nitridation [67], magnesium thermal reduction [68], carbothermic reduction nitridation (CRN) [69] and direct carbothermic nitridation (CN) of zirconia (ZrO_2) [70] and zircon [71], etc. CRN and CN processes are appropriate routes for various sizes and morphologies like particles [72, 73], fibres [74], microspheres [75], films and bulk materials [76],

and have a great possibility of large-scale production of zirconium nitride and other transition metal nitrides.

Zirconium nitride powders have been prepared by hydrogenation–nitridation method [77], high energy reactive ball milling [78], microwave plasma method [79], as well as reduction nitridation process with different reducing agents such as carbon [80], aluminium [81] and magnesium [82]. It is noteworthy that carbothermic nitridation process has the simplicity for a large-scale production. However, it is difficult to obtain nanocrystalline ZrN powders by this route. ZrN particles with nanocrystalline feature have higher surface area and excellent sintering properties. Hence it is effective in fabricating fully dense material [83].

NbN

Niubium nitride (NbN) exhibits a variety of interesting properties like high melting point and high hardness, electrical conductivity, chemical inertness. Improved mechanical properties and thermal stability have been reported in NbN-based nanolayers compared to monolithic coatings [84]. NbN films are used as cathode material for field emission in vacuum microelectronic devices [85] and can be exploited as tunnel junctions due to their superconducting nature [86].

There are several phases of NbN, all of which are hexagonal except for δ-NbN [87]. Some of these phases, including the δ-phase, can be synthesized by modifying the calcination conditions used to process the NbN precursor. The structure of δ-NbN is B1 (NaCl) with metallic bonding character between the Nb and N atoms, this phase is a solid solution with a range of stoichiometries in which the N/Nb ratio is between 0.38 and 0.98 [87]. δ-NbN is also a superconductor with desirable characteristics, including high critical current density ($J_C \sim 10^5$ A/cm^2 at 4.2 K and 100 kOe), high upper critical magnetic field ($Hc_2 \sim 200$ kOe), and a relatively high superconducting transition temperature (T_C= 17.3 K) [88, 89], Primarily because of its high J_C, NbN is a critical component of many technologically important devices including dc-superconducting quantum interference devices (SQUIDS), Josephson junctions, switches for pulsed power applications, and fusion reactor magnets [90, 91].

Various authors have reported about the preparation and superconducting properties of niobium nitride. Rögener [92] obtained niobium nitride samples by diffusion of nitrogen in niobium wire. G. V. Samsonov [93], K. Hechler and E. Saur [94] reported about the preparation and, specifically, the superconducting properties of pure

niobium nitride and ternary niobium nitride compounds and A. N. Christensen [95] described the preparation of niobium nitride single crystals. Drafting a phase diagram of the Nb-N system has since been the objective of studies, among others, by G. Brauer and H. Kirner [96], R. W. Guard *et al*. [97] and C. Politis [98].

Mo_2N

Mellor (1927, p.128) and Brown (1964, p.200) have summarised the various production methods used to obtain molybdenum nitride. The reaction between molybdenum and nitrogen proceeds at a correspondingly lower rate than the one between chromium and nitrogen. Henderson and Galletly (1908) reported that by reaction of metallic molybdenum with ammonia at 850°C, only a small portion of the metal is transformed into nitride. An X-ray investigation of products of the action of nitrogen on molybdenum at temperatures between 400-1000°C showed indication of nitride formation (Ghosh, 1952). Hagg (1930) nitride very pure molybdenum for 4 hours in a porcelain tube furnace with ammonia between 400-725°C. Matsumoto (1966) prepared Mo_2N by the nitrogen plasma jet in a 40 % yield. The maximum surface temperature of Mo was 2900°C.

Molybdenum nitrides are also superconducting and the predicted value of the transition temperature for the metastable MoN phase of NaCl-B1-type cubic structure is the highest of all refractory carbides and nitrides. Much data about the properties of transition metal carbides and to a lesser extent those of transition metal nitrides has been gathered in some books and reviews [99, 100]. Molybdenum nitrides also crystallise in a structure similar to γ-Mo_2N with an excess of nitrogen in the lattice and with the formula Mo_3N_2 [101].

TaN

Tantalum nitride (TaN) is gaining increasing interest due to its excellent chemical and physical properties. TaN is a widely used material for producing hard coatings, wear resistant layers, thin film resistors, diffusion barriers in integrated circuits and mask layers for X-ray lithography [102, 103]. TaN coatings that are deposited via magnetron sputtering result in a variety of compound solutions, such as body centered cubic (bcc) TaN, hexagonal TaN, hex Ta_2N, face centered cubic (fcc) TaN, hexagonal Ta_5N_6, tetragonal Ta_4N_5, and orthorhombic $Ta_6N_{2.5}$, Ta_4N, Ta_3N_5 with differing physical, chemical, and mechanical properties [104, 105]. The reported

values of hardness for various phases of TaN thin films, such as hex Ta_2N, fcc TaN, orth $Ta_6N_{2.5}$ and orth Ta_4N are 31, 20, 30.8, and 61.8 GPa, respectively [106, 107].

Mellor (1927, P. 126) and Brown (1964, P. 192) have summarised methods of production of tantalum nitride. The nitride, TaN, can be prepared by causing tantalum metal to react with nitrogen or ammonia; Chiotti (1952) treated tantalum metal powder with ammonia for 18 hours at 900°C and even this procedure does not give complete conversion to the mononitride. When the powdered pentoxide reacts with ammonia at 500-800°C or with nitrogen and hydrogen mixture at about 900°C, little or no TaN is formed (Bagnall, 1957). Agte and Moers (1939) mixed the pentoxide and then caused the mixture to react with nitrogen at 2300°C.

1.1.2 Binary nitrides

Li_3N

Alkali metal nitrides are dominated by lithium nitride. Li_3N is probably the most studied nitride to date, with much of the research focusing on the electrochemical properties of the material and its related compounds. The structure of α-Li_3N (Fig.1.1) is characterised by hexagonal Li_2N layers, perpendicular to the c axis. A lithium defect concentration of 1–2 % is responsible for the high mobility of Li^+ ions Li(2) in these Li_2N layers [108]; the positions of the bridging lithium atoms Li(1) between the layers are fully occupied and do not contribute to ionic conductivity. Defect formation is due to the incorporation of hydrogen and NH^{-2} groups [109].

Because of compositional differences, it is very difficult to give precise values for the ionic conductivity of lithium nitride. At 300 K, conductivity values of 1.2×10^{-3} $\Omega^{-1}cm^{-1}$ have been measured perpendicular to the c axis for single crystals, and 6.6×10^{-4} $\Omega^{-1}cm^{-1}$ for polycrystalline materials [110]. α-Lithium nitride melts congruently at 1086 K. Ruby-red single crystals can be formed by reacting molten lithium with nitrogen at ca. 0.1 MPa and 800 K, according to the Czochralski method [111]. Single crystals with a volume of ca.10 cm^3 can be produced in this way for solid state studies [111, 112].

Beta-Li_3N [113], can be obtained from α-Li_3N via high pressure methods (4.2 kbar at 300 K) [114]. The crystal structure of the β-form, isotypic with Li_3P, is also composed of planar layers with hexagonal symmetry (Fig.1.2). Each nitrogen atom is bound by two lithium atoms, at 209.5 pm above and below the plane. β-Li_3N was first detected by [115] Li-NMR in a Li_3N single crystal at hydrostatic pressures in which the transition

pressure was reported as 4.2 kbar at 300 K [114]. Although the new phase could not be structurally characterised, a variance in the [115] Li-NMR spectrum revealed the presence of 2 inequivalent Li sites with different quadrupole coupling constants from the alpha structure; 406 and 164 kHz instead of 582±2 and 285±2 kHz [116]. Least squares calculations determined lattice constants which gave a *c*/*a* ratio of 1.78 for β-Li_3N (in comparison to a value of 1.03 for that of α-Li_3N [117] indicative of a Na_3As structure type [118].

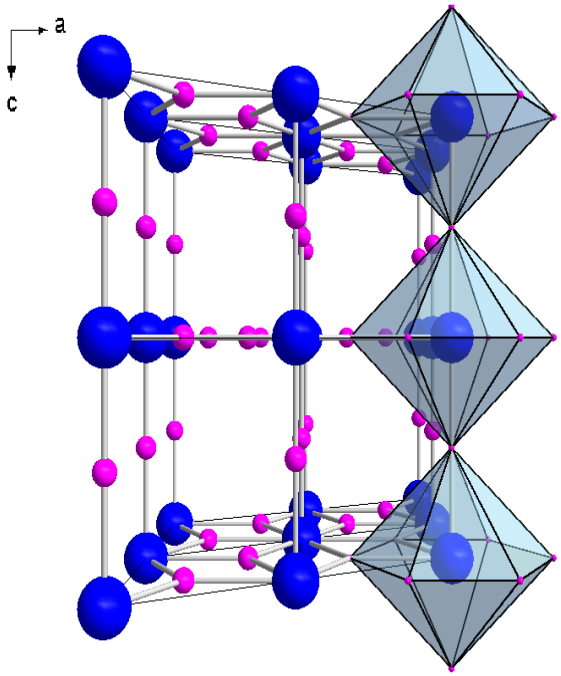

Fig.1.1 Hexagonal structure adopted by α-Li_3N (Li^+ pink, N^{3-} blue) [119].

The third polymorph, γ-Li_3N, can be fully transformed from β-Li_3N between 35-45 GPa and is stable up to 200 GPa [116]. γ-Li_3N, was observed in depressurised samples of Li_3N which had been subjected to pressures of more than 10 GPa [116]. X-ray diffraction data showed that this high-pressure phase was consistent with a cubic face-centred lattice, and it is isostructural with Li_3Bi.

There two methods of producing Li_3N, the reaction of nitrogen with lithium dissolved in liquid sodium [120] and the high temperature reaction of solid lithium under nitrogen.

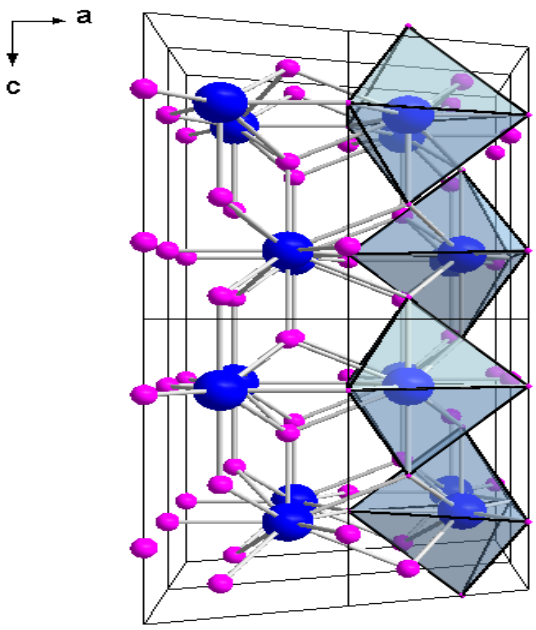

Fig.1.2 Hexagonal structure adopted by β-Li_3N (Li^+ pink, N^{3-} blue) [113].

Mg_3N_2

Magnesium nitride is the alkaline earth metal nitride. Mg_3N_2, has an anti-bixbyite structure [121] with the body-centred cubic cell [121, 122] and space group *Ia-3*(206). Fig.1.3(a) Crystal structure of Mg_3N_2 (cubic anti-bixbyite structure). The unit cell includes 48 metal atoms and 32 nitrogen atoms. The lattice parameter is 0.996 nm [121]. The 80 atoms unit cell composed by 8 basis cells. Fig.1.3(b) is the example configurations of basis cell. The black circles represent the metal vacancies. Fig.1.3(c) is the simplified symbolic cell of Fig.1.3(b). Fig.1.3(d) shows the 8 basis cells arrangement in an 80 atoms unit cell.

The 80 atoms unit cell composed by 8 basis cells and each basis cell has 6 metal atoms and 4 nitrogen atoms, and these 6 metal atoms have different positions. Unlike the unit cell of fluorite structure which has 8 atoms in the centre, the basis cell of anti-bixbyite has 2 metal atom vacancies, and these 2 vacancies are body diagonally arranged.

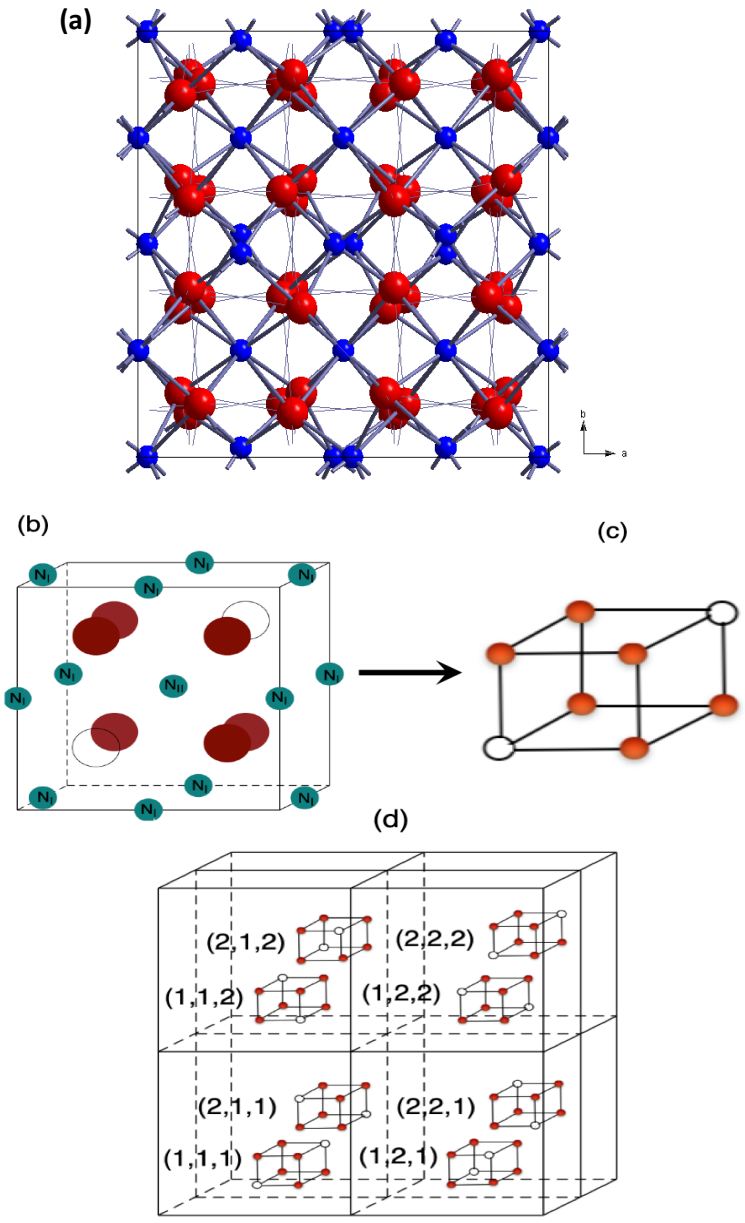

Fig.1.3 Representation of Mg_3N_2 anti-bixbyite structure, blue spheres represent nitrogen atoms, red spheres represent Mg [123].

Three polymorphs of Mg_3N_2 are known; α, β and γ with phase transitions at 823 K (α→β) and 1053 K (β→γ) [124], however the alpha polymorph is the only form which has been fully characterised. Mg_3N_2 was fully refined from PND data by Partin *et al* confirming that it adopts a cubic *anti*-bixbyite structure analogous with Be_3N_2 [125].

1.2 Research aims

This project aims at synthesising, studying and improving the preparation of different nitride materials. Simple and cost-effective methods with relatively low impact on the environment have been privileged in the selection.

Our research primarily involves the preparation of Mn_4N, NbN, Mo_2N, TaN and ZrN transition metal nitrides. The second goal of this work was the synthesis of Li_3N and Mg_3N_2 binary nitrides, and the study of certain parameters. A detailed investigation of metal nitrides was pursued through evaluation of the final product according to the reaction conditions (time, temperature, heating rate,..etc).

With this respect, all the analysis was performed to better understand and optimise the synthesis procedures, and ultimately improvement of the properties of the final products.

1.3 References

[1] N. E. Brese, M. O'Keeffe, *Struct. Bonding (Berlin).*, 1992, **79,** 307.

[2] R. Niewa, H. Jacobs, *Chem. Rev.*, 1996, **96,** 2053.

[3] R. Kniep, *Pure Appl. Chem.*, 1997, **69,** 185.

[4] R. Niewa, F. J. DiSalvo, *Chem. Mater.*, 1998, **10,** 2733.

[5] D. H. Gregory, *J. Chem. Soc., Dalton Trans.*, 1999, **3,** 259.

[6] R. Juza, K. Langer, K. Von Brenda, *Angew. Chem., Int Ed. Engl.*, 1968, **7**, 360.

[7] R. Juza, W. Sachsze, *Z. Anorg. Chem.*, 1945, **253**, 95.

[8] R. Juza, H. Hahn, *Z. Anorg. Allg. Chem.*, 1938, **239,** 282.

[9] D. J. As, *Microelectronics Journal.*, 2009, **40**, 204-209.

[10] M. G. Moreno-Armenta, G. Soto, N. Takeuchi, *J. Alloys. Compd.*, 2011, **509(5)**, 1471-1476.

[11] A. Baiker, M. Maciejewski, *J. Chem. Soc, Faraday Trans. 1.*, 1984, **80**(8), 2331.

[12] W. Lengauer, *J. Alloys. Compd.*; 1992, **186**, 293.

[13] Z. G. Chen, L. Cheng, G. Lu, J. Zou, *Chem. Eng. Journal*; 2010, **165**, 714-719.

[14] G. Husnain, F. Tao, S. D. Yao, *Physica B: Condensed Matter.*, 2010, **405(9)**, 2340-2343.

[15] B. Yuan, J. X. Liu, G. J. Zhang, Y. M. Kan, P. L. Wang, *Ceramics International.*, 2009, **35**, 2155-2159.

[16] www.webelements.com [August 2010].

[17] F. J. DiSalvo, S. J. Clarke, *Curr. Opin. Solid State Mater. Sci.*, 1996, **1,** 241.

[18] W. Sun, A. Holder, B. Orvañanos, E. Arca, A. Zakutayev, S. Lany, G. Ceder, *Chem. Mater.*, 2017, **29**, 6936-6946.

[19] T. A. Manz, Introducing DDEC6 atomic population analysis: part 3. Comprehensive method to compute bond orders. *RSC Advances.*, 2017, **7(72)**, 45552-45581.

[20] T. A. Manz, N. G. Limas. Introducing DDEC6 atomic population analysis: part 1. Charge partitioning theory and methodology. *RSC Advances.*, 2016, **6(53)**, 47771-47801.

[21] S. Maintz, V. L. Deringer, A. L. Tchougréeff, R. Dronskowski, LOBSTER: A tool to extract chemical bonding from plane-wave based DFT. *Journal of computational chemistry.*, 2016, **37(11)**, 1030-1035.

[22] N. T. Ruiz, M. Segalés, D. H. Gregory, *Coordination Chemistry Reviews.*, 2013, **257**, 1978–2014.

[23] L. E. Toth, Transition Metal Carbides and Nitrides, *Refractory Materials Series, vol. 7*, Academic Press, New York–London, 1972.

[24] P. Schwarzkopf, R. Kieffer, Refractory Hard Metals, Macmillan, New York, 1953, p. 49.

[25] P. Ettmayer, W. Lengauer, in *Ullmann's Encyclopedia of Industrial Chemistry, Verlag Chemie*, 1991, Vol. A17, Chap. Nitrides, p. 341.

[26] W. Lengauer, in *Handbook of Ceramic Hard Materials*, ed. R. Riedel, Wiley-VCH, Weinheim, Germany, 2000, Vol. I, p. 202.

[27] D. Kiesler, T. Bastuck, R. Theissmann, F. E. Kruis, *J. Nanopart. Res.*, 2015, **17**, 1–13.

[28] T. Nakamura, H. Hayashi, T. Ebina, *J. Nanopart. Res.*, 2014, **16(11)**, 2699.

[29] E. S. Lee, S. M. Lee, D. J. Shanefield, W. R. Cannon, *J. Am. Ceram. Soc.*, 2008, **91(4)**, 1169–1174.

[30] Y. Lv, L. Yu, W. Ai, C. Li, Scalable preparation and characterization of GaN nanopowders with high crystallinity by soluble salts-assisted route, *J. Nanopart. Res.*, 2014, **16**, 2619.

[31] I. El Azhari, J. Garcia, M. Zamanzade, F. Soldera, C. Pauly, L. Llanes, F. Mücklich, Investigations on micro-mechanical properties of polycrystalline Ti(C,N) and Zr(C,N) coatings. *Acta. Mater.*, 2018, **149**, 364–376.

[32] W. E. Lee, M. Gilbert, S. T. Murphy, R. W. Grimes, D. J. Green. Opportunities for Advanced Ceramics and Composites in the Nuclear Sector. *J. Am. Ceram. Soc.*, 2013, **96**, 2005–2030.

[33] X. Wu, G. Liu, J. Li, Z. Yang, J. Li. Combustion synthesis of ZrN and AlN using Si_3N_4, and BN as solid nitrogen sources. *Ceram. Int.*, 2018, **44**, 11914–11917.

[34] X. G. Lu, M. Selleby, B. Sundman. Calculations of thermophysical properties of cubic carbides and nitrides using the Debye-Grüneisen model. *Acta. Mater.*, 2007, **55**, 1215–1226.

[35] Z. Nishiyama, R. Iwanaga. *J. Nippon Kinzoku Gakkai-Shi.*, 1945, **9**, 1.

[36] W. J. Feng, N. K. Sun, J. Du, Q. Zhang, X. G. Liu, Y. F. Deng, Z. D. Zhang. Structural evolution and magnetic properties of Mn–N compounds. *Sol State Commun.*, 2008, **148**,199–202.

[37] R. Niewa. Nitridocompounds of manganese: manganese nitrides and nitridomanganates. *J. Z Kristallogr.*, 2002, **217**, 8–23.

[38] K. Suzuki, T. Kaneko, H. Yoshida, Y. Obi, H. Fujimori, H. Morita. Crystal structure and magnetic properties of the compound MnN. *J. Alloy Compd.*, 2000, **306**, 66–71.

[39] W. J. Takei, R. R. Heikes, G. Shirane. Magnetic structure of Mn_4N-type compounds. *Phys Rev.*, 1968, **125**, 1893–1897.

[40] N. A. Gokcen. The Mn–N (manganese-nitrogen) system. *Bull Alloy Phase Diagrams.*, 1990, **11**, 33–42.

[41] F. Lihl, P. Ettmayer, A. Kutzelnigg. The system manganese-nitrogen. *Z Metallk.*, 1962, **53**, 715–721.

[42] J. W. Huang, J. Li, H. Peng. Microwave synthesis of manganese nitride. *Powder Metall.*, 2007, **50**, 137–141.

[43] G. Kreiner, H. Jacobs. Magnetische structure von g-Mn3N2. *J Alloy Compd.*, 1992, **183**, 345–362.

[44] Y. Chen, C. J. Deng, C. Yu, J. Ding, H. X. Zhu. *Ceram. Int.*, 2018, **44**, 8710–15.

[45] B. Fu, L. Gao. Synthesis of nanocrystalline zirconium nitride powders by reduction-nitridation of zirconium oxide. *J. Am. Ceram. Soc.*, 2004, **87**, 696–698.

[46] R. W. Harrison, W. E. Lee. *J. Am. Ceram. Soc.*, 2015, **98**, 2205–13.

[47] M. Burghartz, G. Ledergerber, H. Hein, R. R. Van der Laan, R. J. M. Konings. *J. Nucl. Mater.*, 2001, **288**, 233–236.

[48] C. Brugnoni, F. Lanza, G. Macchi, R. Müller, E. Parnisari, M. F. Stroosnijder, J. Vinhas. *Surf. Coat. Technol.*, 1998, **23**, 100–101.

[49] J. Musil, S. Zenkin, S. Kos, R. Cerstvy, S. Haviar. *Vacuum.*, 2016, **131**, 34–38.

[50] G. Lee, M. S. Yurlova, D. Giuntini, E. G. Grigoryev, O. L. Khasanov, J. McKittrick, E. A. Olevsky. Densification of zirconium nitride by spark plasma sintering and high voltage electric discharge consolidation: A comparative analysis. *Ceram. Int.*, 2015, **41**, 14973–14987.

[51] F. Wang, D. Holec, M. Odén, F. Muecklich, I. A. Abrikosov, F. Tasnadi. Systematic *ab initio* investigation of the elastic modulus in quaternary transition metal nitride alloys and their coherent multilayers. *Acta. Mater.*, 2017, **127**, 124–132.

[52] C. J. Xuan, Z. Zhao, P. G. Jönsson. Wettability and corrosion of spark plasma sintered (SPS) ZrN by liquid iron and steel. *J. Eur. Ceram. Soc.*, 2016, **36**, 2435–2442.

[53] M. Wittmer. High-temperature contact structures for silicon semiconductor devices. *Appl. Phys. Lett.*, 1980, **37**, 540–542.

[54] K. Schwarz, A. R. Williams, J. J. Cuomo, J. H. E. Harper, H. T. G. Hentzell. Zirconium nitride-a new material for Josephson junctions. *Phys Rev B: Condens. Matter. Mater. Phys.*, 1985, **32**, 8312–8316.

[55] K. Schwarz, A. R. Williams, J. J. Cuomo, J. H. E. Harper, H. T. G. Hentzell. *Phys Rev B: Condens. Matter. Mater. Phys.*, 1985, **32**, 8312–16.

[56] M. Burghartz, G. Ledergerber, H. Hein, R. R. Van Der Laan, R. J. M. Konings. Some aspects of the use of ZrN as an inert matrix for actinide fuels. *J. Nucl. Mater.*, 2001, **288**, 233–236.

[57] J. Adachi, K. Kurosaki, M. Uno, S. Yamanaka. Porosity influence on the mechanical properties of polycrystalline zirconium nitride ceramics. *J. Nucl. Mater.*, 2006, **358**, 106–110.

[58] Lee, G. *et al*. Effect of electric current on densification behavior of conductive ceramic powders consolidated by spark plasma sintering. *Acta. Mater.*, 2018, **144**, 524–533.

[59] K. Wheeler, P. Peralta, M. Parra, K. Mcclellan, J. Dunwoody, G. Egeland. Effect of sintering conditions on the microstructure and mechanical properties of ZrN as a surrogate for actinide nitride fuels. *J. Nucl. Mater.*, 2007, **366**, 306–316.

[60] W. E. Lee, E. Giorgi, R. Harrison, A. Maître, O. Rapaud. Nuclear Applications for Ultra-High Temperature Ceramics and MAX Phases //Ultra-High Temperature Ceramics: Materials for Extreme Environment Applications. *John Wiley and Sons, Inc.*, 2014.

[61] P. Merja, T. Masahide. Sintering and characterization of ZrN and (Dy,Zr)N as surrogate materials for fast reactor nitride fuel. *J. Nucl. Mater.*, 2014, **444**, 7–13.

[62] R. S. Reddy, M. Kamaraj, U. K. Mudali, S. R. Chakravarthy, R. Sarathi. Generation and characterization of zirconium nitride nanoparticles by wire explosion process. *Ceram. Int.*, 2012, **38**, 5507–5512.

[63] P. Merja, T. Masahide, N. Tsuyoshi. Sintering and characterization of (Pu,Zr)N. *J. Nucl. Mater.*, 2014, **444**, 421–427.

[64] M. S. El-Eskandarany, A. H. Ashour. Mechanically induced gas-solid reaction for the synthesis of nanocrystalline ZrN powders and their subsequent consolidations. *J. Alloy. Compd.*, 2000. **313**, 224–234.

[65] J. L. H. Chau, C. C. Kao. Microwave plasma synthesis of TiN and ZrN nanopowders. *Mater. Lett.*, 2007, **61**, 1583–1587.

[66] Y. Gu, F. Guo, Y. Qian, H. Zheng, Z. Yang. A benzene-thermal synthesis of powdered cubic zirconium nitride. *Mater. Lett.*, 2003, **57**, 1679–1682.

[67] L. Yin, M. I. Jones. Synthesis of ZrN powders by aluminum-reduction nitridation of ZrO_2 powders with $CaCO_3$ additive. *Ceram. Int.*, 2017, **43**, 3183–3189.

[68] Y. Chen, C. Deng, C. Yu, J. Ding, H. Zhu. Molten-salt nitridation synthesis of cubic ZrN nanopowders at low temperature via magnesium thermal reduction. *Ceram. Int.*, 2018, **44**, 8710–8715.

[69] R. Harrison, O. Rapaud, N. Pradeilles, A. Maître, W. E. Lee. On the fabrication of ZrC_xN_y from ZrO_2 via two-step carbothermic reduction-nitridation. *J. Eur. Ceram. Soc.*, 2015, **35**, 1413–1421.

[70] T. B. Jit, X. Youming, S. G. Francis, L. S. Steven. Thermodynamic analysis and synthesis of zirconium nitride by thermal nitridation of sol gel zirconium oxide. *Chem. Mater.*, 1994, **6**, 918–926.

[71] S. Yugeswaran, P. V. Ananthapadmanabhan, L. Kumaresan. Synthesis of zirconium nitride from zircon sand by transferred arc plasma assisted carbothermal reduction and nitridation process. *Ceram. Int.*, 2018, **44**, 14789–14796.

[72] P. H. Suman, M. O. Orlandi. Influence of processing parameters on nanomaterials synthesis efficiency by a carbothermal reduction process. *J. Nanopart. Res.*, 2011, **13**, 2081–2088.

[73] L. Yin, Y. Xu, Z. Huang, Y. Liu, M. Fang, B. Liu. Synthesis of ZrN-Si3N4 composite powders from zircon and quartz by carbothermal reduction and nitridation. *Powder. Technol.*, 2013, **246**, 677–681.

[74] A. D. Mazzoni, M. S. Conconi. Study of carbonitriding reactions of zirconia. Synthesis of Zr(C , N, O) phases and ß-type zirconium oxynitrides. *Ceram. Int.*, 2004, **30**, 23–29.

[75] J. Y. Li, Y. Sun, Y. Tan, M. F. Xu, X. L. Shi, N. Ren. Zirconium nitride (ZrN) fibers prepared by carbothermal reduction and nitridation of electrospun PVP/zirconium oxychloride composite fibers. *Chem. Eng. J.*, 2008, **144**, 149–152.

[76] K. S. C. Weil, P. R. N. Kumta. Synthesis of transition metal nitride powders and coatings using alkanolamine chelated precursors. *Mater. Design.*, 2001, **22**, 605–615.

[77] T. Hollmer. Manufacturing methods for (U-Zr)N-fuels. *KTH Royal Institute of Technology (Diploma thesis).*, 2011, 29–34.

[78] M. S. El-Eskandaranya, A. H. Ashourb. *J. Alloys Compd.*, 2000, **313**, 224–234.

[79] J. L. H. Chau, C. C. Kao, *Mater. Lett.*, 2007, **61**, 1583–87.

[80] R. Harrison, O. Rapaud, N. Pradeilles, A. Maître, W. E. Lee. *J. Eur. Ceram. Soc.*, 2015, **35**, 1413–21.

[81] L. Yin, M. I. Jones. *Ceram. Int.*, 2017, **43**, 3183–89.

[82] Y. Chen, C. J. Deng, C. Yu, J. Ding, H. X. Zhu. *Ceram. Int.*, 2018, **44**, 8710–15.

[83] M. G. Chaudhuri, J. Basu, G. C. Das, S. Mukherjee, M. K. Mitra. *J. Am. Ceram. Soc.*, 2013, **96**, 385–390.

[84] S. A. Barnett, A. Madan, I. Kim, K. Martin. Stability of nanometer-thick layers in hard coatings. *MRS Bull.*, 2003, **28**, 169–172.

[85] Y. Gotoh, M. Nagao, T. Ura, H. Tsuji, J. Ishikawa. Ion-beam assisted deposition of niobium nitride thin films for vacuum microelectronics devices. *Nucl. Instrum. Methods Phys. Res. Sect. B Beam Interact. Mater. At.*, 1999, **148**, 925–929.

[86] Z. Wang, H. Terai, A. Kawakami, Y. Uzawa. Interface and tunnelling barrier heights of NbN/AlN/NbN tunnel junctions. *Appl. Phys. Lett.*, 1999, **75**, 701.

[87] Comprehensive Inorganic Chemistry. Trotman-Dickerson, A. F., Ed.; Pergamon Press: New York, 1973, pp 604-607.

[88] J. Kodymová, V. Krejci, L. Láska, J. Votruba. Acta. *Phys. Slov.*, 1982, **32**, 177.

[89] A. N. Christensen, S. Fregerslev. *Acta. Chem. Scand. A.*, 1977, **31**, 861.

[90] H. Abe, K. Hamasaki, Y. Ikeno. *Appl. Phys. Lett.*, 1992, **61**, 1131.

[91] M. S. Hossain, K. Yoshida, K. Kudo, K. Enpuku, K. Yamafuji. *Jpn. J. Appl. Phys.*, 1992, **31**, 1033.

[92] H. Rögener, Z. Physik. 1952, **132**, 446.

[93] G. V. Samsonov, O. I. Shulishova, I. A. Shcherbak. *Poroshkovaya metallurgia.*, 1974, **12(144)**, 76-78.

[94] K. Hechler, E. Z. Saur. *Phys.*, 1967, **205**, 392-99.

[95] A. N. Christensen, DGKK-Tagung, Stuttgart, Sept. 1977.

[96] G. Brauer, H. Kirner. *Z. anorg. allg. Chemie, Bd.*, 1964, **328**, 34.

[97] R. W. Guard, J. W. Savage, D. G. Swathout. *Transact of the Met. Soc. of AIME.*, 1976, **239**, 643.

[98] C. Politis, G. Rejman. Kernforschungszentrum Karlsruhe Gmbh, Karlsruhe (D), KFK-Ext. 6/78-1, 1978.

[99] L. Toth. Transition Metal Carbides and Nitrides. *Academic Press*, New York. 1971, pp. 29, 247–261.

[100] The Chemistry of Transition Carbides and Nitrides (Ed. Oyama. S. T.). *Blackie Academic and Professional*. London, UK, 1996. pp. 2–10.

[101] D. Rische. MOCVD of Tungsten and Molybdenum Nitrides. Ph.D. Thesis, University of Bochum, Bochum, Germany, 2007.

[102] J. E. Sundgren, B. O. Johansson, A. Rockett, S. A. Barnett, J. E. Greene. TiN: A Review of the Present Understanding of the Atomic Electronic Structure and Recent

Results on the Growth and Physical Properties of Epitaxial TiNx (0.6 < x < 1.2) Layers. In Physics and Chemistry of Protective Coatings: Universal City, CA, 1985; J. E. Greene, W. D. Sproul, J. A. Thornton. Eds. AIP Conference Proceedings Series 149; American Institute of Physics: New York, NY, USA, 1986, p. 95.

[103] X. Sun, E. Kolawa, J. Chen, J. Reid, M. A. Nicolet. Properties of reactively sputter-deposited TaN thin films. *Thin Solid Films.*, 1993, **236**, 347–351.

[104] C. Stampfl, A. J. Freeman. Stable and metastable structures of the multiphase tantalum nitride system. *Phys. Rev. B.*, 2005, **71**, 024111.

[105] Y. X. Leng, H. Sun, P. Yang, J. Y. Chen, J. Wang, G. J. Wan, N. Huang, X. B. Tian, L. P. Wang, P. K. Chu. Biomedical properties of tantalum nitride films synthesized by reactive magnetron sputtering. *Thin Solid Films.*, 2001, 398–399, 471–475.

[106] K. Valleti, A. Subrahmanyam, S. V. Joshi, A. R. Phani, M. Passacantando, S. Santucci. Studies on phase dependent mechanical properties of dc magnetron sputtered TaN thin films: Evaluation of super hardness in orthorhombic Ta_4N phase. *J. Phys. D Appl. Phys.*, 2008, **41**, 045409.

[107] D. Bernoulli, U. Müller, M. Schwarzenberger, R. Hauert, R. Spolenak. Magnetron sputter deposited tantalum and tantalum nitride thin films: An analysis of phase, hardness and composition. *Thin Solid Films.*, 2013, **548**, 157–161.

[108] H. Schulz, K. H. Thiemann. *Acta Crystallogr. Sect. A: A.*, 1979, **35**, 309.

[109] J. Wahl. *Solid State Commun.*, 1979, **29**, 485.

[110] A. Rabenau. *Solid State Ionics.*, 1982, **6**, 277.

[111] E. Schönherr, G. Müller, E. Winkler. *J. Cryst. Growth.*, 1978, **43**, 469.

[112] E. Schönherr, A. Köhler, G. Pfrommer. *Inorg. Synth.*, 1983, **22**, 48.

[113] H. J. Beister, S. Haag, R. Kniep, K. Strössner, K. Syassen. *Angewandte Chemie International Edition in English.*, 1988, **27**, 1101.

[114] M. Mali, J. Roos, D. Brinkmann. *Physical Review B.*, 1987, **36**, 3888.

[115] U. V. Alpen. *Journal of Solid-State Chemistry.*, 1979, **29**, 379.

[116] A. Lazicki, B. Maddox, W. J. Evans, C. S. Yoo, A. K. McMahan, W. E. Pickett, R. T. Scalettar, M. Y. Hu, P. Chow. *Physical Review Letters.*, 2005, **95**, 165503.

[117] E. Zintl, G. Brauer. *Zeitschrift für Elektrochemie und Angewandte Physikalische Chemie.*, 1935, **41**, 102.

[118] G. Brauer, E. Zintl. *Zeitschrift für Physikalische Chemie.*, 1937, **837**, 323.

[119] A. Rabenau, H. Schulz. *Journal of the Less-Common Metals.*, 1976, **50**, 155.

[120] C. C. Addison, B. M. Davis. *J. Chem. Soc. (A).*, 1969, 1827.

[121] D. E. Partin, D. J. Williams, M. O'Keeffe. *J. Solid State Chem.*, 1997, **132**, 56.

[122] A. M. Heyns, L. C. Prinsloo, K. J. Range, M. Stassen. *J. Solid State Chem.*, 1998, **137**, 33.

[123] Peng Wu. Epitaxial Growth and Optical Properties of Mg_3N_2, Zn_3N_2, and Alloys, 2019. Thesis, University of Victoria.

[124] D. W. Mitchell. *Industrial and Engineering Chemistry.*, 1949, **41**, 2027.

[125] J. David, Y. Laurent, J. Lang. *Bulletin de la Société Française de Minéralogie et de Cristallographie.*, 1977, **72**, 1949.

Chapter-2: Experimental Details

2 Experimental and methodology

The aim of this chapter is to illustrate in detail the synthetic methods to prepare nitride materials described in this work.

2.1 Air sensitive handling techniques

As the majority of the samples used during this thesis are air sensitive, then they must be handled and stored in an inert atmosphere. All procedures, including sample preparation, mixing and pelletising were performed in an N_2-filled mBRAUN LABstar glovebox (Fig.2.1), with an operating pressure of 2.3 mbar. H_2O and O_2 contents typically below 0.5 ppm. The N_2(g) is supplied to the glovebox via an N_2 generator in the lab (99-99.9 % purity). The atmosphere of the glovebox is kept clean by the recirculating of inert gas using an internal recirculating pump. For weighing manipulations, the recirculating pump can be switched off for minimal periods.

Excess moisture/oxygen is removed from the glovebox by molecular sieves/catalysts at the side of the box. The molecular sieves remove the water from the inert gas, while the catalyst removes the oxygen from the gas. These are regenerated at regular periods. The molecular sieve is regenerated by heating under vacuum with liquid N_2 used to collect the water. The catalyst is regenerated by heating under a flow of H_2/N_2(g) (1:9) under vacuum overnight to remove the oxygen that is absorbed to the water. The catalyst is then heated under vacuum to remove the water by-product. The levels of moisture and oxygen are indicated by their respective sensors at the left-hand side of the glove box and should typically be in the 0-5 ppm region for oxygen and 0-30 ppm for water.

The transfer of samples into and out of the glovebox is via a transfer port at the side of the glovebox in order to preserve the inert atmosphere of the glovebox. The transfer port is kept under vacuum when not in use. To transfer samples and equipment to the glovebox, the transfer port is filled with the relevant gas (N_2(g)) until atmospheric pressure is achieved.

All equipment used was washed thoroughly, rinsed with acetone and dried to ensure accurate results were obtained. The items required to be transferred into the glovebox are then placed in the transfer port. The transfer port is then evacuated using an Edwards Rotary Vane (RV) pump and gas is introduced until the pressure gauge reaches zero. This process is performed three times in total. After the third

cycle, the contents of the port can be transferred to the glovebox. For removing items from the glovebox, the items are also transferred via the transfer port.

Fig.2.1 mBRAUN LABstar Glovebox.

2.2 Materials synthesis under inert gas

2.2.1 Solid-state reactions

Solid-state reactions in nitride synthesis are typically long and require high temperatures. A reaction can take anything from 6 hours to 3 days, at temperatures of up to 1000 K. These specific reaction conditions are required to overcome significant thermodynamic barriers as well as the slow diffusion rates of solids. However, it is also necessary to prevent the decomposition of nitride products, due to formation of N_2 from nominally N^{-3}, which may occur at relatively low temperatures [1]. Solid-state reactions must be kept under stringent anaerobic and anhydrous conditions, to prevent the often-instantaneous reaction of nitrides with oxygen or water, to form oxides and hydroxides respectively.

It is possible to reduce the high temperatures of some nitride syntheses by use of molten Na as a solvent. The liquid Na forms an alloy with alkaline earth metals, which may then be indirectly reacted with nitrogen to yield a binary nitride. However, this is not a technique that can be exploited in the synthesis of ternary or higher nitrides.

2.3 Glass blowing

A standard quartz tube was prepared by bisecting a longer length of tubing (typically 1 m) with a glass cutter. The two equal length tubes were then separated, and sealed at one end, using glass blowing equipment. This created four quartz tubes of equal length, with one sealed end and one open end. Compound mixtures and pellets were then placed inside and sealed to create an airtight environment. This was achieved in two ways:

1. A filled quartz tube was attached to a specifically built vacuum line via a piece of thick rubber tubing. The tube was evacuated to 10^{-2} Torr and sealed using a glass blowing torch.
2. Inside a nitrogen glovebox, a filled quartz tube was sealed using a rubber septum and parafilm, to give a nitrogen-filled tube.

Synthetic methods are described in detail for each material. Safety protocols in the laboratory were followed; including the filling out of COSSH (Control of Substances Hazardous to Health) forms before commencing specific experiments and experiment cards detailing the primary hazards of the experiment being performed with the information to shut down the reaction safely. Safety equipment, in the form of a laboratory coat, goggles and gloves were always worn whilst conducting experiments in the laboratory environment.

2.4 Preparation of transition metal nitrides

All procedures, including sample preparation, mixing and transport were performed in an inert atmosphere inside a glovebox equipped with a circulative purification system to prevent moisture and oxygen contaminations, in which the H_2O and O_2 concentrations were kept below 1 ppm.

2.4.1 Preparation of Mn_4N

Manganese nitride Mn_4N was prepared by heating Mn powder (Aldrich, 99.9 %) in a flow of super pure NH_3 at 600°C for 3 h. An annealing at 500°C has been followed for 20 h in the same atmosphere. Equation (Eq.2.1) outlines the overall reaction.

$$8Mn + N_2 \rightarrow 2Mn_4N \qquad Eq.2.1$$

2.4.2 Preparation of NbN

Niobium nitride NbN nitride was synthesised by the vapor-phase reaction of gaseous niobium pentachloride ($NbCl_5$) with ammonia (NH_3) at 200-1300°C [2]. The formation

process of NbN can be followed by changing heating temperature. The reaction of $NbCl_5$ with ammonia to form $NbCl_5$ and $5NH_3$ has been occurred first at around 200°C. The Nb_4N_5 was obtained at 250-950°C is considered to be due the reaction of $NbCl_5$-$5NH_3$ with ammonia above about 250°C leading to Nb_4N_5 product. Nb_4N_5 decomposes and can be converted to NbN at above 1000°C. The process can be followed by changing the heating temperature as shown below in three equations:

$$NbCl_5 \xrightarrow{200^\circ C} NbCl_5 + 5NH_3 \qquad Eq.2.2$$

$$NbCl_5 + 5NH_3 \xrightarrow{200\text{-}950^\circ C} Nb_4N_5 \qquad Eq.2.3$$

$$Nb_4N_5 \xrightarrow{1000^\circ C} NbN \qquad Eq.2.4$$

2.4.3 Preparation of Mo_2N

Molybdenum nitride Mo_2N was produced by the temperature programmed reaction method previously described [3]. Approximately 0.1 g of molybdenum (VI) oxide powder (MoO_3, Aldrich) was loaded onto a quartz wool plug in a quartz tube reactor. The oxide was first nitridated using a mixture of nitrogen/hydrogen with a predetermined temperature. After the material was cooled to room temperature, the material was passivated in a mixture of 1 % O_2 in He flowing for 24 h. This step was necessary to prevent pyrophoric oxidation upon contact with air.

2.4.4 Preparation of TaN

Tantalum nitride TaN was prepared by the reduction in liquid ammonia. The reaction of solutions of tantalum pentachloride ($TaCl_5$) with sodium was previously reported [4]. The powder obtained by the reduction was then heated under vacuum at 900°C temperature for 24 h. The powder was put into a tantalum crucible, and then was placed into the quartz tube. The operation was done in the glovebox under the atmosphere of argon. The quartz tube was sealed, and moved out from the glovebox, then was placed into the furnace, and connected with the vacuum system. The powder was kept under vacuum, and the temperature of the furnace was raised to set value and kept for 2 h.

2.4.5 Preparation of ZrN

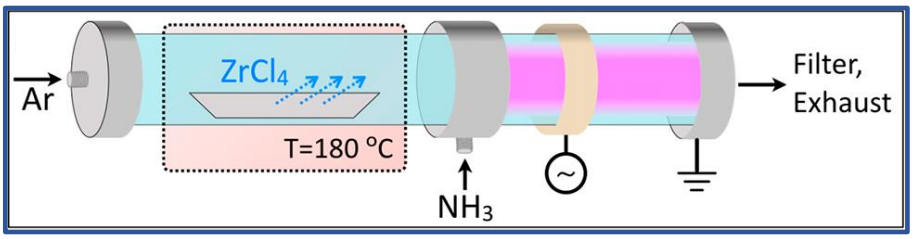

Fig.2.2 Schematic of the nonthermal plasma system used to synthesise ZrN [7].

Zirconium nitride ZrN was produced from Zirconium tetrachloride ($ZrCl_4$, Alfa Aesar) and ammonia (NH_3) injection using nonthermal plasma reactor [5] as shown in Fig.2.2. The as-obtained powder was annealed at 250°C and 0.3 Torr in 90 sccm of argon flow for 1 h to remove the ammonium salt [6]. The process can be followed as shown below in two equations:

$$6ZrCl_4 + 32NH_3 \xrightarrow{NH_3\text{-}180\,^\circ C} 24NH_4Cl + N_2 + 6ZrN \qquad Eq.2.5$$

$$24NH_4Cl + N_2 + 6ZrN \xrightarrow{Ar\text{-}250\,^\circ C} ZrN \qquad Eq.2.6$$

2.5 Preparation of Li_3N

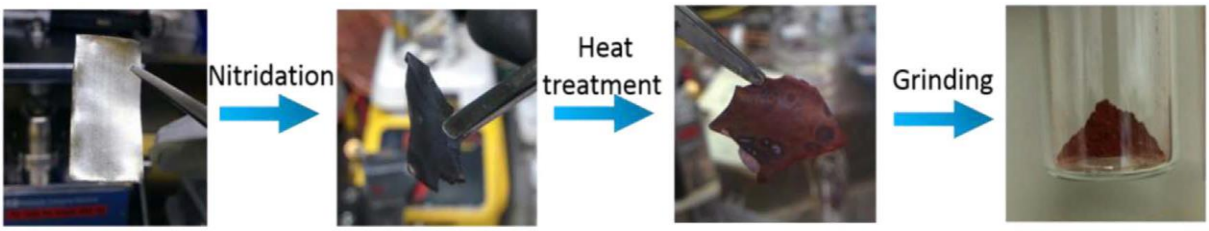

Fig.2.3 Synthesis processes of Li_3N [8].

Lithium metal foil (99.9 purity, 0.75 mm thickness) was purchased from Alfa Aesar and was used for the preparation of Li_3N. During the synthesis, about 1 g of Li metal foil was filed firstly until most of the metal oxide coating removed and a shiny surface appeared. In a recirculating glovebox filled with nitrogen, the Li metal was further filed until no oxide layer remained. After 3 days, the cleaned Li metal foil

transformed spontaneously into a Li_3N flake, which was further heat-treated outside the glovebox using a furnace to ensure the metal has fully reacted with nitrogen. The direct reaction took place under N_2 gas at 200°C for 24 h. Li_3N powder was obtained after grinding using sandpaper or file.

Exposing lithium metal to nitrogen gas at room temperature results in the formation of lithium nitride. Equation 2.1 outlines the overall reaction.

$$6Li + N_2(g) \rightarrow 2Li_3N \qquad Eq.2.7$$

2.6 Preparation of Mg_3N_2

Fig.2.4 Solid-state reaction in small pot furnace.

The Magnesium powder (Alfa Aesar, 99.98 purity) was loaded into an alumina crucible (Al_2O_3) and placed into a quartz tube. The manipulation was done under a continuously purified N_2 atmosphere in glovebox. The reaction was performed in bench and hood type furnace (Fig.2.4). The furnace was then heated to 650-1150°C at the heating rate of 2°C/min. The whole system was kept for 3 h under N_2 flowing gas then allowed to cool naturally to room temperature. A yellow/orange powder was found after cooling. This reaction is the most common method of Mg_3N_2 synthesis found in the literature [9]. Equation 2.8 outlines the overall reaction.

$$3Mg + N_2 \rightarrow Mg_3N_2 \qquad Eq.2.8$$

All obtained samples Mn_4N, NbN, Mo_2N, TaN, ZrN, Li_3N and Mg_3N_2 were transferred directly to the glovebox after cooling in each case, which reduce the risk of impurity phases forming. All the ground samples were stored in the glovebox for further characterisation.

2.7 References

[1] E. K. Storms. The Refractory Carbides, 1st Edition, Academic Press, New York, 1967.

[2] Y. Akimasa, A. Takashi, M. Ryoko, S. Yuzo. *Journal of Bulletin of the Chemical Society of Japan.*, 1984, **57(6)**, 1582-1585.

[3] J. G. Choi, J. R. Brenner, L. T. Thompson. *Journal of Catalysis.*, 1995, **154**, 33.

[4] C. H. Ma, W. F. Zhang, J. L. He, H. M. Zhu. Synthesis and characterization of tantalum nitride nanopowder prepared through homogeneous reaction. *Journal of Transactions of Nonferrous Metals Society of China.*, 2007, **17**, s556-s559.

[5] A. A. Palko, A. D. Ryon, D. W. Kuhn. The Vapor Pressures of Zirconium Tetrachloride and Hafnium Tetrachloride. *J. Phys. Chem.*, 1958, **62**, 319–322.

[6] A. Yajima, Y. Segawa, R. Matsuzaki, Y. Saeki. Reaction Process of Zirconium Tetrachloride with Ammonia in the Vapor Phase and Properties of the Zirconium Nitride Formed. *Bull. Chem. Soc. Jpn.* 1983, **56**, 2638–2642.

[7] S. Exarhos, A. A. Barragan, E. Aytan, A. A. Balandin, L. Mangolini. *ACS Energy Lett.*, 2018, **3**, 2349–2356.

[8] S. Yougming, L. Yanbin, S. Jie, L. Yuzhang, P. Allen, C. Yi. Stabilized Li_3N for efficient battery cathode prelithiation. *Journal of Energy Storage Materials.*, 2017, **6**, 119-124.

[9] O. Reckeweg, J. Francis, Z. Disalvo. *Anorg. Allg. Chem.*, 2001, **627**, 371-377.

Chapter-3: Methods of Analysis

3 Characterisation

A variety of different techniques have been employed to characterise the synthesised materials. Powder X-ray diffraction has been used for structural determination and phase analysis. Different spectroscopy techniques have been required to provide extra information on the structure and properties of these materials.

3.1 Powder X-ray diffraction

Powder X-ray diffraction is an incredibly powerful analytical tool and is ubiquitous in many areas of chemical and physical research. It can provide information on the phase purity, crystallinity and the structure of materials. In the course of this work, it is used mostly to identify the products of reactions and their purity, as well as the relative crystallinity of the obtained material.

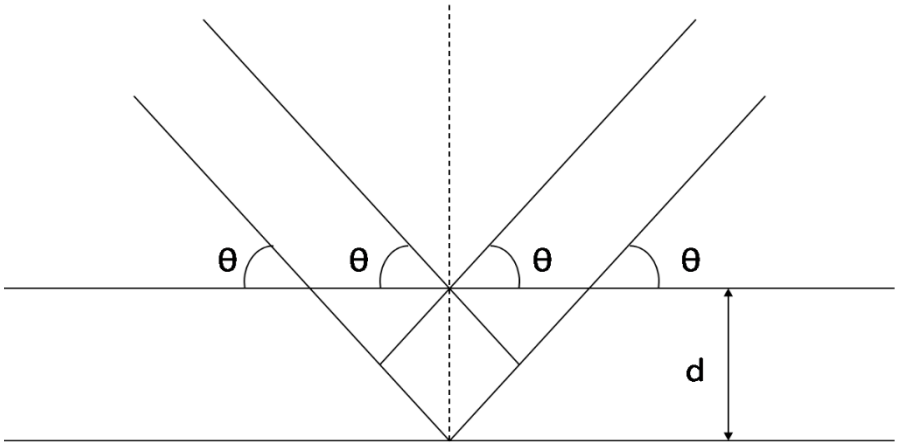

Fig.3.1 Diffraction from parallel planes of point scatterers.

X-rays can be scattered in a manner comparable to light being diffracted by a grating of suitably spaced lines as visualised in Fig.3.1. Atoms or ions arranged in a regular pattern in a crystalline solid can diffract a beam of X-rays which is then detected, however single atoms scatter X-rays so weakly that they cannot be assessed. Only constructive interference of waves from all the contents of a crystal will result in the amplification needed to be able to measure the scattering. W. L. Bragg showed that diffraction patterns could be understood by regarding them as if they were reflected from planes passing through points in the crystal. In order for constructive interference to occur the path difference must correspond to an integral number for wavelengths. This generates the Bragg equation [1]:

$$n\lambda = 2d \sin\theta \qquad Eq.3.1$$

At angles other than the Bragg angle, θ, diffracted beams are out of phase and so destructive interference occurs. The lattice spacings, d, are then calculated by measuring the diffraction maxima. In most cases only n=1 is considered [2]. All the various *d*-spacings possible can then be obtained, where h, k and l are miller indices, the reciprocal values of the fractional positions where the plane cuts the a, b and c axes respectively. The assignment of the Miller indices from *d*-spacings allows the cell size to be calculated. Hence, by studying the diffraction of X-ray beams by crystalline solids structural information can be obtained.

3.1.1 Preparation of PXD samples

Sample preparation for analyses was performed inside the glovebox because all the materials were air sensitive. Before PXD analysis, samples are ground using a mortar and pestle until a fine powder was obtained to ensure a random distribution of crystallites. The random distribution of crystallites ensures that lattice planes are present in every orientation, so for each set of lattice planes some crystals will be orientated at Bragg's angle to give a reflection from these planes. This can also lead to 'preferred orientation' which results in the increase of some intensities which are attributed to a particular direction.

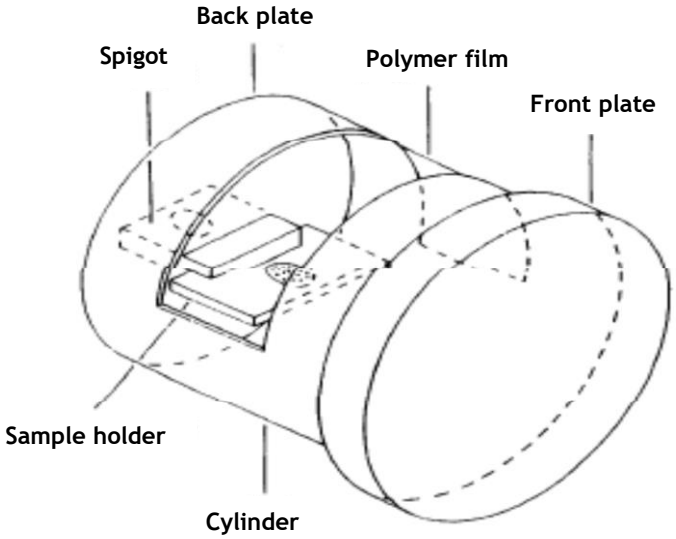

Fig.3.2 Schematic of the air sensitive sample holder. Reprinted [3] with permission from The Royal Society of Chemistry.

For air sensitive materials the samples were prepared by a bespoke Air Sensitive flat plate sample holder for use with the PANalytical X'pert Pro MPD powder diffractometer (Fig.3.2). The air sensitive flat plate sample holder used on the PANalytical X'pert diffractometer consists of two components: a back plate which is fixed to the goniometer of the diffractometer and an air sensitive cylinder (with polymer film) that covers the sample that is placed in the sample holder, which is a glass slide with an indent. The air sensitive holder minimises the exposure of the sample to air and moisture when performing a flat plate reflection experiment in Bragg-Brentano geometry.

The ground sample is placed in the indent of the slide. Ideally, the indent of the sample holder should be completely filled with powder sample, such that the sample is flat with the plane of the slide. The sample holder is then placed in the spigot. The air sensitive cylinder is then placed over the sample inside the glove box. The air sensitive sample holder is also attached to a clamp at all times to allow the air sensitive cylinder to be attached and also for transport of the sample.

3.1.2 Data collection

Obtained samples were characterised by Powder X-Ray diffraction (PXD) using a PANalytical X'pert Pro diffractometer in Bragg-Brentano reflection geometry (Fig.3.3). The X-ray source in a laboratory PXD is typically a sealed tube or a rotating anode. The electrons are emitted by a heated tungsten filament by thermionic emission and are accelerated by high voltage and collide with a metal target typically Cu and produce X-rays. At this stage, there are three wavelengths of X-rays, $K_{\alpha 1}$, $K_{\alpha 2}$ (produced from electrons dropping from the L shells) and K_{β} (produced from electrons dropping from the M shells) produced, with K_{α} ($K_{\alpha 1}$ and $K_{\alpha 2}$) the wavelength of choice as this is the most intense.

In an atom, the innermost shell for electrons is the K-shell (which omits electrons when collision occurs) and this is surrounded by the L and M electron shells which replaces the emitted electrons from the K shell. The X-rays are then filtered through a slit to select the desired wavelength for diffraction.

Samples were analysed using the PANalytical X'pert Pro diffractometer. In Bragg-Brentano configuration the sample is irradiated using a standing X-ray source and a moving detector. The sample holder is placed on one axis and tilted by θ with the detector at 2θ. The diffractometer used Cu $K_{\alpha 1}$ radiation with the X-ray operating

power being 40 KV and 40 mA. The detector was a X' Celerator solid state detector. A monochromator slit of 10 mm was used and a slit size of 0.5 for the divergence and anti-scatter slit used. For phase identification, samples were typically run for 20-30 minutes between 5°- 85°. For Rietveld Refinement, data was collected between 20°-140° for 12 hours with a step size of 0.0167 °/2θ and a time per step of 0.11° per minute. The monochromator mask used was 10 mm.

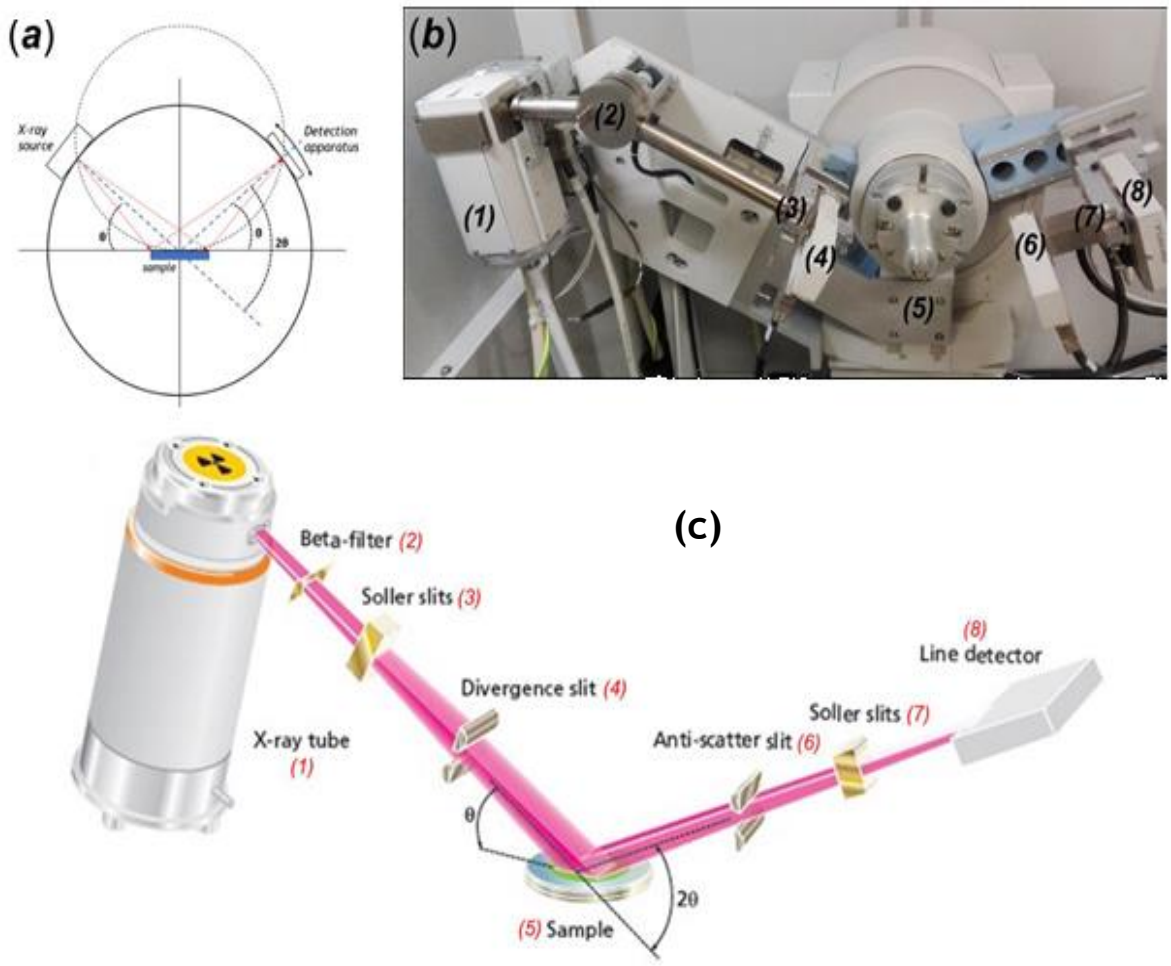

Fig.3.3 (a) Schematic representation of the Bragg-Brentano geometry; (b) picture and (c) schematic diagram of the PANalytical X'Pert PRO MPD diffractometer, with numbers indicating the corresponding components [4].

3.1.3 Data analysis

The PANalytical X'pert produces the PXRD pattern in a PANalytical format (.xdrml). This latter format can be converted to a raw data file by using the PowDLL convertor program [5]. Data manipulation was carried out using the PowderCell program [6].

The obtained pattern was compared to calculated patterns in PowderCell using the crystal data from the Inorganic Crystal Structure database (ICSD) [7]. The obtained pattern was also compared to known patterns in the International Centre for Diffraction data Powder Diffraction File Database (ICDD PDF) using the PANalytical High Score Plus software as identification instrument. Structure refinement was performed against X-ray data using the Rietveld method using the software GSAS [8] and EXPGUI [9].

3.2 Rietveld refinement

Hugo Rietveld as a Dutch mathematician took an early interest in the problems associated with neutron diffraction of powders back in 1964. The Rietveld Method has since become the basis of powder diffraction analysis worldwide [10]. Rietveld refinement was carried out using General Structure Analysis System (GSAS) [9], a full profile refinement software program. The Rietveld method fits experimentally obtained powder data to a refinable structural model allowing accurate measurement of unit cell dimensions, angles and atomic positions as well as information on the preferred orientation of the crystals.

The refinement uses the difference of squares method which is a standard mathematical method used for comparing two similar sets of data step by step. Each experimental data point is taken in turn and compared with the theoretical data point from the model, rather than comparing the shape of the pattern as a whole. The concept of refinement is to iteratively minimise S in equation 3.2.

$$S = \sum_i w_i (y_i - y_{ci})^2 \qquad Eq.3.2$$

S is the residual being minimised

w_i is the Weight factor $= \frac{1}{y_i}$

y_i is the observed intensity

y_{ci} is the calculated intensity

y_{ci} can be calculated from the crystal structure using equation 3.3.

$$y_{ci} = s \sum_k L_k |F_k|^2 \emptyset(2\theta_i - 2\theta_k P_k A + y_{bi}) \qquad Eq.3.3$$

s : scale factor

k : Miller indices h, k, l, for the Bragg reflections

L_K : contains the Lorentz polarisation and multiplicity factors

Ø : reflection profile function

P_K : preferred orientation function

A : absorption factor

F_K : structure factor for the K in the Bragg reflection

y_{bi} : background intensity for the i^{th} step

The accuracy of fit between the model and the data is then measured using a series of R factors. R_{wp} (Eq.3.4) is considered the most useful of these as the numerator is the residual that is being minimised in the refinement.

$$R_{wp} = \sqrt{\left\{\frac{\sum w_i(y_i(obs) - y_i(calc))^2}{\sum w_i\,(y_i(obs))^2}\right\}} \qquad Eq.3.4$$

y_i : diffraction intensity

w_i : 1/y

3.3 Thermal analysis

Thermal analysis methods investigate the physical properties of solids as a function of a change in temperature. They are useful for investigating phase transitions, thermal stability, loss of mass, and for constructing phase diagrams [11]. There are numerous techniques available: the primary differences in the techniques are the properties of the material being studied. Three thermal analysis techniques have been used for the characterisation of the samples in this work (Table.3.1); thermogravimetric analysis (TGA), differential thermal analysis (DTA) and evolved gas analysis (EGA), the latter using a Mass Spectrometer (MS).

Table.3.1 *Common thermal analysis methods and the properties measured [12].*

Method	Abbreviation	Property Measured
Differential Thermal Analysis	DTA	Temperature difference
Thermogravimetric Analysis	TGA	Mass difference
Evolved Gas Analysis	EGA	Gaseous decomposition

3.3.1 Simultaneous thermal analysis (STA)

Measurements were performed using a Netzsch STA 409 analyser (Fig.3.4) which was interfaced to a Hiden HPR 20 Mass Spectrometer. As samples were air sensitive, measurements were undertaken using an instrument located in a mBraun Ar(g) glovebox (<0.1 ppm H_2O, <0.1 ppm O_2).

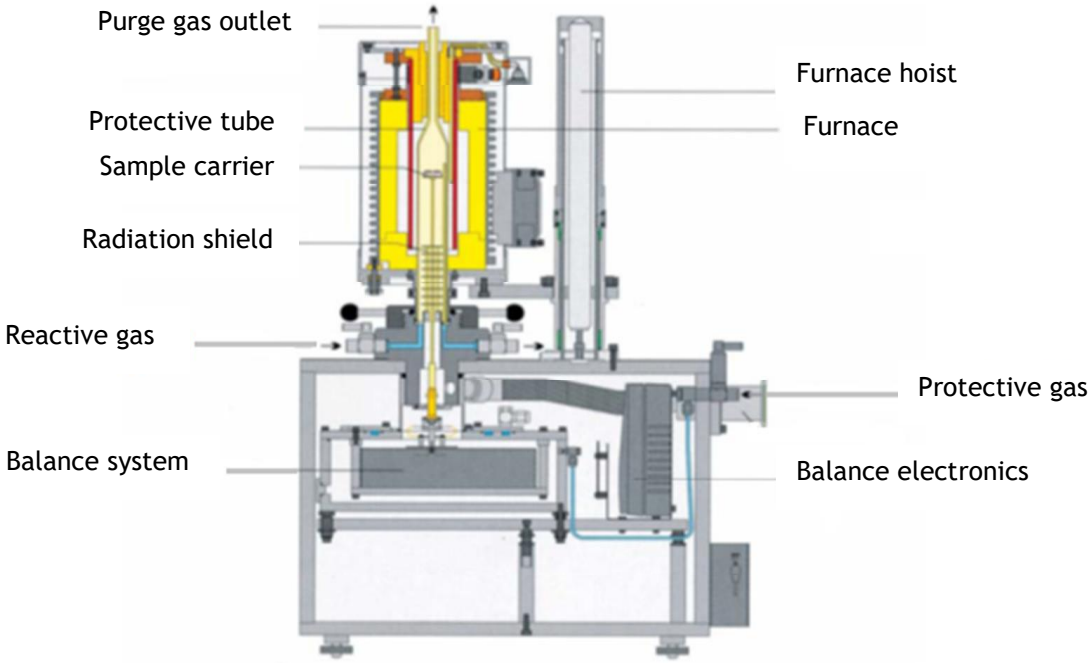

Fig.3.4 Schematic of the Netszch STA409CD [13].

Simultaneous thermal analysis (STA) generally refers to the simultaneous application of thermogravimetry analysis (TGA) and differential thermal analysis (DTA) to the same sample in a single instrument. The experiment conditions are exactly identical for the TGA and DTA signals (same atmosphere, gas flow rate, vapour pressure of the sample, heating rate, thermal contact to the sample crucible and sensor, radiation effect, etc.). The information gathered was enhanced by coupling the STA instrument to an Evolved Gas Analyzer (EGA), specifically a Mass Spectrometer (MS).

TGA is an important tool and can aid in determining the thermal stability of a material. In TGA, the sample is heated in a crucible which is typically alumina, platinum, nickel or stainless steel, with the weight loss of the sample recorded as a function of temperature.

Differential thermal analysis (DTA) is coupled to the TGA. DTA can be used to identify phase transition temperatures and also to identify if a reaction or transition is either exothermic or endothermic. In DTA, the crucible containing the sample is heated under identical conditions as the reference crucible, which is an empty crucible (crucible depends on the sample crucible material, so if an alumina crucible is used for the sample, then an empty alumina crucible is used for the reference). An empty crucible is used so that heat changes originating from the crucible can be taken into account, and that measured changes in the recorded thermal profile are attributed to the sample only. A schematic of the DTA arrangement is shown in Fig.3.5.

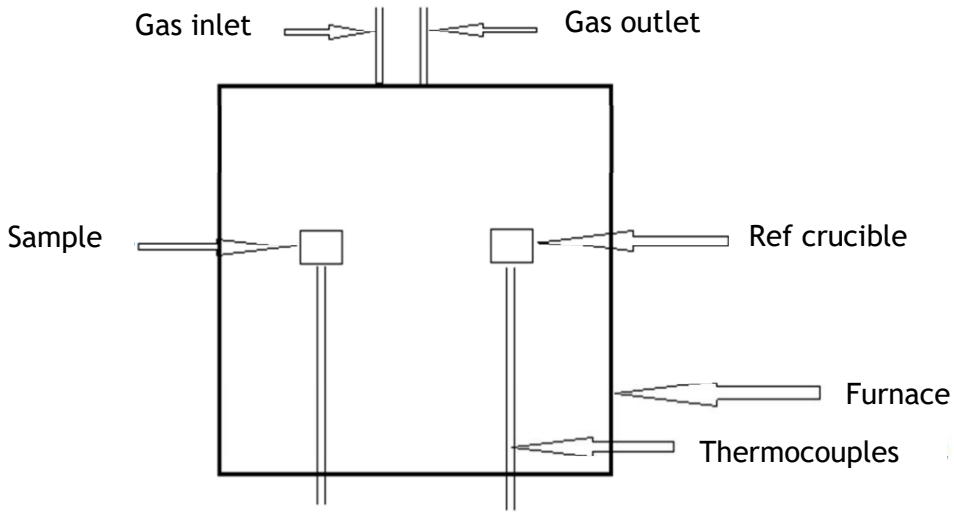

Fig.3.5 Schematic of the DTA arrangement.

A mass spectrometer typically consists of three components: the ion source, the mass analyser and the mass detector. The first process in a mass spectrometer is the vaporisation of the sample at the ion source. This involves the ionisation of the sample by electrons, produced by the filament, to a cation with the loss of an electron (where M is the sample):

$$M + e^- \rightarrow M^+ + 2e^- \qquad Eq.3.5$$

The detection of ions with different masses is achieved by varying the magnetic field used in the deflection process. After the selection of ions has occurred, the ions are focussed onto an ion collector where they are detected and also amplified. The mass

spectrum is then recorded by the mass spectrometry software and analysis of the mass spectrum undertaken.

The Mass Spectrometer used in this project, the Hiden HPR20 is a quadrupole mass analyser. The quadrupole mass analyser (Fig.3.6) was developed by Wolfgang Paul [14]. In a quadrupole mass analyser, there are four parallel quadrupole rods. These rods have a fixed DC (direct current) potential and alternating RF (radio frequency) factors, so that the ions produced by the ion source travel along the middle of the rods. Only ions with a particular m/z value (selected by the user) are stabilised and allowed to travel through to the mass detector, due to changes in the electrical fields. The RF factor is changed to allow other ions with other particular m/z values to be detected by the mass detector in order to build up a spectrum.

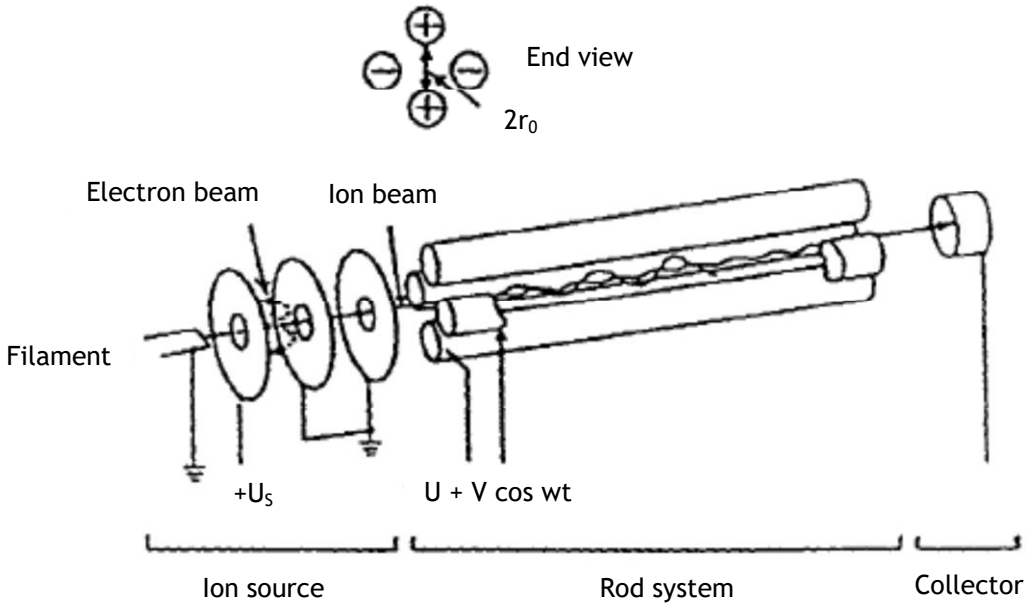

Fig.3.6 Quadrupole mass analyser developed by Wolfgang Paul. Reprinted with permission from [14]. Copyright 1990 John Wiley & Sons.

3.3.2 Sample Preparation

Before a sample could be heated and analysed in a TG-DTA experiment, a correction file is needed. This involves heating an empty sample pan using the conditions required for the sample being studied. The correction file contains the information about the heating conditions for the sample and the thermal profile of the sample

pan. The Mass Spectrometry is also run during the correction file to mimic the conditions of the sample when heated. Ar(g) was the carrier gas used for all measurements during this project.

The first step for running the sample is to place an empty pan onto the TGA and allowing the balance to stabilise to zero and the DTA value on the software to reach ~ (-1 mV). Once the balance is stabilised, the sample is added to the pan using a micro spatula. In a typical experiment, 30-40 mg of sample is used. The balance/furnace (fig.3.6) is then closed, and the balance allowed to stabilise and the DTA value allowed to rest at ~ (-1mV). Once this is the case, the relevant correction file is selected, and the sample is heated. Mass spectrometry data is also collected for the sample at the appropriate m/z values.

3.4 Scanning electron microscopy/Energy dispersive X-ray (EDX)

SEM, in combination with EDX, can be used to study the morphology of a sample and define the elements associated with interesting morphological features. The tungsten filament of the electron gun emits electrons, which are accelerated through a high voltage of 20 kV. These electrons are focused on a small spot on the surface (50–100 Å in diameter) by a condensing lens, requiring the sample to be run under vacuum to prevent bombardment from air particles from scattering the electron beam (Fig.3.7).

This beam then scans the sample–producing X-rays and secondary electrons, both of which are a result of the inelastic scattering of the electron beam by electrons in the material studied. The secondary electrons are used to create an image of the surface, which has a three-dimensional quality to it as the angle of the electron projection depends on the angle of the incoming beam. A back scattered electron profile is also detected, being produced by the elastic scattering of samples electrons. These two images are then combined to produce an overall image, which tends to appear brighter with higher atomic number atoms as they have the greater electron scattering.

To prevent charging of the non-conducting sample during the bombardment by electrons, the samples are usually sputter-coated in a thin layer of gold. Being a conductor, it dissipates any build-up of charge from the electron beam which can cause scanning faults and other image artefacts. Furthermore, being an element with a high atomic number, the coating by gold can enhance resolution of lighter

elements, by increasing backscattering and secondary electron emission near the samples surface.

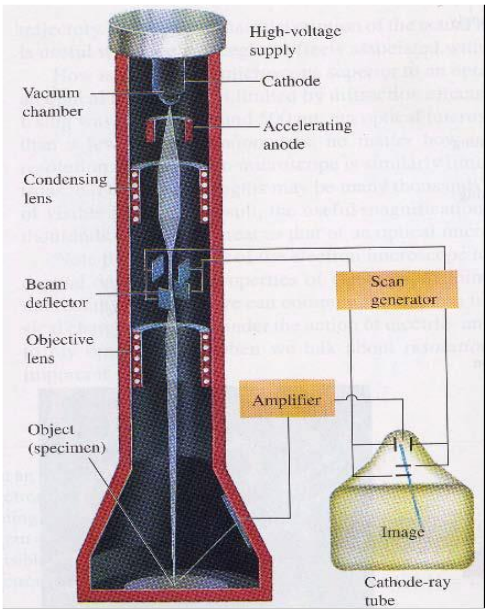

Fig.3.7 Schematic illustration of a scanning electron microscope [15].

EDX is a complementary technique, which scans the energy of the X-rays produced by the aforementioned inelastic scattering. This energy is characteristic of the material present and therefore EDX can be used to complete local elemental analysis. Unfortunately, only elements of a greater atomic mass than beryllium can be assessed in this way, as a Be window is used to screen the detector from higher energy X-rays. Therefore, composition of compounds containing lithium could not be carried out accurately, and this technique was only used for analysis of the synthesis of the magnesium hydroxide nanoparticles.

A Philips XL30 SEM-FEG has been used, operating at 20 KV in high vacuum mode with a working distance of 10 mm. An Oxford instruments EDX was attached to the side giving elemental analysis capability. Again, this microscope was only used in high vacuum work though it did have environmental mode capabilities. A standard SED was used to detect the electrons.

3.4.1 Sample preparation for SEM

The powdered samples are scattered or wiped across a circular double-sided carbon adhesive tab and attached to an aluminium slug before being inserted into the SEM.

In non-conducting samples, pre-treatment with an inert metallic layer, for example, gold is needed to reduce the build-up of charge on the surface due to secondary electron loss. The samples in this project, however, were sufficiently conducting through the carbon tab to avoid the need for sample coating.

SEM was performed at 20 KV, in high vacuum mode, with a typical working distance of 10 mm and spot size 3 or 4. Samples were loaded onto aluminium slugs using a double-sided adhesive carbon tabs which provided enough conduction to prevent the need for a coating procedure. EDX was used in conjunction with the SEM to ascertain approximate elemental ratios.

3.5 Size distribution calculation

SEM is a powerful technique for observation and characterisation of surfaces materials on a micro area, allowing the evaluation of their shape and size. The irregular shape of the particle presents a problem in particle size analyses. The particle size distribution measurement was studied by ImageJ software based on scanning electron microscopy images.

The first step in using ImageJ is the image calibration required to correlate the image dimensions in pixel to physical dimensions. The procedure consists in the drawing of a line over the scale bar of the image acquired by the SEM followed by the command “Analyze → Set Scale”. The Set Scale window was entered into the “Known Distance” box and changed the “Unit of Measurement” box in μm or nm. Image processing algorithms require a binary image that can be produced by converting the 8-bit image, that can display grey levels, by proper thresholding.

The procedure of obtaining the binary image consists in the use of the ImageJ's command “Threshold…”. Such a command by default produces the auto-threshold limits, wherein the lower limit is varied with the image and the higher limit was at the maximum of 255 grey levels. Use this tool to automatically or interactively set lower and upper threshold values. The scale bar was surrounded with rectangular selection and the contents was cleared (“Edit → Clear”). Proceeding with the correct threshold limits creates the required binary image. In fact, if the object is properly covered by thresholding, then accurate size measurement is automatically guaranteed as the image processing method is direct in principle.

The procedure of measurement is obtained by running the ImageJ's “Analyze particles” routine. The options “Exclude on Edges” and “Include Holes” were

selected in order to ensure including all whole particles and ignoring holes, if any after thresholding, in the particles of the image during analysis.

Particle area was determined using the Analyze Particle tool within the ImageJ software. This command processes the threshold binary image by identifying the particles and calculating their areas. The software reports the results individually in a table. Assuming that the particles were spherical, the diameters were calculated using Equation 3.7:

$$d = 2\sqrt{\frac{A}{\pi}} \qquad Eq.3.7$$

where *A* is the calculated area and *d* is the diameter of the particle. For particles that are not spherical, Equation 3.7 can still be used and will provide the equivalent spherical diameter of particles.

The software Origin can calculate automatically the most appropriate bin size. Once obtained the distribution, it could be useful to extrapolate the real mean values and the width of the distribution itself. The standard deviation of the whole population is indicative of how broad the distribution of particle is. The particle size distribution was exhibited on a histogram, and the data were fit with the log-normal distribution (Eq.3.8) [16, 17, 18] to determine the mean and standard deviation (SD) [19].

$$f(x) = \frac{1}{x\sqrt{2\pi}lnS_g} exp\left[-\frac{lnx - lnx_g{}^2}{2ln^2S_g}\right] \qquad Eq.3.8$$

where X_g is the geometric mean diameter and S_g is the geometric SD.

3.6 Diffuse reflectance UV-Vis (DR-UV-Vis) spectroscopy

Reflection describes the effect of light scattered back by a surface. Reflection is specular from an ideally planar surface without defects, at the light travelling back with an angle to the surface normal equivalent to the angle of incidence. Visible light specular reflection occurs from a mirror-like surface, whereas for all other surfaces the reflected light is scattered in all the possible directions, due to superficial roughness and imperfections. For opaque surfaces with negligible transmission, light can be absorbed or reflected. Measurement of diffuse reflection is hence useful for the determination of sample absorption.

3.6.1 Reflectance measurements

Fig.3.8 The Shimadzu UV-2600 UV-Vis spectrophotometer.

Reflectance measurements require an integrating sphere attachment (ISR-2600 Plus) to the UV-Vis spectrometer (Fig.3.8). The reflectance or the absorbance are measured as a function of the wavelength of the incident radiation as in normal UV-Vis spectrometry.

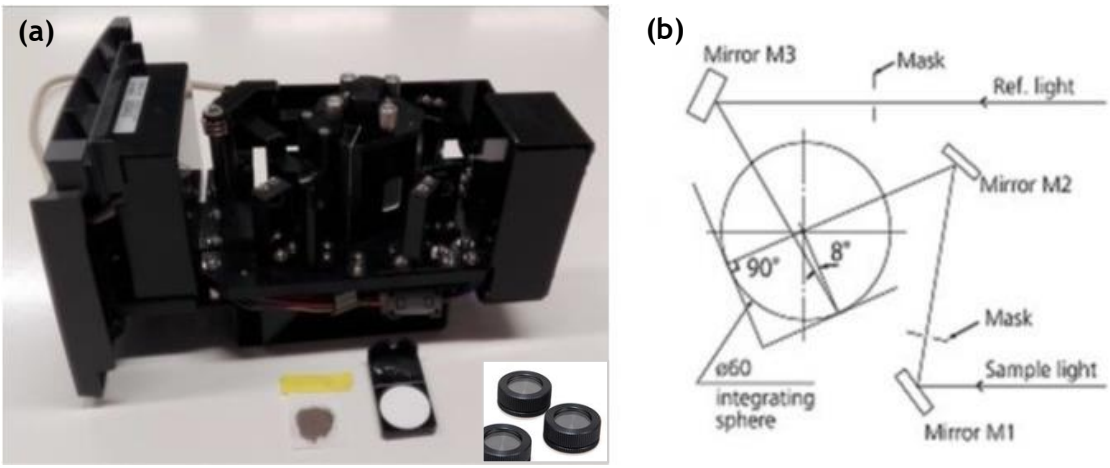

Fig.3.9 (a) Integrating sphere device, with $BaSO_4$ support and sample prepared for the measurement and (b) geometry of the integrating sphere (from Shimadzu).

In the integrating sphere (Fig.3.9), the inclination of the sample and the reference with respect to the incoming beam allows the specular reflectance to exit

undetected, with the diffuse reflectance is concentrated by the $BaSO_4$-coated inner walls of the sphere and collected by a photodiode. The beam is directed to the sample by a geometrical arrangement of parabolic mirrors. Barium sulphate is also used for the baseline determination, since it reflects all radiation within the operative range of the spectrometer (190-1300 nm).

3.6.2 Band gap calculation

The optical band gap represents the energy required for a photon to be absorbed by a material. The absorption of the photon and associated energy is equivalent to the difference between the conduction and valence band. The optical band gap is not equivalent to the electronic band gap, defined as the energy necessary to produce a non-bound couple of a hole and an electron.

The determination of the optical band gap in semiconductors is easily extrapolated from its absorption spectrum according to the process originally proposed by Tauc, David and Mott [20, 21]. The model, commonly known as Tauc's plot, proposes the proportionality between the band gap (E_g) and the absorption coefficient (α) of the material:

$$(h\nu\alpha)^{1/n} = A(h\nu - E_g) \qquad Eq.3.9$$

where h is the Planck constant, υ is the light frequency and A is a proportionality constant depending on the properties of the material. n is defined as power factor and its value depends on the nature of the optical transition probability [22]. Briefly, a transition is direct when it does not involve a change in momentum and the sole interaction occurs only between the photon and the electron.

A modification in momentum that defines an indirect transition involves an additional interaction with a phonon to promote the transition of the electron to the valence band. A transition can be classified as allowed or forbidden according to the momentum and energy conservation principle. The transition is generally allowed if the initial and final electronic states belong to two different bands; the intra-band transitions, in which the two states lay in the same band, are hence forbidden.

The values of *n* (listed for each transition in Table.3.2) derive from the description of the electronic bands through their wavefunctions in function of the imaginary part of the dielectric constant of the material [20].

Table.3.2 *Correlation exponential term for the Tauc expression.*

allowed	n=1/2	n=2
forbidden	n=3/2	n=3

A more refined model for the calculation of the band gap involves a description of optical properties considering the contribution of the scattering through the reflectance measurement. The Kubelka-Munk model is a two-flux model, with the light diffused by the sample travelling in the forward and reverse directions [23]. According to the Kubelka-Munk theory [24, 25], the absorption coefficient (*K*) in the optical transition expression is weighted by the scattering coefficient (*S*). The ratio of the two coefficients is a function of the diffuse reflectance emerging from a theoretically infinite thick and opaque layer (R_∞) [26]:

$$F(R_\infty) = \frac{K}{S} = \frac{(1 - R_\infty)^2}{2R_\infty} \qquad Eq.3.10$$

Where $F(R_\infty)$ is the Kubelka-Munk function, which can be replaced in the Tauc's expression (Eq.3.11) giving:

$$(h\nu \mathrm{F(R)})^{1/n} = A(h\nu - E_g) \qquad Eq.3.11$$

In both the Tauc and Kubelka-Munk model, the plot of $(h\nu \mathrm{F(R)})^{1/n}$ as a function of the incident radiation energy generally gives generally a sigmoidal curve for a semiconductor. The characteristic slope is fitted as a linear interpolation. The intersection of the slope with the x-axis ($h\upsilon$) directly provides the value of the band gap [27].

3.7 References

[1] Aaron Wold and Kirby Dwight, Solid State Chemistry, Synthesis, Structure, and Properties of Selected Oxides and Sulfides. *Chapman and Hall, Inc.*, New York, 1993, 1st ed. P19-26.

[2] M. Woolfson, F. Hai-fu. Physical and non-physical methods of solving crystal structures. Cambridge University Press., Cambridge, 1995, p **16**.

[3] M. G. Barker, M. J. Begley, P. P. Edwards, D. H. Gregory, S. E. Smith. *J. Chem. Soc. Dalton Trans.,* 1996, **1**.

[4] M. Ermrich, D. Opper. XRD for analyst, PANalytical GmbH, 2011, pp. **28**.

[5] N. Kourkoumelis. International Union of Crystallography, Commission on Powder diffraction, *Newsletter.*, 2005, **30**.

[6] G. Nolze, W. Kraus. *Powder Diffr.*, 1998, **13**, 256.

[7] A. Belsky, M. Hellenbrandt, V. L. Karen, P. Luksch. *Acta Crystallogr.*, 2002, B**58**, 364.

[8] A. C. Larson, R. B. Von Dreele. The General Structure Analysis System, Los Alamos National Laboratories, Report LAUR 086–748, LANL, Los Alamos, NM, 2000.

[9] B. H. Toby. *J. Appl. Crystallogr.,* 2001, **34**, 210.

[10] R. A. Young. The Rietveld Method. Oxford University Press, 1993.

[11] S. Z. D. Cheng, C. Y. Li, B. H. Calhoun, L. Zhu, W. W. Zhou. Thermal analysis: the next two decades. *Thermochimica Acta.*, 2000, **355(1-2)**, 59-68.

[12] T. Lever, P. Haines, J. Rouquerol, L. C. Edward, P. Van Eckeren, J. B. Donald. ICTAC nomenclature of thermal analysis (IUPAC Recommendations 2014). *Pure* and *Applied Chemistry.*, 2014, **86**, 545.

[13] Netszch STA409 PC product brochure accessed on 27th March 2012 at: http://www.netzschthermal-analysis.com/download/STA409CD_e.0306_18.pdf.

[14] W. Paul, *Angew. Chem. Int. Ed.*,1990, **29**, 739.

[15] R. Freedman, T. Sandin, A. Lewis-Ford, *University Physics: with Modern Physics*, Addison Wesely, USA, 2000, 10th Edition, 1282-1284.

[16] M. E. Gomez Yepes, L. V. Cremades. Characterization of wood dust from furniture by scanning electron microscopy and energy-dispersive X-ray analysis. *Industrial Health.*, 2011, **49**, 492–500.

[17] W. H. Walton. Feret's statistical diameter as measure of particle size. *Nature.*, 1948, **162**, 329–330.

[18] C. Igathinathane, S. Melin, S. Sokhansanj, X. Bi, C. J. Lim, L. O. Pordesimo, *et al.*, Machine vision-based particle size and size distribution determination of airborne dust particles of wood and bark pellets, Powder Technology., 2009, **196**, 202–212.

[19] Y. Endo. *Powder Technol.*, 2009, **193**, 154.

[20] J. Tauc, R. Grigorovici, A. Vancu. Optical Properties and Electronic Structure of Amorphous Germanium. *Phys. Status Solidi.*, 1966, **15**, 627-637.

[21] E. A. Davis, N. F. Mott. Conduction in non-crystalline systems V. Conductivity, optical absorption and photoconductivity in amorphous semiconductors. *Philos. Mag.*, 1970, **22**, 903-922.

[22] Y. Zhao, C. Li, X. Liu, F. Gu, H. Jiang, W. Shao, L. Zhang, Y. He. Synthesis and Optical Properties of TiO_2 Nanoparticles. *Mater. Lett.*, 2007, **61**, 79–83.

[23] A. B. Murohy. Modified Kubelka–Munk model for calculation of the reflectance of coatings with optically-rough surfaces. *J. Phys. D: Appl. Phys.*, 2006, **39**, 3571–3581.

[24] P. Kubelka, F. Munk. Ein Beitrag Zur Optik Der Farbanstriche. *Z. Techn. Physik*, (*German*)., 1931, **12**, 593-601.

[25] P. Kubelka. New Contributions to the Optics of Intensely Light-Scattering Materials. Part I. *J. Opt. Soc. Am.*, 1948, **38**, 448-457.

[26] G. Kortüm, W. Braun, G. Herzog. Principles and Techniques of Diffuse-Reflectance Spectroscopy. *Angew.*, 1963, **2**, 333-341.

[27] M. Nowak, B. Kauch, P. Szperlich. Determination of energy band gap of nanocrystalline SbSI using diffuse reflectance spectroscopy. *Rev. Sci. Instr.*, 2009, **80**, 046107.

Part-II Experimental Results

Chapter-4: Synthesis of Transition Metal Nitrides Results

4 Introduction

A number of transition metal nitrides have been prepared, mainly, Mn_4N, NbN, Mo_2N, TaN and ZrN nitrides. The synthesised nitride materials were characterised by powder X-ray diffraction. Phase identification was conducted by comparing data to the HighScore Plus database, and optical band gap has been calculated from reflectance measurements.

4.1 Powder X-ray diffraction results

Fig.4.1 shows the X-ray diffraction pattern of manganese nitride derived by the conventional heating method under ammonia gas. The peaks were indexed with the cubic phase of Mn_4N (ICSD#01-089-4804) and the hexagonal phase of $Mn_2N_{0.86}$ (ICSD#01-071-0200).

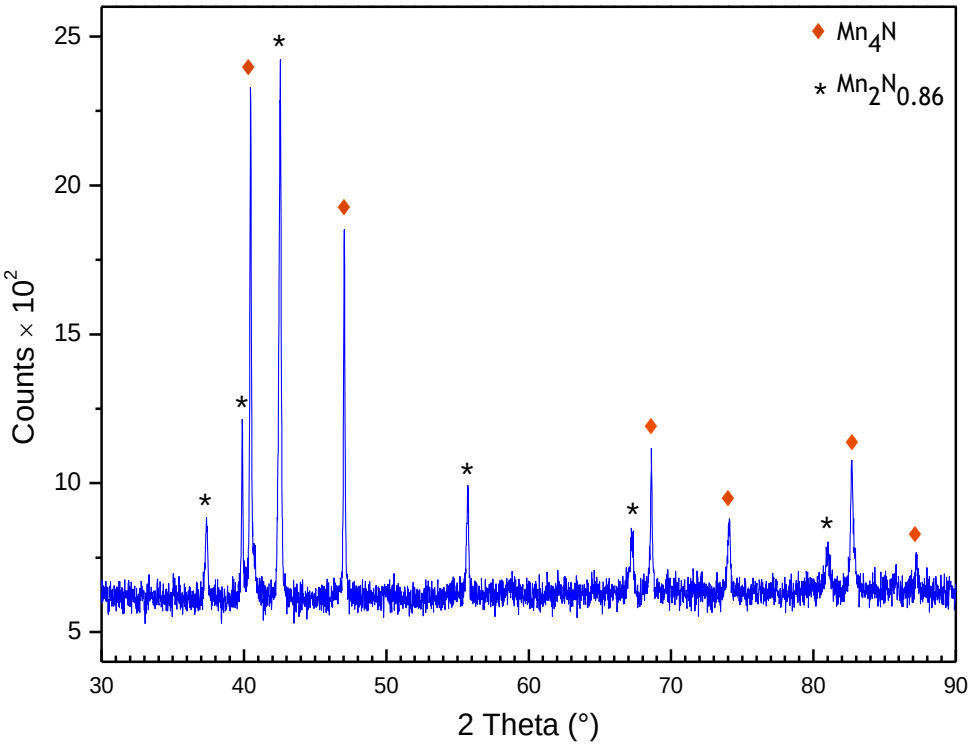

Fig.4.1 Powder X-ray diffraction pattern of Mn_4N. The $Mn_2N_{0.86}$ phase is indicated by the asterisks.

The typical X-ray diffraction pattern of chemically prepared NbN powder, in the range of $30° \leq 2\theta \leq 120°$, is shown in Fig.4.2. The major feature can be indexed as a hexagonal phase of NbN (PDF#03-065-3417) with the appearance of small and moderate quantity of tetragonal $Nb_8N_{6.8}$ (PDF#03-065-2252) as second phase.

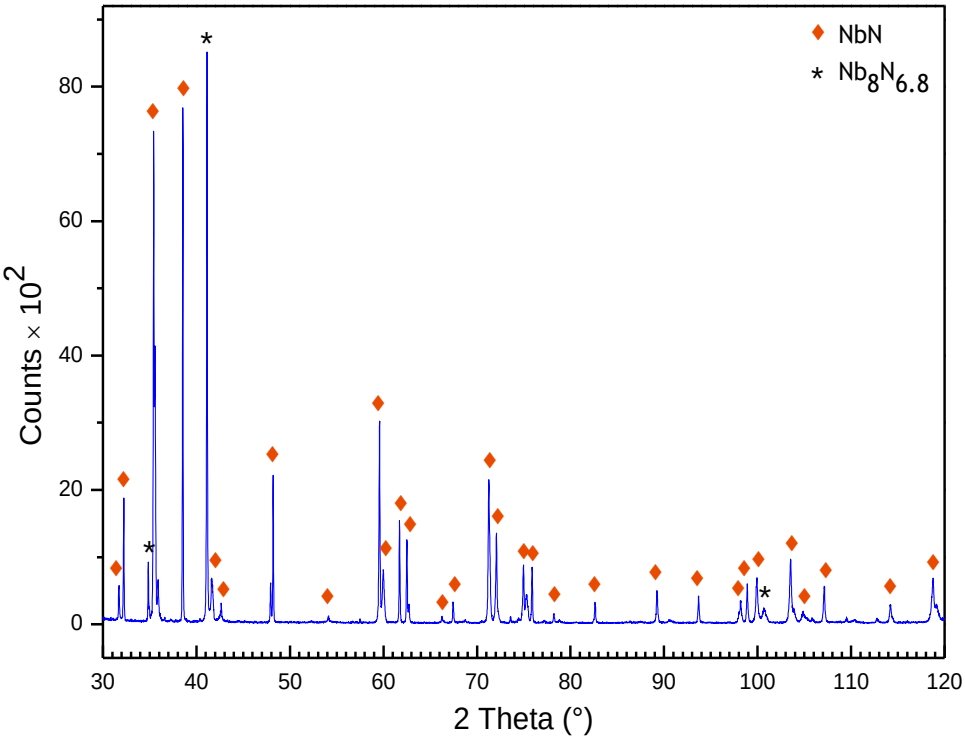

Fig.4.2 Powder X-ray diffraction pattern of NbN. The $Nb_8N_{6.8}$ phase is indicated by the asterisks.

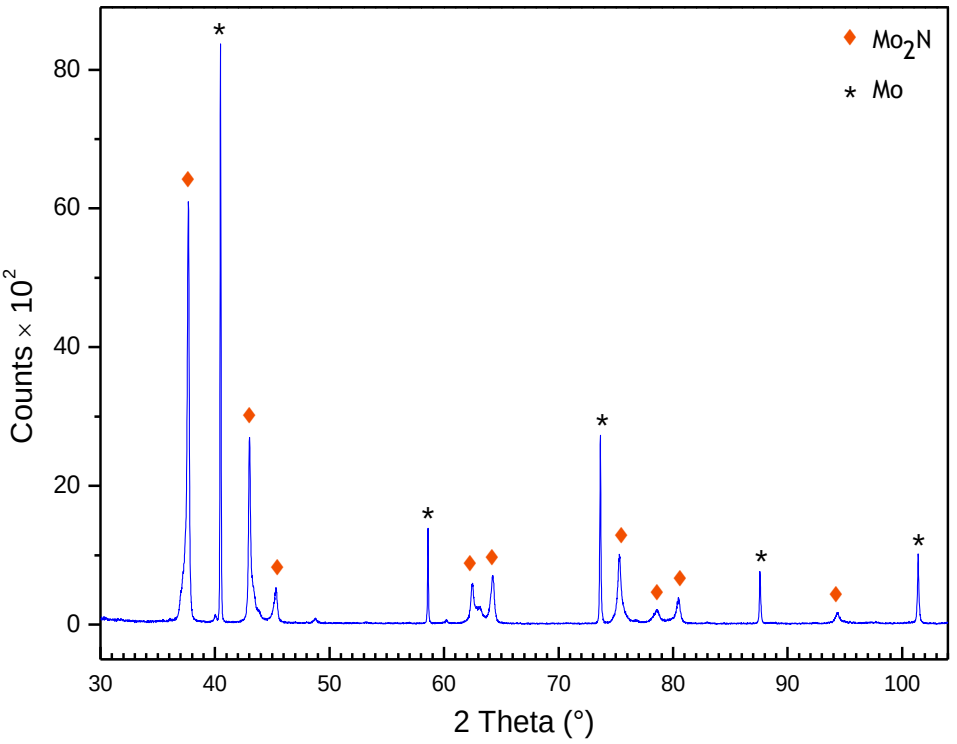

Fig.4.3 Powder X-ray diffraction pattern of Mo_2N. The Mo phase is indicated by the asterisks.

The diffraction pattern of synthesised Mo_2N shows peaks corresponding to the planes which matches with the pattern of Powder Diffraction File Database having the card No. 024-0768 with the most intense peaks occurring at diffraction angles, $2\theta = 37.6°$ and $43.05°$ which correspond to the (112) and (200) reflection planes, respectively. The diffraction at $2\theta = 40.5°, 58.6°, 73.6°, 87.6°$ and $101.4°$ can be identified as the $(111), (200), (211), (220)$ and (310) crystal planes of Mo (PDF#00-004-0809).

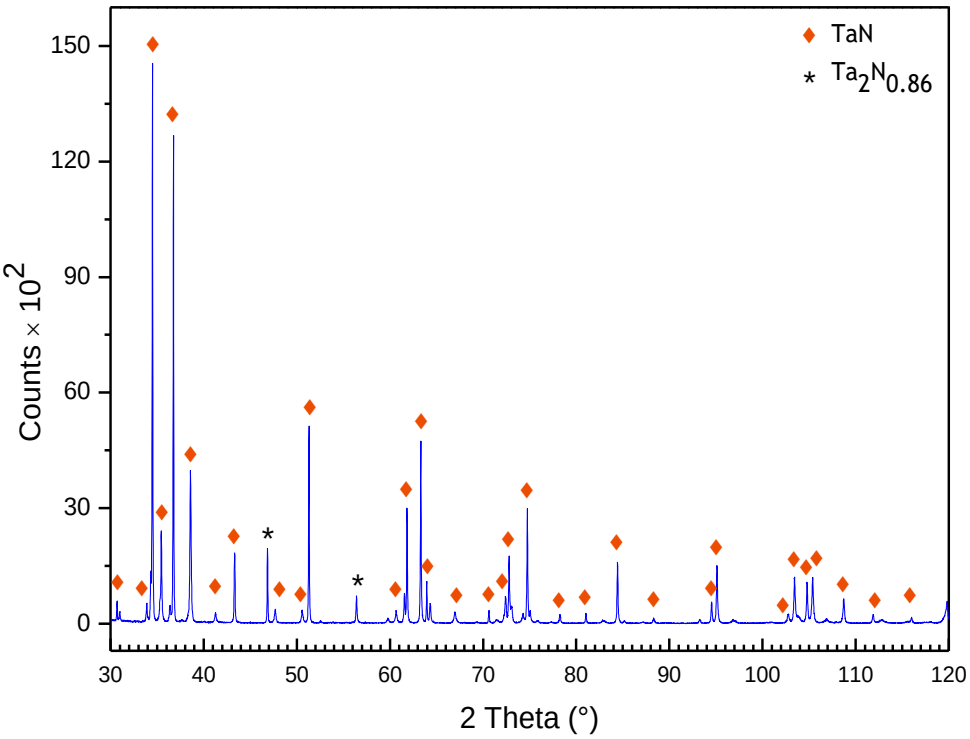

Fig.4.4 Powder X-ray diffraction pattern of TaN. The $Ta_2N_{0.86}$ phase is indicated by the asterisks.

The peaks recorded in Fig.4.4 match those of hexagonal TaN (PDF#00-039-1485) with the presence of slight impurity of hexagonal $Ta_2N_{0.86}$ (PDF#01-089-5199).

It was observed that the routes used for the synthesis of Mn_4N, NbN, Mo_2N and TaN produced a nitrogen deficient nitrides of formula $Mn_2N_{0.86}$, $Nb_8N_{6.8}$, and $Ta_2N_{0.86}$, as second phases, which is likely these materials formed are sub-stoichiometric nitrogen. This low value may be due to the refractory nature of these metal nitrides. This may also correspond to some nitrogen sub-stoichiometry as many transition metal nitrides are interstitial compounds and are metal rich, which they are known to tolerate wide ranges in composition [1]. It should be noted that some nitrogen loss may occur prior to analysis.

As-prepared ZrN was a fine, yellow/brown powder. In a typical synthetic method with an appropriate choice of conditions, the nonthermal plasma reaction generates crystalline phase-pure ZrN (PDF#03-065-9412). Most importantly, no oxide or hydroxide impurities have been detected.

Manually fitting the background using 12 coefficients gave the best fit. The experimental pattern fits well with the theoretical pattern as displayed in Fig.4.5. The main phase was indexed to a cubic cell (Space group No.225: $Fm\bar{3}m$). Rietveld refinement yielded lattice parameters of a=4.58093(4) Å and a cell volume of 96.131(2) Å^3. Selected Rietveld refinement data and atomic parameters are presented in Tables 4.1 and 4.2. Estimated standard deviation (esd) values are shown in parentheses.

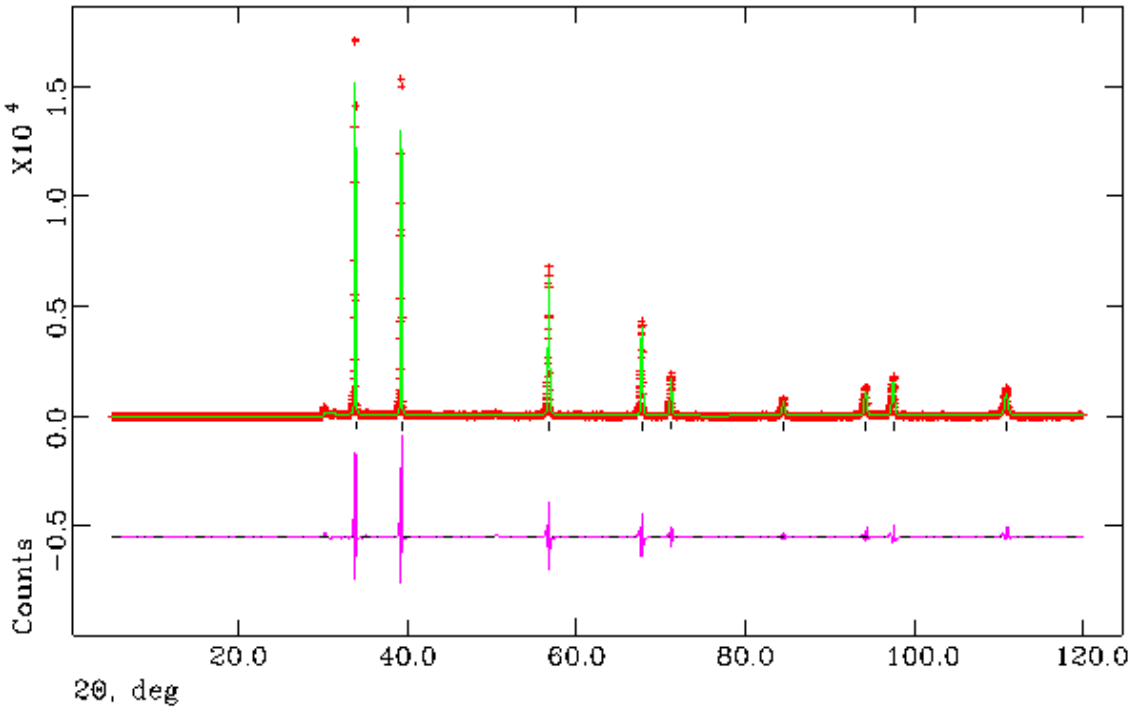

Fig.4.5 Observed-calculated-difference (OCD) profile plot from the Rietveld refinement for ZrN. Observed data are shown in red (crosses), calculated (green solid line) and the difference between the two curves (pink). Black tickmarks correspond to peak positions of cubic ZrN.

Table.4.1 *Selected Rietveld refinement data from PXD data for ZrN.*

ZrN		
Phase		ZrN
Crystal System		Cubic
Space Group		*Fm-3m(225)*
Unit cell parameters/Å	a	4.58093(4)
	b	4.58093(4)
	c	4.58093(4)
Volume/Å^3		96.131(2)
Z		4
Formula Weight/g		356.154
Density ρ_x/gcm^{-3}		6.152
No of observations		5385
No of variables		25
R_{wp}		0.2933
R_p		0.2379
χ^2		12.93

Table.4.2 *Atomic parameters of ZrN.*

Atom/Site	**x**	**y**	z	**Occupancy**	**U_{iso} x 100/Å^2**
N/4a	0	0	0	1	0.38(23)
Zr/4b	0.5(0)	0.5(0)	0.5(0)	1	1.21(2)

The PXD data of ZrN were used in the structural refinement via the Rietveld method. It is clear that production of pure ZrN is fully achieved with crystalline face centred cubic (FCC), rock-salt structure $(Fm\bar{3}m)$ and space group (225) as stated above. The structure was presented in Fig.4.6, whereby the zirconium atoms (Zr) large pink spheres occupy the interstitial octahedral sites and nitrogen atoms (N) with small blue spheres accommodate metal vacancies. The Zr—N distance was found to be 2.2905 Å.

Bond Zr—N = 2.2905 Å

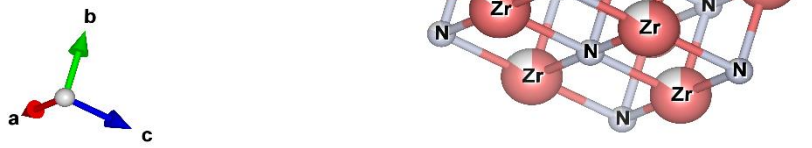

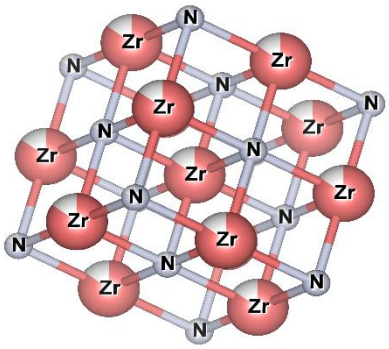

Fig.4.6 Crystal structure of synthesised ZrN has been displayed using VESTA software. The Zr atoms are coloured pink and the N atoms are blue.

4.2 Band gap calculation

The diffuse reflectance is measured as a function of the wavelength of the incident radiation as in normal UV-Vis spectrometry within the operative range of 190-1300 nm. The determination of the optical band gap is easily extrapolated from its absorption spectrum according to the process originally proposed by Tauc, David and Mott [2, 3]. Tauc's plot proposes the proportionality between the band gap (E_g) and the absorption coefficient (α) of the material.

$$(\alpha h\nu)^{1/n} = A(h\nu - E_g) \qquad Eq.4.1$$

Where h is the Plank constant, ν is the light frequency and A is a proportionality constant depending on the properties of the material. n defined as power factor and its value depends on the nature of the optical transition probability [4]. The value of n derive from the description of the electronic bands through their wavelength in function of the imaginary part of the dielectric constant of the material [3].

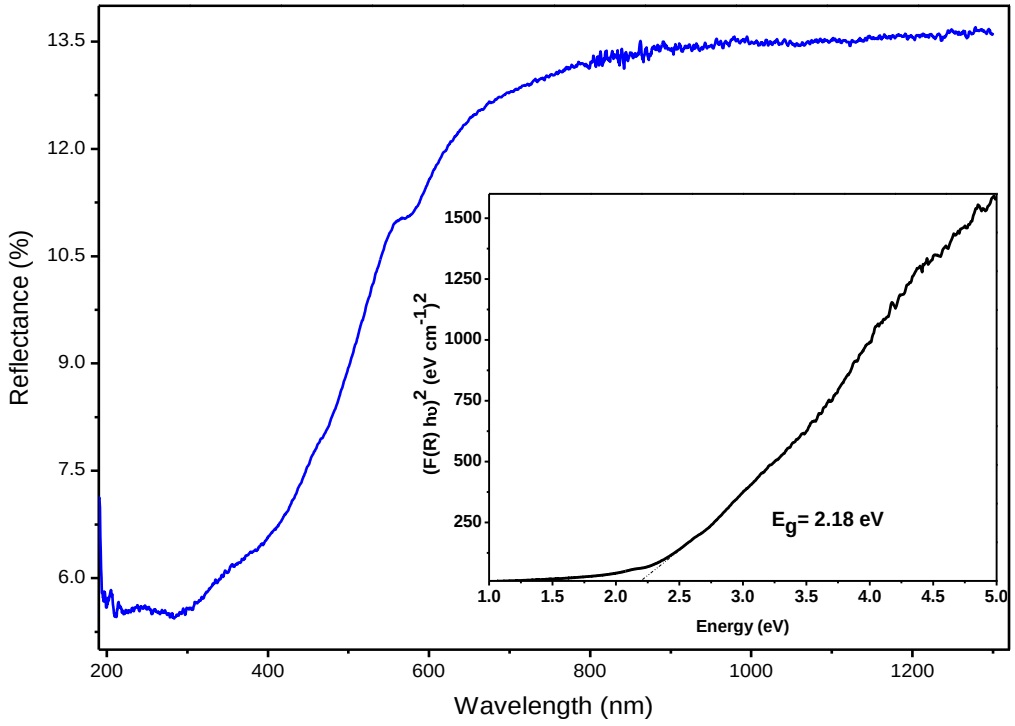

Fig.4.7 UV-Vis spectrum of Mn_4N with Tauc plot for band gap determination.

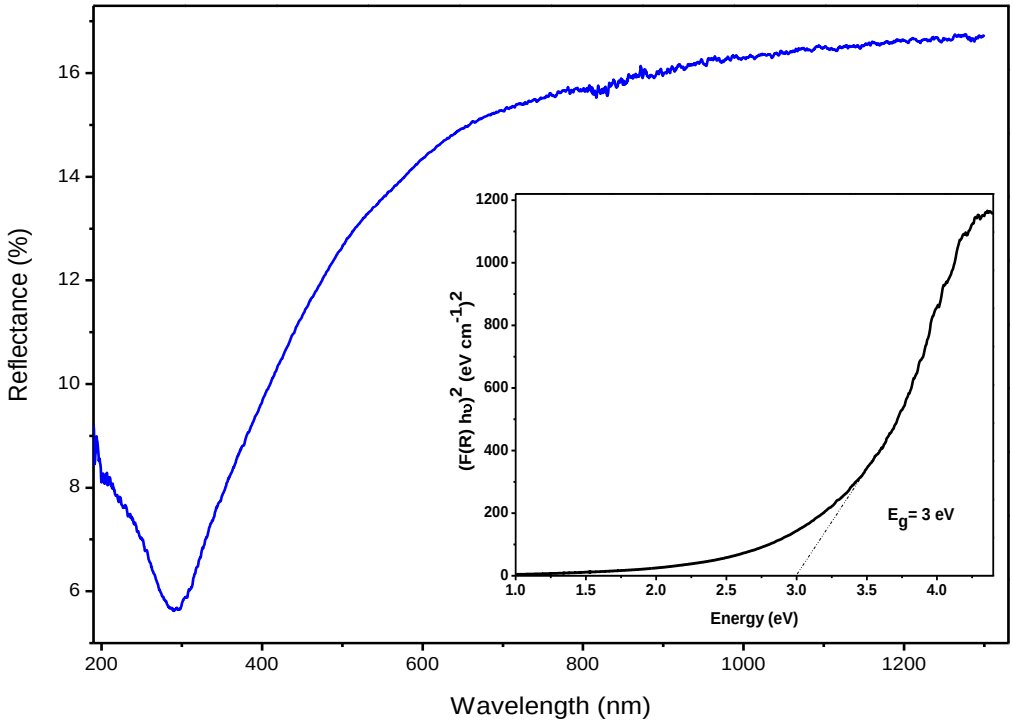

Fig.4.8 UV-Vis spectrum of NbN with Tauc plot for band gap determination.

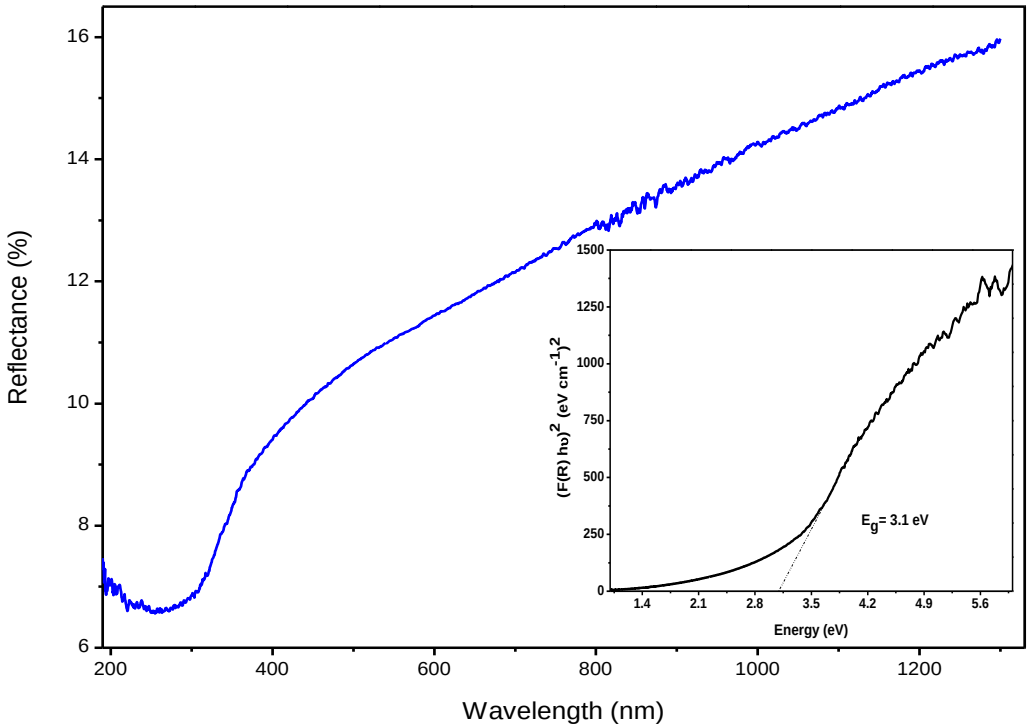

Fig.4.9 UV-Vis spectrum of Mo_2N with Tauc plot for band gap determination.

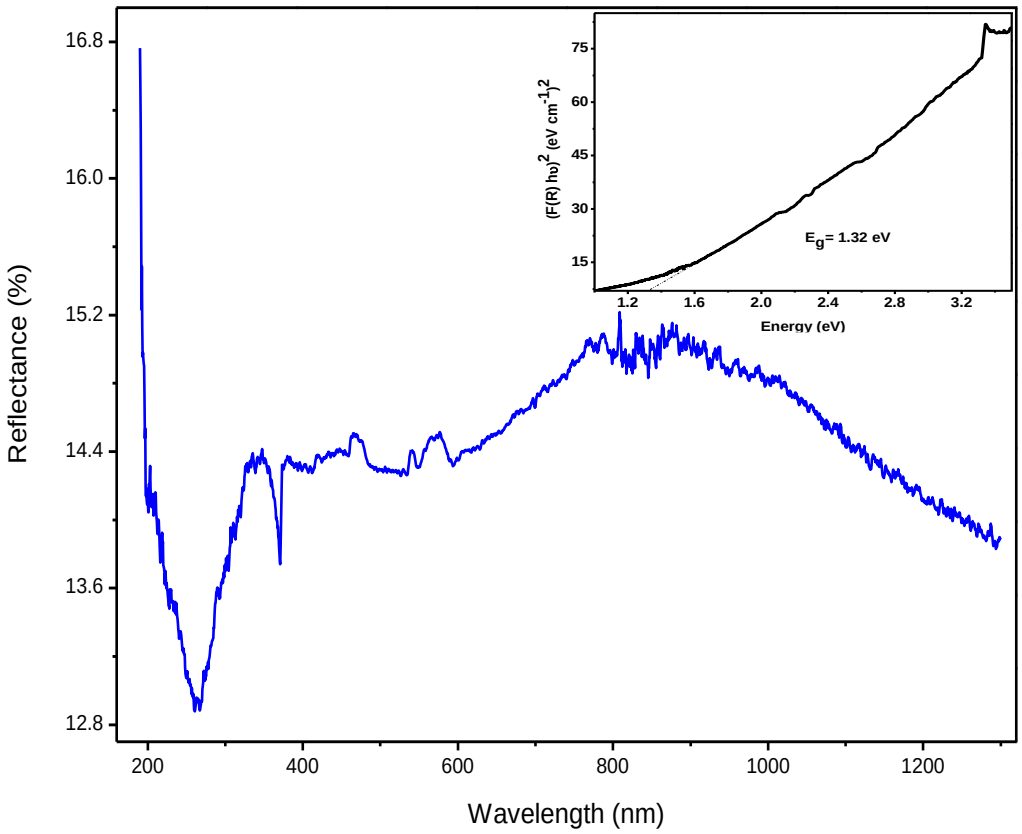

Fig.4.10 UV-Vis spectrum of TaN with Tauc plot for band gap determination.

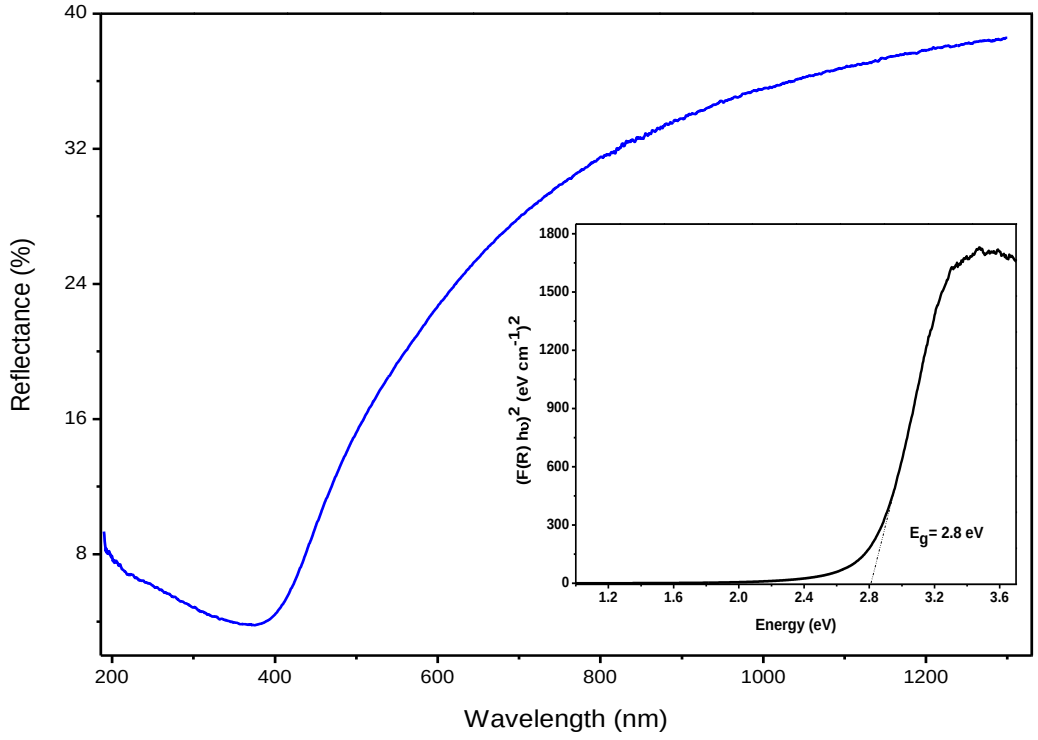

Fig.4.11 UV-Vis spectrum of ZrN with Tauc plot for band gap determination.

According to the Kubelka-Munk theory [5, 6] and Tauc plot of $(F(R)h\nu)^{1/n}$ as a function of the incident radiation energy, the characteristic slop is fitted as a linear interpolation. The intersection of the slop with the x-axis ($h\nu$) directly provides the value of the band gap [7].

Optical band gaps obtained from the reflectance data on synthesised Mn_4N, NbN, Mo_2N, TaN, ZrN nitride materials were estimated to be 2.18 eV, 3 eV, 3.1 eV, 1.32 eV and 2.8 eV, respectively, as shown in Fig.4.6, 4.7, 4.8, 4.9 and 4.10.

4.3 References

[1] I. P. Parkin, A. M. Nartowski. Solid state metathesis routes to group IIIa nitrides: comparison of Li_3N and Mg_3N_2 as nitriding agents. *Journal of Polyhedron.*, 1998, **17(16)**, 2617-2622.

[2] E. A. Davis, N. F. Mott. Conduction in non-crystalline systems V. Conductivity, optical absorption and photoconductivity in amorphous semiconductors. *Journal of Philosophical Magazine.*, 1970, **22(179)**, 903-922.

[3] J. Tauc, A. Grigorovici, A. Vancu. Optical properties and electronic structure of amorphous germanium. *Journal of Physica Status Solidi (b).*, 1966, **15**, 627-637.

[4] Y. Zhao, C. Li, X. Liu, F. Gu, H. Jiang, W. Shao, Li. Zhang, Y. He. Synthesis and optical properties of TiO_2 nanoparticles. *Journal of Materials Letters.*, 2007, **61(1)**, 79-83.

[5] P. Kubelka, F. Munk. Ein Beitrag Zur Optik Der Farbanstriche. *Journal of Zeitschrift für Technische Physik*, German., 1931, **12**, 593-601.

[6] P. Kubelka. New contributions to the optics of intensely light-scattering materials. Part I. *Journal of the Optical Society of America.*, 1948, **38(5)**, 448-457.

[7] M. Nowak, B. Kauch, P. Szperlich. Determination of energy band gap of nanocrystalline SbSI using diffuse reflectance spectroscopy. *Journal of Scientific Instruments.*, 2009, **80**, 046107.

Chapter-5: Synthesis of Li_3N and Mg_3N_2 Results

5 Introduction

Li_3N and Mg_3N_2 have been synthesised and studied. Structural refinements performed against powder X-ray diffraction data were conducted using General Structure Analysis System (GSAS). The least-square refinements were carried out until the best fit was obtained between the entire observed powder diffraction pattern taken as a whole and the entire calculated pattern based on the published structures as starting models. The major parameters refined were scale factors, zero shifts, unit cells, Pseudo-voigt peaks, shape, and profile parameters.

5.1 Synthesis of Li_3N results

5.1.1 Powder X-ray diffraction

The reaction between Li metal and nitrogen gas to form Li_3N occurred spontaneously. Li metal foil was left in a nitrogen-filled glovebox, and after 3 days of exposure, the color of the Li foil changed from white to black. The as-obtained powder was heated at 200 °C for around 24 h to ensure a complete reaction. During the course of the experiment, N_2 gas was flowed through the furnace and paraffin bubbler heating the crucible allowed for reaction temperature 200 °C to be reached. Once cooled, the crucible and its content were removed from the furnace and transferred to a glovebox where they were opened using pipe cutter, which allowed the crucible lid to be removed cleanly without polluting the sample. The black powder of Li_3N turned purple/red with lustrous effect after annealing process in the same atmosphere. The final powder was thoroughly mixed and ground together using an agate pestle and mortar. The crystallinity and phase purity of the annealing powder after grinding was then determined by powder X-ray diffraction.

All the diffraction peaks of the resulting powder can be readily indexed to alpha-Li_3N exhibiting strong intensity, indicating the high crystallinity of the powder sample. Weak peaks of Beta-Li_3N were additionally observed. This may be due to the pressure induced phase transformation during the grinding process [1]. No other impurities, such LiOH and Li_2O, were detected by PXD due to its limited sensitivity.

The experimental powder X-ray diffraction data for synthesised Li_3N was refined via the Rietveld method in order to obtain weight percentage values for alpha and beta Li_3N phases. The models for each of the calculations were obtained from the online Inorganic Crystal Structure Database (ICSD) and PowderCell 2.4 was used to obtain a visual comparison between the experimental and theoretical models. The

refinement was carried out using structural parameters of alpha-Li_3N in hexagonal symmetry [$Space\ group\ No.\ 191: P6/mmm, ICSD\#34779$], and beta-$Li_3N$ in hexagonal symmetry [$Space\ group\ No.\ 194: P63/mmc, ICSD\#156889$]. The observed-calculated-difference (OCD) profile plot is shown in Figure 5.1. Selected Rietveld refinement data and atomic parameters are presented below in Tables 5.1, 5.2 and 5.3. Estimated standard deviation (esd) values are shown in parentheses.

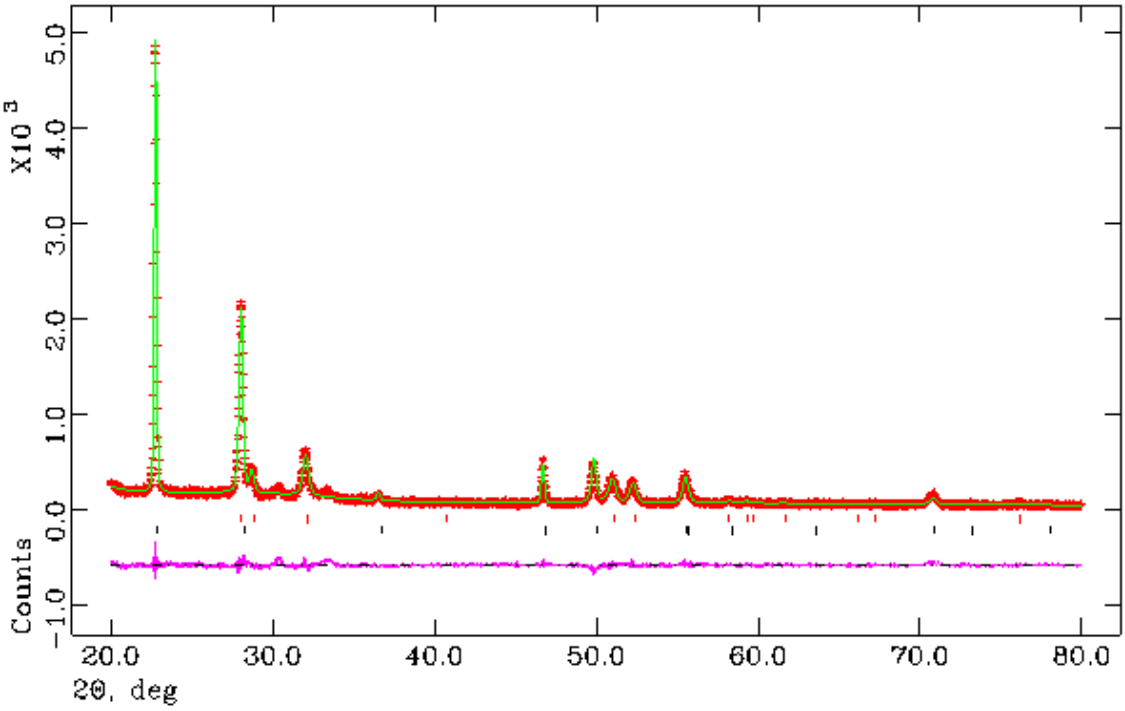

Fig.5.1 Observed (crosses), Calculated (solid line) and difference curves (bottom line) (OCD) plot for the structural refinement of Li_3N. The black tick marks are reflections from α-Li_3N and the red thick marks are reflections from β-Li_3N.

Table.5.1 *Selected Rietveld refinement data from PXD data of synthesised Li_3N.*

Li_3N			
Phases		α-Li_3N	β-Li_3N
Phase Fraction/wt.%		70.37(15)	29.63(29)
Crystal System		Hexagonal	Hexagonal
Space Group		*P6/mmm(191)*	*P63/mmc(194)*
Unit cell parameters/Å	a	3.6447(1)	3.5724(3)
	b	3.6447(1)	3.5724(3)
	c	3.8737(1)	6.3417(6)
Volume/$Å^3$		44.566(3)	70.091(13)
Z		2	4
Formula Weight/g		24.301	55.423
Density ρ_x/gcm^{-3}		0.905	1.313
No of observations		3589	
No of variables		44	
R_{wp}		0.1086	
R_p		0.0801	
χ^2		1.685	

Table.5.2 *Atomic parameters of α-Li_3N.*

Atom/Site	**x**	**y**	z	**Occupancy**	**U_{iso} x 100/$Å^2$**
Li1/1b	0	0	0.5(0)	0.573(9)	16.03(57)
Li2/2c	0.3333(0)	0.6667(0)	0	0.812(5)	11.15(19)
N/1a	0	0	0	0.647(3)	10.30(13)

Table.5.3 *Atomic parameters of β-Li_3N.*

Atom/Site	x	y	z	Occupancy	U_{iso} x 100/Å^2
Li1/2b	0	0	0.25(0)	0.879(16)	6.63(52)
Li2/4f	0.3333(0)	0.6667(0)	0.5915(15)	0.651(10)	7.80(33)
N/2c	0.3333(0)	0.6667(0)	0.25(0)	0.898(6)	10.26(20)

Rietveld refinement of the diffraction data yielded lattice parameters of a=3.6447(1), c=3.8737(1) for α-Li_3N, and a=3.5724(3), c=6.3417(6) for β-Li_3N. A cell volume of 44.566(3) and 70.091(13) were obtained, respectively. The agreement indices in the simulated pattern gives the best fit value of weighed R_p-R_{wp} and goodness of fit-χ^2=1.685 with 70.37(15) % of α-Li_3N and 29.63(29) % of β-Li_3N phase fractions.

5.1.2 Band gap calculation

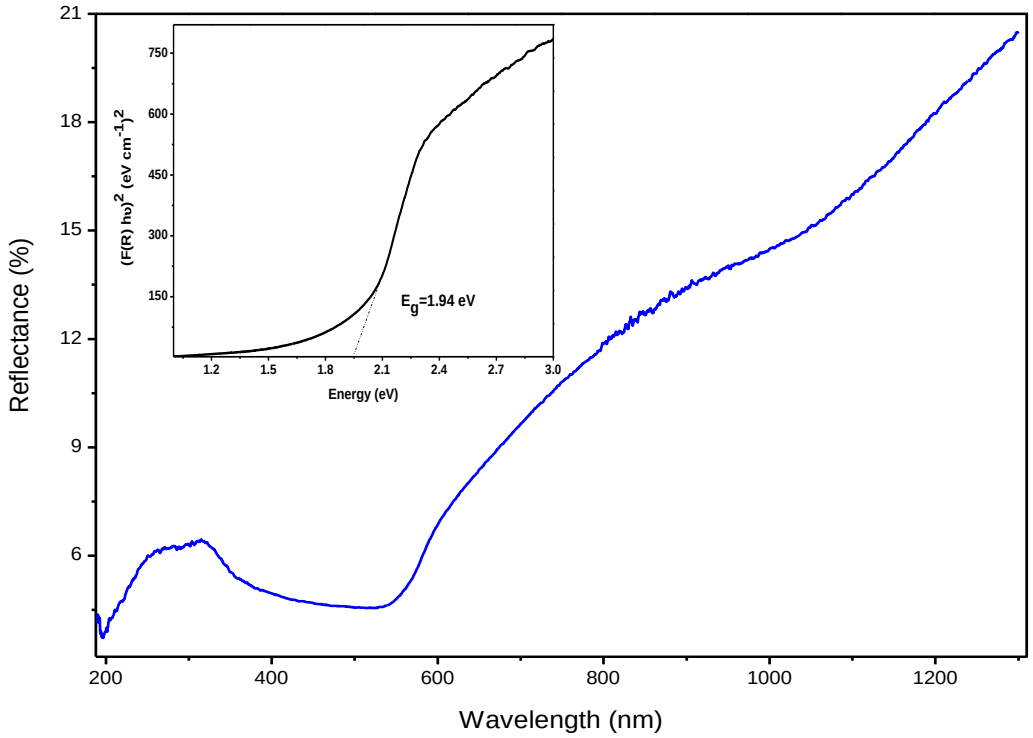

Fig.5.2 UV-Vis spectrum of Li_3N with Tauc plot for band gap determination.

Energy gap of the as-obtained Li_3N has been evaluated from the reflectance measurements of the visible light wavelength between 200 and 1300 nm. The calculated optical band gap was found to be 1.98 eV as shown in Fig.5.2, which is in good agreement with the literature value [2, 3].

5.2 Synthesis of Mg_3N_2 results

5.2.1 Powder X-ray diffraction

Mg_3N_2 synthesis was attempted by direct nitridation reaction of Mg powder with N_2 gas at a heating rate of 2°C/min for 3 h at a temperature ranging from 650°C to 1150°C.

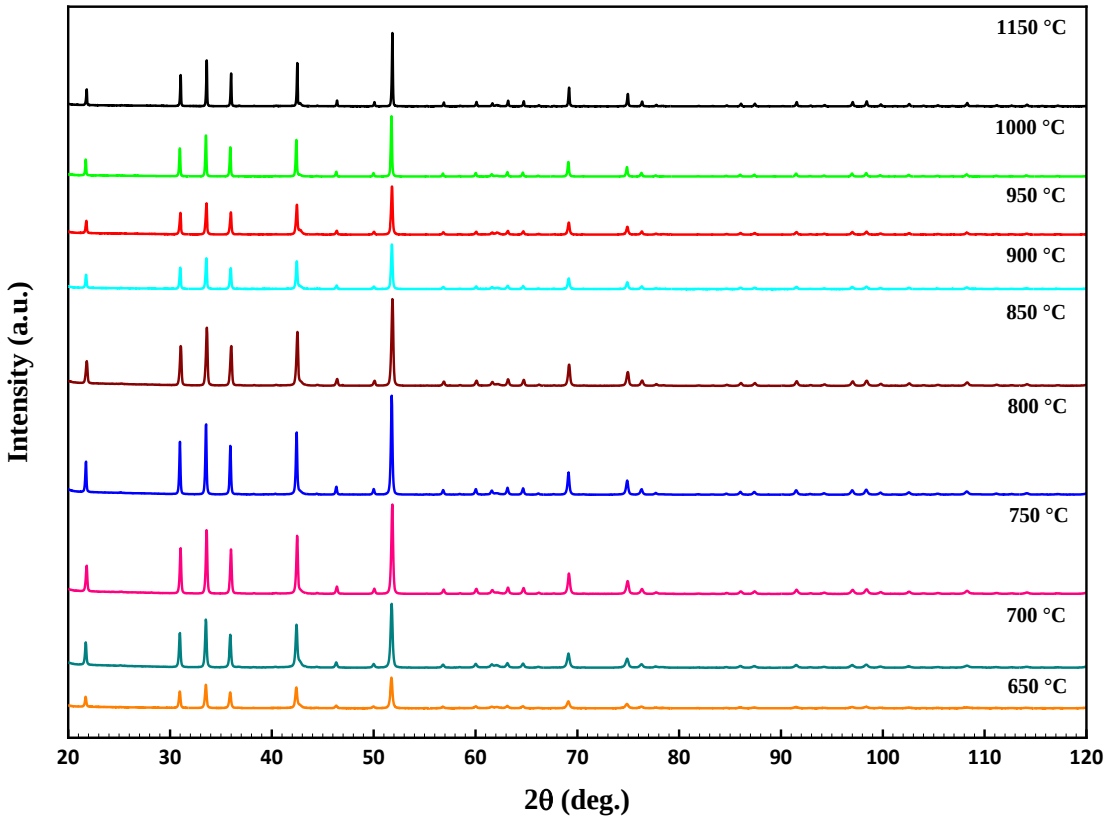

Fig.5.3 Powder XRD patterns comparing the Mg_3N_2 compounds obtaining by varying temperatures in the 650-1150°C range under N_2 atmosphere and heating rate of 2°C/min for 3 h.

Synthesised Mg_3N_2 was a fine yellow powder. Powder XRD (Fig.5.3) was employed to characterize the final product results. All the peaks can be well-indexed to be a pure phase of Mg_3N_2 for the entire set of the as-formed compounds obtained at various temperatures, which suggests that almost all Mg atoms have turned into Mg_3N_2. This was considered a positive result as no oxide was formed. It is clear in the figure that all peaks fairly correspond to the data of Mg_3N_2 powder recorded in the International Centre for Diffraction Data PDF database (Card No. 00-035-0778). This result is in agreement with previous studies of Fujian Zong *et all* [4].

Structure refinement was carried out from powder XRD data using the Mg_3N_2 cubic model in the $Ia\bar{3}$ space group suggested from the online ICSD database (No. 23522). A very slight MgO impurity, undetected by PXRD, was found to be present in all synthesised samples and included as a second phase in the refinement. This may have been caused by a poor airtight seal or by oxide present in the taps of the reaction pot. The Calculated, Observed, and Difference (COD) plots with selected refinement data are shown below.

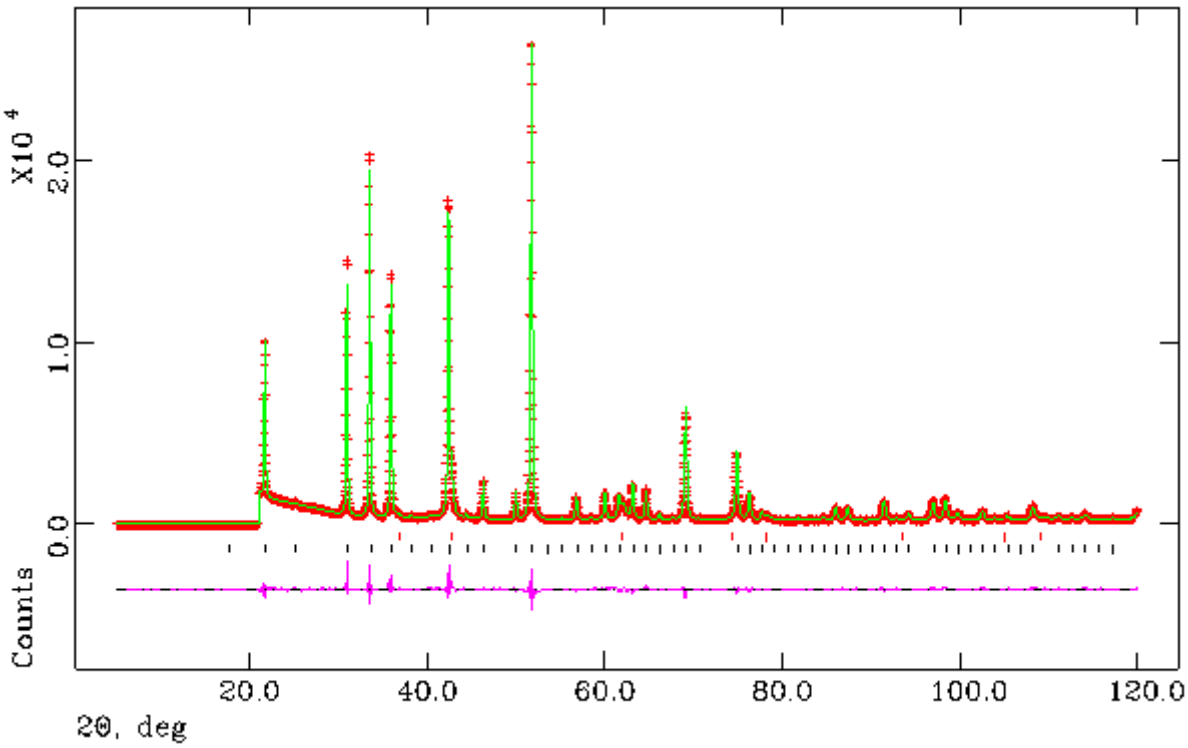

Fig.5.4 Rietveld refinement for Mg_3N_2 powder synthesised at 650°C. Observed (crosses), calculated (solid line) and difference curves (bottom line) are shown for comparison. Vertical bars (I) correspond to Bragg positions of Mg_3N_2 (black) and MgO (red) phases respectively from bottom to top.

Table.5.4 *Selected Rietveld refinement data from PXD data of sample (1) synthesised at 650°C.*

Sample (1) - 650°C			
Phases		Mg_3N_2	MgO
Phase Fraction/wt.%		90.50(2)	9.5(1)
Crystal System		Cubic	Cubic
Space Group		*Ia-3(206)*	*Fm-3m(225)*
Unit cell parameters/Å	a	9. 96797(7)	4. 2317(4)
	b	9. 96797(7)	4. 2317(4)
	c	9. 96797(7)	4. 2317(4)
Volume/$Å^3$		990.42(2)	75.78(2)
Z		48	48
Formula Weight/g		1642.324	158.577
Density ρ_x/gcm^{-3}		2.754	3.475
No of observations		5923	
No of variables		50	
R_{wp}		0.0627	
R_p		0.0486	
χ^2		3.075	

Table.5.5 *Atomic parameters of Mg_3N_2 (sample 1).*

Atom/Site	x	y	z	Occupancy	U_{iso} x 100/$Å^2$
Mg/48e	0.38940(7)	0.15247(6)	0.38203(8)	0.987(2)	1.95(1)
N1/8b	0.25(0)	0.25(0)	0.25(0)	0.166(13)	5.16(15)
N2/24d	-0.03062(16)	0	0.25(0)	0.500(4)	2.06(6)

Table.5.6 *Atomic parameters of MgO (sample 1).*

Atom/Site	x	y	z	Occupancy	U_{iso} x 100/$Å^2$
Mg/4a	0	0	0	1	1.31(9)
O/4b	0.5(0)	0.5(0)	0.5(0)	1	3.47(20)

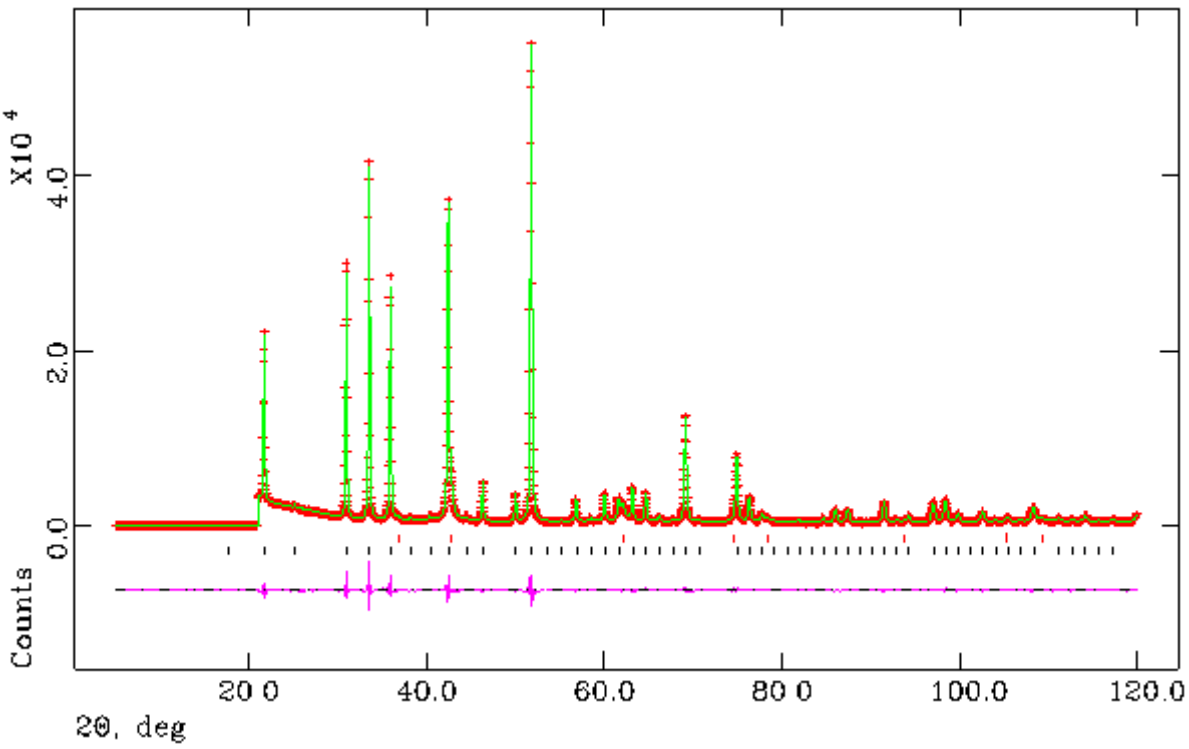

Fig.5.5 Rietveld refinement for Mg_3N_2 powder synthesised at 700° C. Observed (crosses), calculated (solid line) and difference curves (bottom line) are shown for comparison. Vertical bars (I) correspond to Bragg positions of Mg_3N_2 (black) and MgO (red) phases respectively from bottom to top.

Table.5.7 *Selected Rietveld refinement data from PXD data of sample (2) synthesised at 700°C.*

Sample (2) - 700°C			
Phases		Mg_3N_2	MgO
Phase Fraction/wt.%		90(1)	10(1)
Crystal System		Cubic	Cubic
Space Group		*Ia-3(206)*	*Fm-3m(225)*
Unit cell parameters/Å	a	9.96801(6)	4. 2215(3)
	b	9.96801(6)	4. 2215(3)
	c	9.96801(6)	4. 2215(3)
Volume/$Å^3$		990.43(1)	75.23(1)
Z		48	48
Formula Weight/g		1644.678	177.556
Density ρ_x/gcm^{-3}		2.757	3.919
No of observations		2961	
No of variables		71	
R_{wp}		0.0517	
R_p		0.0403	
χ^2		4.156	

Table.5.8 *Atomic parameters of Mg_3N_2 (sample 2).*

Atom/Site	**x**	**y**	**z**	**Occupancy**	**U_{iso} x 100/$Å^2$**
Mg/48e	0.38936(8)	0.15235(7)	0.38232(9)	0.986(1)	0.56(1)
N1/8b	0.25(0)	0.25(0)	0.25(0)	0.166(9)	1.39(13)
N2/24d	-0.03087(18)	0	0.25(0)	0.500(4)	1.78(6)

Table.5.9 *Atomic parameters of MgO (sample 2).*

Atom/Site	x	y	z	Occupancy	U_{iso} x 100/Å^2
Mg/4a	0	0	0	1	0.60(9)
O/4b	0.5(0)	0.5(0)	0.5(0)	1	2.08(17)

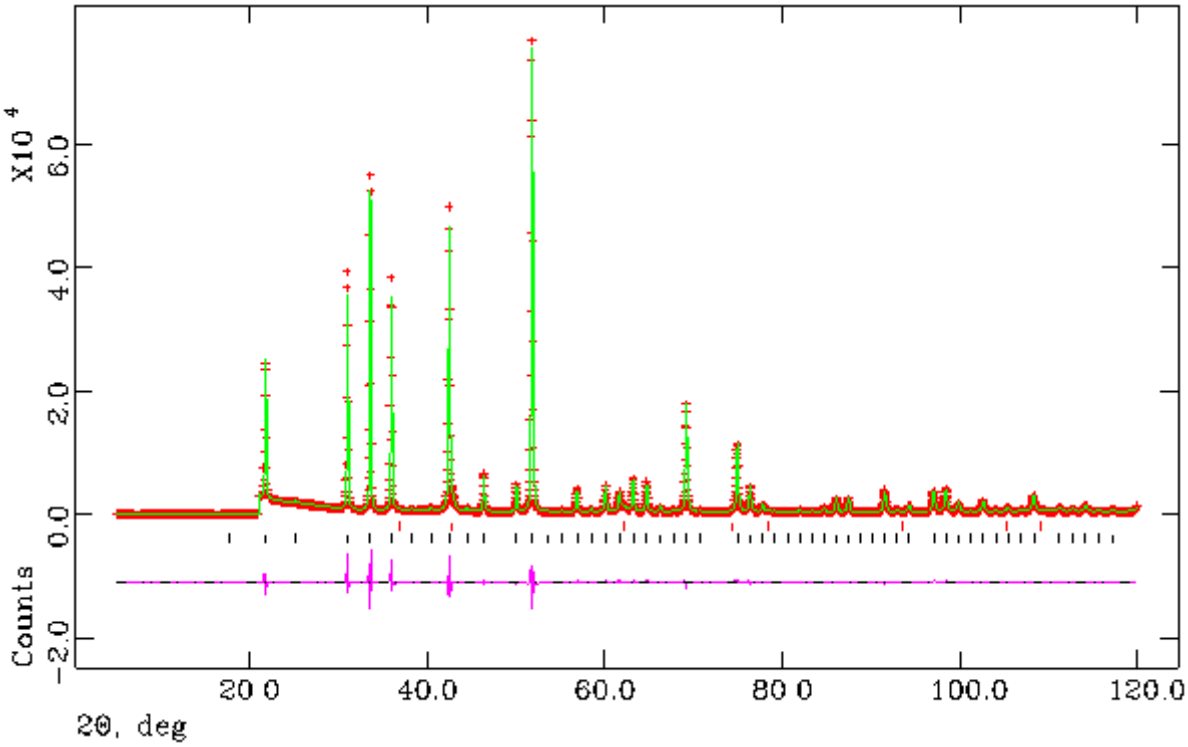

Fig.5.6 Rietveld refinement for Mg_3N_2 powder synthesised at 750° C. Observed (crosses), calculated (solid line) and difference curves (bottom line) are shown for comparison. Vertical bars (I) correspond to Bragg positions of Mg_3N_2 (black) and MgO (red) phases respectively from bottom to top.

Table.5.10 *Selected Rietveld refinement data from PXD data of sample (3) synthesised at 750°C.*

Sample (3) - 750°C			
Phases		Mg_3N_2	MgO
Phase Fraction/wt.%		94.05(1)	5.95(8)
Crystal System		Cubic	Cubic
Space Group		*Ia-3(206)*	*Fm-3m(225)*
Unit cell parameters/Å	a	9.96839(4)	4.2262(4)
	b	9.96839(4)	4.2262(4)
	c	9.96839(4)	4.2262(4)
Volume/$Å^3$		990.54(1)	75.48(2)
Z		48	48
Formula Weight/g		1658.952	162.683
Density ρ_x/gcm^{-3}		2.781	3.579
No of observations		2961	
No of variables		75	
R_{wp}		0.0709	
R_p		0.054	
χ^2		7.997	

Table.5.11 *Atomic parameters of Mg_3N_2 (sample 3).*

Atom/Site	x	y	z	Occupancy	U_{iso} x 100/$Å^2$
Mg/48e	0.38935(7)	0.15251(6)	0.38231(9)	0.994(1)	0.42(1)
N1/8b	0.25(0)	0.25(0)	0.25(0)	0.166(8)	1.81(11)
N2/24d	-0.03025(18)	0	0.25(0)	0.500(3)	1.63(5)

Table.5.12 *Atomic parameters of MgO (sample 3).*

Atom/Site	x	y	z	Occupancy	U_{iso} x 100/Å^2
Mg/4a	0	0	0	1	2.40(1)
O/4b	0.5(0)	0.5(0)	0.5(0)	1	0.96(2)

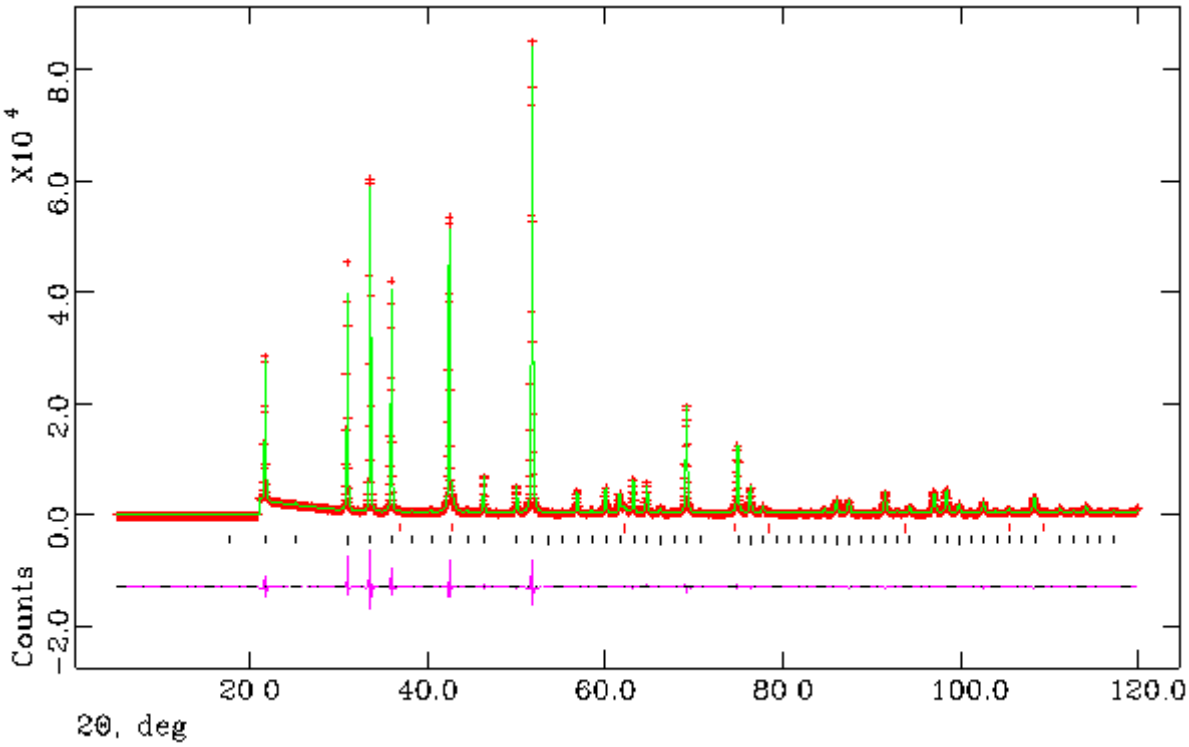

Fig.5.7 Rietveld refinement for Mg_3N_2 powder synthesised at 800° C. Observed (crosses), calculated (solid line) and difference curves (bottom line) are shown for comparison. Vertical bars (I) correspond to Bragg positions of Mg_3N_2 (black) and MgO (red) phases respectively from bottom to top.

Table.5.13 *Selected Rietveld refinement data from PXD data of sample (4) synthesised at 800°C.*

Sample (4) - 800°C			
Phases		Mg_3N_2	MgO
Phase Fraction/wt.%		94.44(1)	5.56(9)
Crystal System		Cubic	Cubic
Space Group		*Ia-3(206)*	*Fm-3m(225)*
Unit cell parameters/Å	a	9.96773(4)	4.2210(5)
	b	9.96773(4)	4.2210(5)
	c	9.96773(4)	4.2210(5)
Volume/$Å^3$		990.34(1)	75.20(2)
Z		48	48
Formula Weight/g		1659.801	164.966
Density ρ_x/gcm^{-3}		2.783	3.642
No of observations		2961	
No of variables		64	
R_{wp}		0.0689	
R_p		0.0518	
χ^2		7.417	

Table.5.14 *Atomic parameters of Mg_3N_2 (sample 4).*

Atom/Site	**x**	**y**	**z**	**Occupancy**	**U_{iso} x 100/$Å^2$**
Mg/48e	0.38939(7)	0.15248(6)	0.38223(9)	0.996(1)	0.50(1)
N1/8b	0.25(0)	0.25(0)	0.25(0)	0.166(9)	1.89(12)
N2/24d	-0.03031(19)	0	0.25(0)	0.500(4)	1.61(6)

Table.5.15 *Atomic parameters of MgO (sample 4).*

Atom/Site	x	y	z	Occupancy	U_{iso} x 100/Å^2
Mg/4a	0	0	0	1	1.85(15)
O/4b	0.5(0)	0.5(0)	0.5(0)	1	1.36(27)

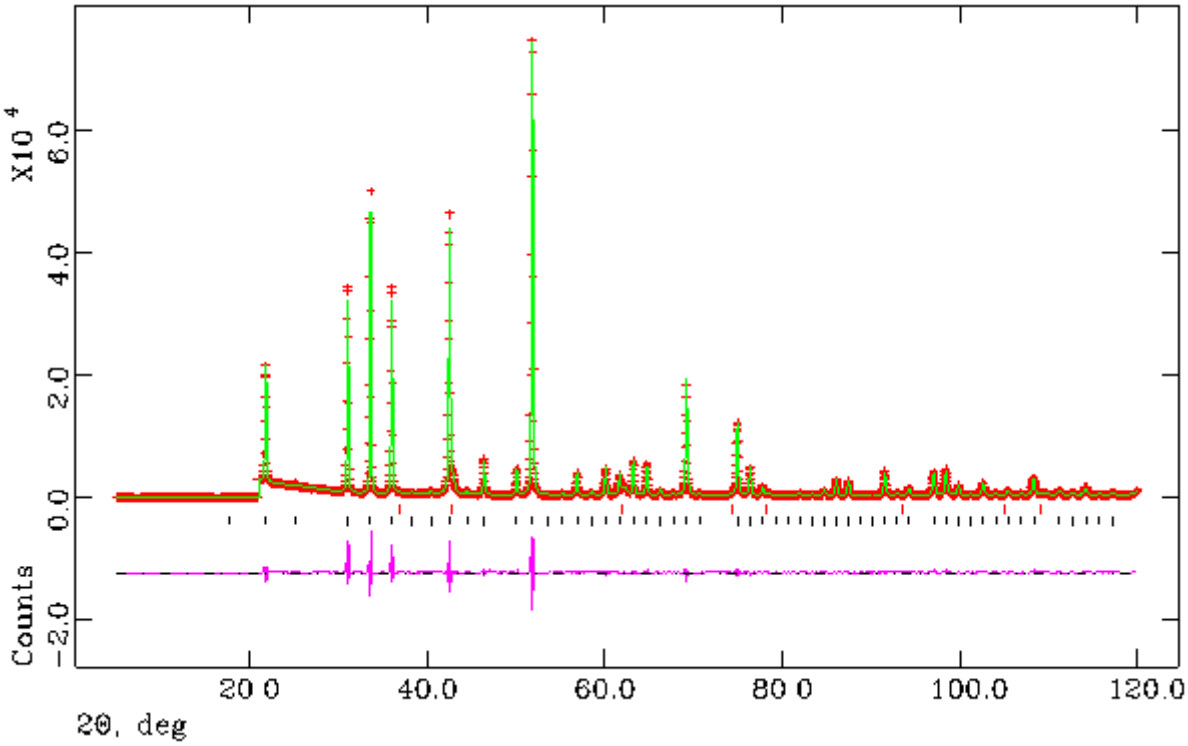

Fig.5.8 Rietveld refinement for Mg_3N_2 powder synthesised at 850° C. Observed (crosses), calculated (solid line) and difference curves (bottom line) are shown for comparison. Vertical bars (I) correspond to Bragg positions of Mg_3N_2 (black) and MgO (red) phases respectively from bottom to top.

Table.5.16 *Selected Rietveld refinement data from PXD data of sample (5) synthesised at 850°C.*

Sample (5) - 850°C			
Phases		Mg_3N_2	MgO
Phase Fraction/wt.%		93.34(1)	6.6(10)
Crystal System		Cubic	Cubic
Space Group		*Ia-3(206)*	*Fm-3m(225)*
Unit cell parameters/Å	a	9.96766(5)	4.2292(4)
	b	9.96766(5)	4.2292(4)
	c	9.96766(5)	4.2292(4)
Volume/$Å^3$		990.32(1)	75.64(2)
Z		48	48
Formula Weight/g		1642.026	175.833
Density ρ_x/gcm^{-3}		2.753	3.860
No of observations		2961	
No of variables		70	
R_{wp}		0.0837	
R_p		0.0647	
χ^2		11.38	

Table.5.17 *Atomic parameters of Mg_3N_2 (sample 5).*

Atom/Site	x	y	z	Occupancy	U_{iso} x 100/$Å^2$
Mg/48e	0.38941(9)	0.15240(8)	0.38205(11)	0.989(1)	1.60(1)
N1/8b	0.25(0)	0.25(0)	0.25(0)	0.166(10)	3.40(15)
N2/24d	-0.03016(22)	0	0.25(0)	0.500(4)	2.08(6)

Table.5.18 *Atomic parameters of MgO (sample 5).*

Atom/Site	x	y	z	Occupancy	U_{iso} x 100/Å^2
Mg/4a	0	0	0	1	2.48(13)
O/4b	0.5(0)	0.5(0)	0.5(0)	1	4.59(28)

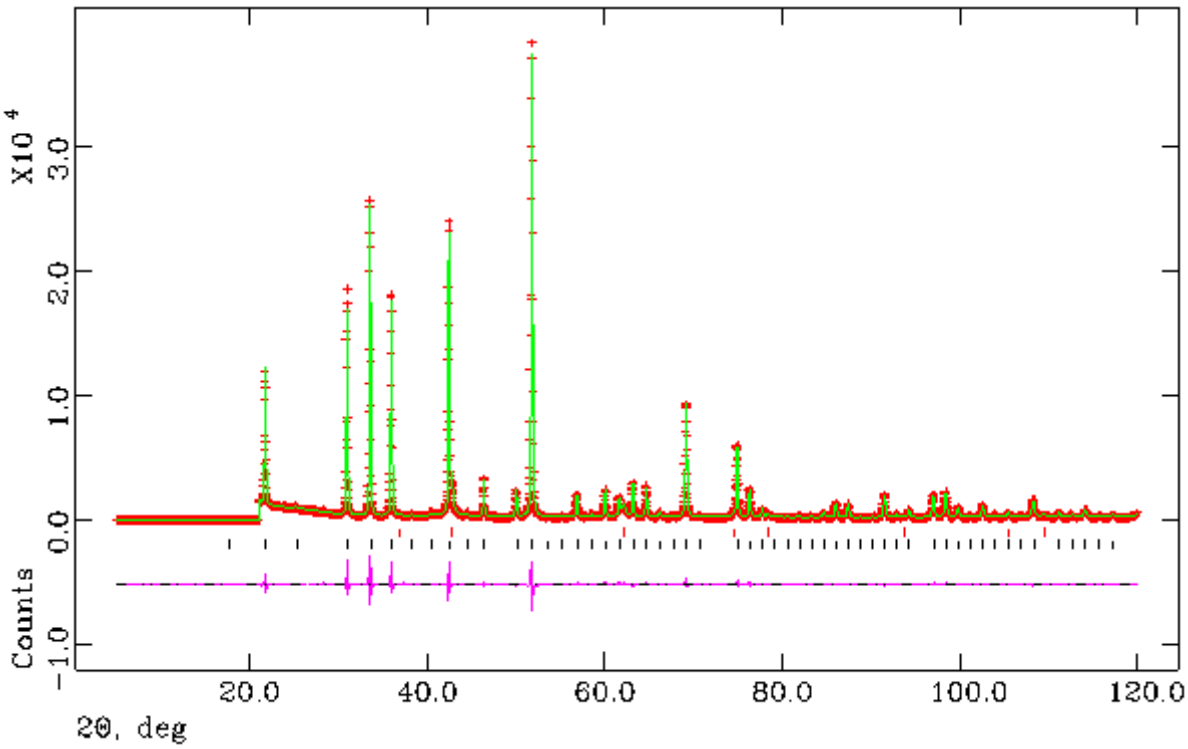

Fig.5.9 Rietveld refinement for Mg_3N_2 powder synthesised at 900° C. Observed (crosses), calculated (solid line) and difference curves (bottom line) are shown for comparison. Vertical bars (I) correspond to Bragg positions of Mg_3N_2 (black) and MgO (red) phases respectively from bottom to top.

Table.5.19 *Selected Rietveld refinement data from PXD data of sample (6) synthesised at 900°C.*

Sample (6) - 900°C			
Phases		Mg_3N_2	MgO
Phase Fraction/wt.%		92.25(2)	7.75(13)
Crystal System		Cubic	Cubic
Space Group		*Ia-3(206)*	*Fm-3m(225)*
Unit cell parameters/Å	a	9.96785(6)	4.2192(3)
	b	9.96785(6)	4.2192(3)
	c	9.96785(6)	4.2192(3)
Volume/$Å^3$		990.38(1)	75.11(2)
Z		48	48
Formula Weight/g		1660.946	173.104
Density ρ_x/gcm^{-3}		2.785	3.827
No of observations		5923	
No of variables		64	
R_{wp}		0.0696	
R_p		0.0555	
χ^2		3.683	

Table.5.20 *Atomic parameters of Mg_3N_2 (sample 6).*

Atom/Site	**x**	**y**	**z**	**Occupancy**	**U_{iso} x 100/$Å^2$**
Mg/48e	0.38933(7)	0.15241(6)	0.38221(8)	0.996(2)	0.64(1)
N1/8b	0.25(0)	0.25(0)	0.25(0)	0.166(9)	1.63(12)
N2/24d	-0.03060(16)	0	0.25(0)	0.500(4)	1.78(6)

Table.5.21 *Atomic parameters of MgO (sample 6).*

Atom/Site	x	y	z	Occupancy	U_{iso} x 100/Å^2
Mg/4a	0	0	0	1	0.50(10)
O/4b	0.5(0)	0.5(0)	0.5(0)	1	2.48(21)

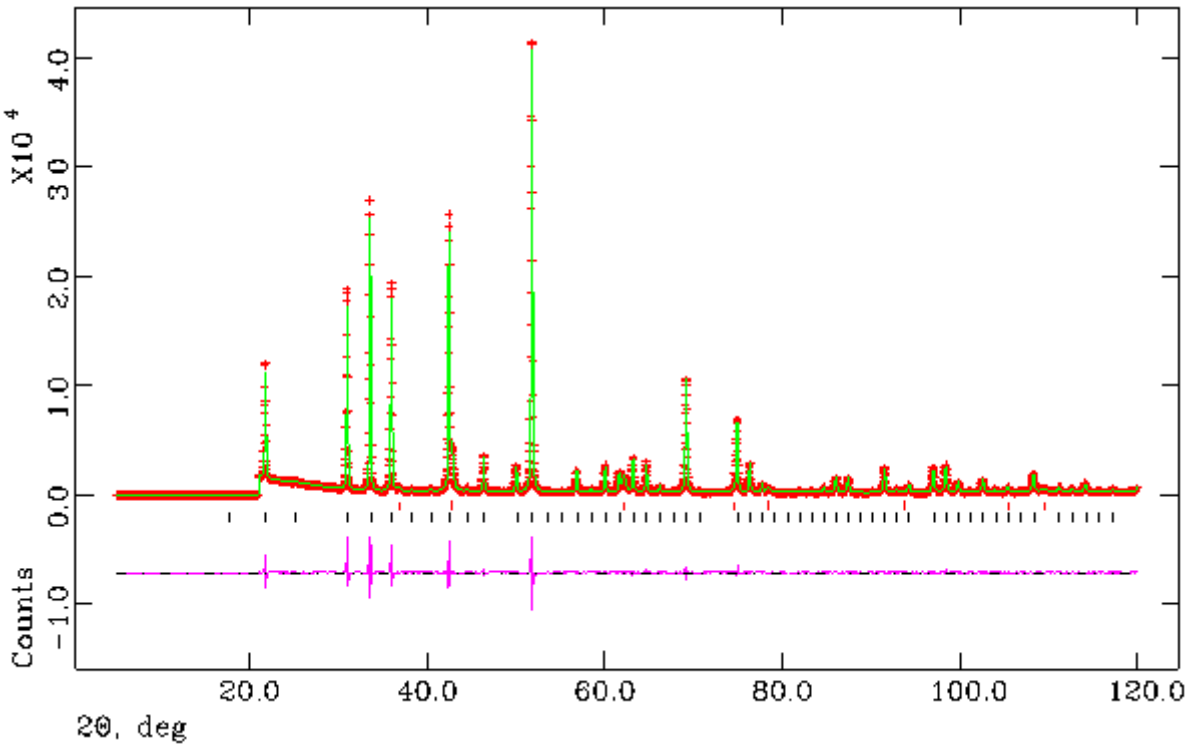

Fig.5.10 Rietveld refinement for Mg_3N_2 powder synthesised at 950°C. Observed (crosses), calculated (solid line) and difference curves (bottom line) are shown for comparison. Vertical bars (I) correspond to Bragg positions of Mg_3N_2 (black) and MgO (red) phases respectively from bottom to top.

Table.5.22 *Selected Rietveld refinement data from PXD data of sample (7) synthesised at 950°C.*

Sample (7) - 950°C			
Phases		Mg_3N_2	MgO
Phase Fraction/wt.%		91.14(2)	8.86(10)
Crystal System		Cubic	Cubic
Space Group		*Ia-3(206)*	*Fm-3m(225)*
Unit cell parameters/Å	a	9.96662(5)	4.2172(2)
	b	9.96662(5)	4.2172(2)
	c	9.96662(5)	4.2172(2)
Volume/$Å^3$		990.02(1)	75.00(1)
Z		48	48
Formula Weight/g		1683.178	165.455
Density ρ_x/gcm^{-3}		2.823	3.663
No of observations		5923	
No of variables		64	
R_{wp}		0.0794	
R_p		0.0625	
χ^2		5.14	

Table.5.23 *Atomic parameters of Mg_3N_2 (sample 7).*

Atom/Site	x	y	z	Occupancy	U_{iso} x 100/$Å^2$
Mg/48e	0.38932(7)	0.15253(6)	0.38217(8)	0.995(2)	0.71(1)
N1/8b	0.25(0)	0.25(0)	0.25(0)	0.166(10)	1.82(12)
N2/24d	-0.03044(17)	0	0.25(0)	0.500(4)	1.77(6)

Table.5.24 *Atomic parameters of MgO (sample 7).*

Atom/Site	x	y	z	Occupancy	U_{iso} x 100/Å^2
Mg/4a	0	0	0	1	0.96(8)
O/4b	0.5(0)	0.5(0)	0.5(0)	1	1.25(15)

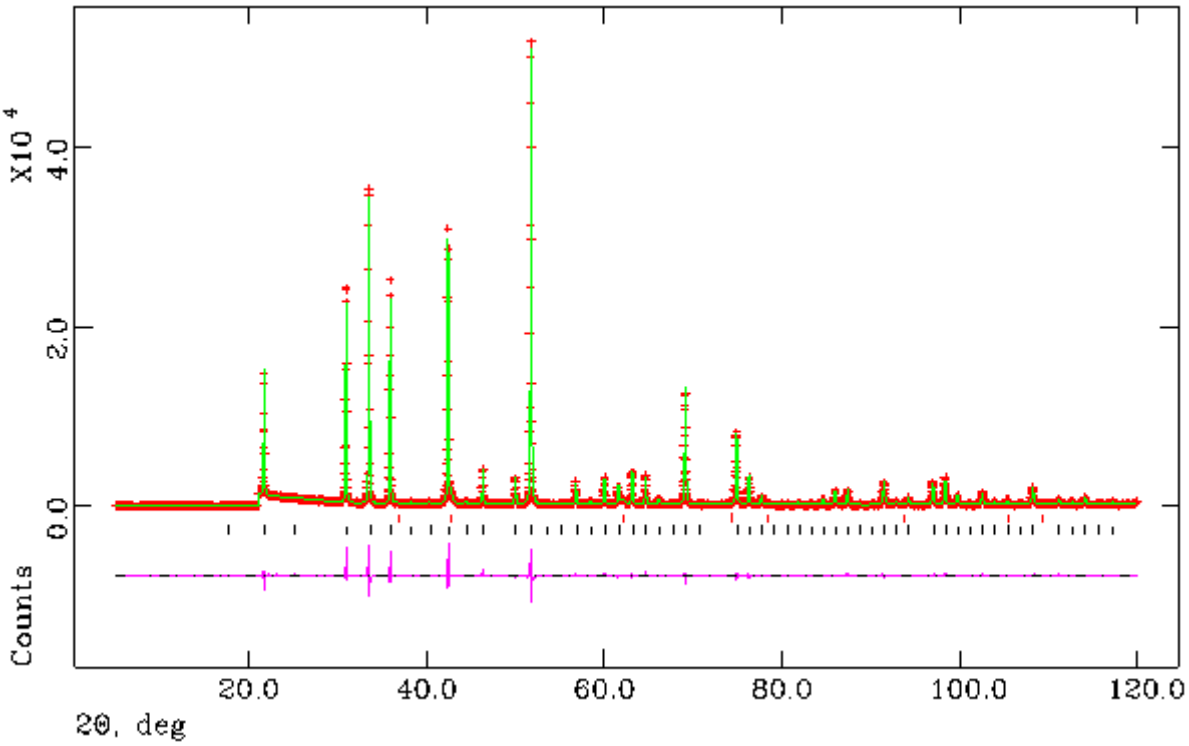

Fig.5.11 Rietveld refinement for Mg_3N_2 powder synthesised at 1000°C. Observed (crosses), calculated (solid line) and difference curves (bottom line) are shown for comparison. Vertical bars (I) correspond to Bragg positions of Mg_3N_2 (black) and MgO (red) phases respectively from bottom to top.

Table.5.25 *Selected Rietveld refinement data from PXD data of sample (8) synthesised at 1000°C.*

Sample (8) - 1000°C			
Phases		Mg_3N_2	MgO
Phase Fraction/wt.%		95.99(5)	4.01(5)
Crystal System		Cubic	Cubic
Space Group		*Ia-3(206)*	*Fm-3m(225)*
Unit cell parameters/Å	a	9.96797(2)	4.2214(2)
	b	9.96797(2)	4.2214(2)
	c	9.96797(2)	4.2214(2)
Volume/$Å^3$		990.42(1)	75.22(1)
Z		48	48
Formula Weight/g		1650.699	163.518
Density ρ_x/gcm^{-3}		2.768	3.609
No of observations		5923	
No of variables		61	
R_{wp}		0.0829	
R_p		0.0657	
χ^2		5.113	

Table.5.26 *Atomic parameters of Mg_3N_2 (sample 8).*

Atom/Site	**x**	**y**	z	**Occupancy**	**U_{iso} x 100/$Å^2$**
Mg/48e	0.38950(6)	0.15270(5)	0.38199(7)	0.994(1)	1.38(1)
N1/8b	0.25(0)	0.25(0)	0.25(0)	0.166(7)	3.48(9)
N2/24d	-0.02967(14)	0	0.25(0)	0.500(3)	1.88(4)

Table.5.27 *Atomic parameters of MgO (sample 8).*

Atom/Site	x	y	z	Occupancy	U_{iso} x 100/Å^2
Mg/4a	0	0	0	1	2.42(12)
O/4b	0.5(0)	0.5(0)	0.5(0)	1	1.43(21)

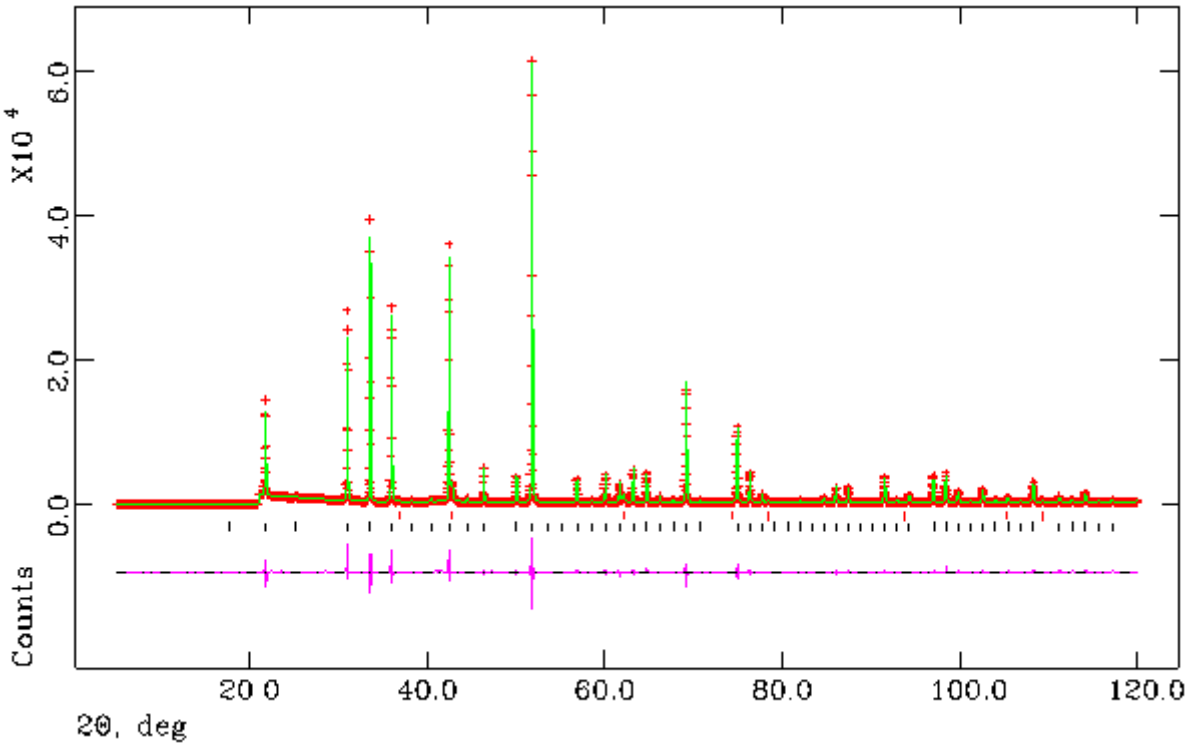

Fig.5.12 Rietveld refinement for Mg_3N_2 powder synthesised at 1150°C. Observed (crosses), calculated (solid line) and difference curves (bottom line) are shown for comparison. Vertical bars (I) correspond to Bragg positions of Mg_3N_2 (black) and MgO (red) phases respectively from bottom to top.

Table.5.28 *Selected Rietveld refinement data from PXD data of sample (9) synthesised at 1150°C.*

Sample (9) - 1150 °C			
Phases		Mg_3N_2	MgO
Phase Fraction/wt.%		94.26(1)	5.74(7)
Crystal System		Cubic	Cubic
Space Group		*Ia-3(206)*	*Fm-3m(225)*
Unit cell parameters/Å	a	9.96915(2)	4.2224(1)
	b	9.96915(2)	4.2224(1)
	c	9.96915(2)	4.2224(1)
Volume/$Å^3$		990.774(6)	75.284(9)
Z		48	48
Formula Weight/g		1660.934	165.135
Density ρ_x/gcm^{-3}		2.784	3.642
No of observations		5924	
No of variables		73	
R_{wp}		0.1063	
R_p		0.0813	
χ^2		8.09	

Table.5.29 *Atomic parameters of Mg_3N_2 (sample 9).*

Atom/Site	**x**	**y**	**z**	**Occupancy**	**U_{iso} x 100/$Å^2$**
Mg/48e	0.38940(7)	0.15267(6)	0.38205(9)	0.996(1)	0.57(1)
N1/8b	0.25(0)	0.25(0)	0.25(0)	0.166(8)	1.79(10)
N2/24d	-0.03042(18)	0	0.25(0)	0.500(3)	1.03(5)

Table.5.30 *Atomic parameters of MgO (sample 9).*

Atom/Site	x	y	z	Occupancy	U_{iso} x 100/Å^2
Mg/4a	0	0	0	1	2.43(11)
O/4b	0.5(0)	0.5(0)	0.5(0)	1	0.68(11)

Mg_3N_2 was successfully synthesised by the reaction of Mg powder placed in alumina crucible under flowing N_2 gas at different temperatures. The yield of product could reach 96 %. These compounds have the antibixbyte structure. The space group is $Ia\bar{3}\ (No.206)$. In this cubic structure, the metal atoms are in general positions, 48e of $Ia\bar{3}$ (x, y, z) and there are two kinds of N atom. N(1) is in position 8b $(\frac{1}{4}, \frac{1}{4}, \frac{1}{4})$ and N(2) is in position 24d $(x, 0, \frac{1}{4})$.

5.2.2 Morphological results – SEM analysis

With the purpose of investigating the effect of the nitridation reaction temperature on particle size and morphology of Mg_3N_2, samples were examined with SEM and a wide range of morphology is observed from the different synthetic temperatures.

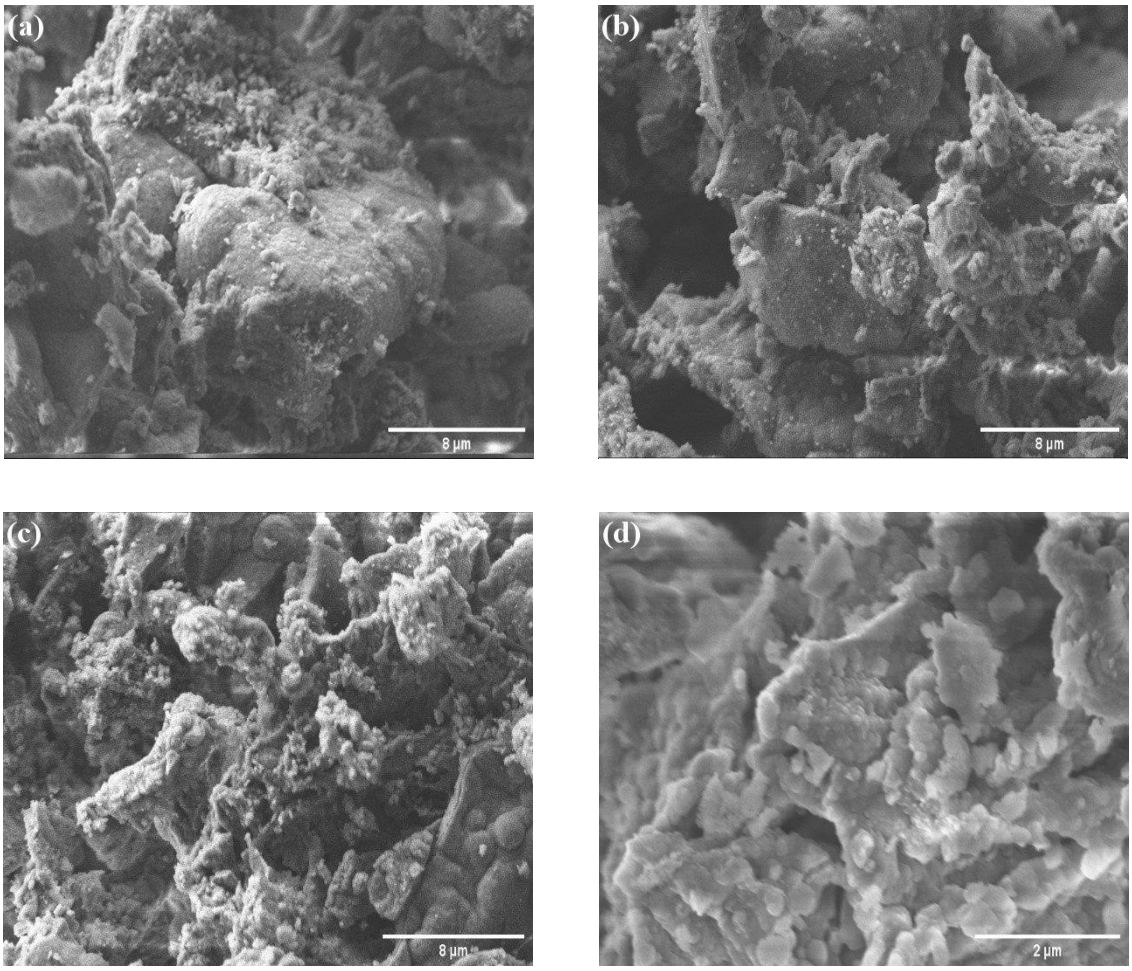

EDX (%.Wt) : Magnesium (69), Nitrogen (31)
EDX (%.Wt) : Magnesium (76.7), Nitrogen (23.3)
EDX (%.Wt) : Magnesium (87.9), Nitrogen (12.1)

Fig.5.13 Scanning electron micrographs of Mg_3N_2 powder synthesised by the nitridation reaction of Mg with N_2 gas at 650°C.

The synthesised Mg_3N_2 has not uniform size. It is due to agglomeration of primary single crystal as seen in Fig.5.13 The particles have an average value ranging from 2-20 nm; some have dark spots on them suggesting they may be porous. For areas

containing both large and small particles, when a clump of the smaller, more regular particles was found.

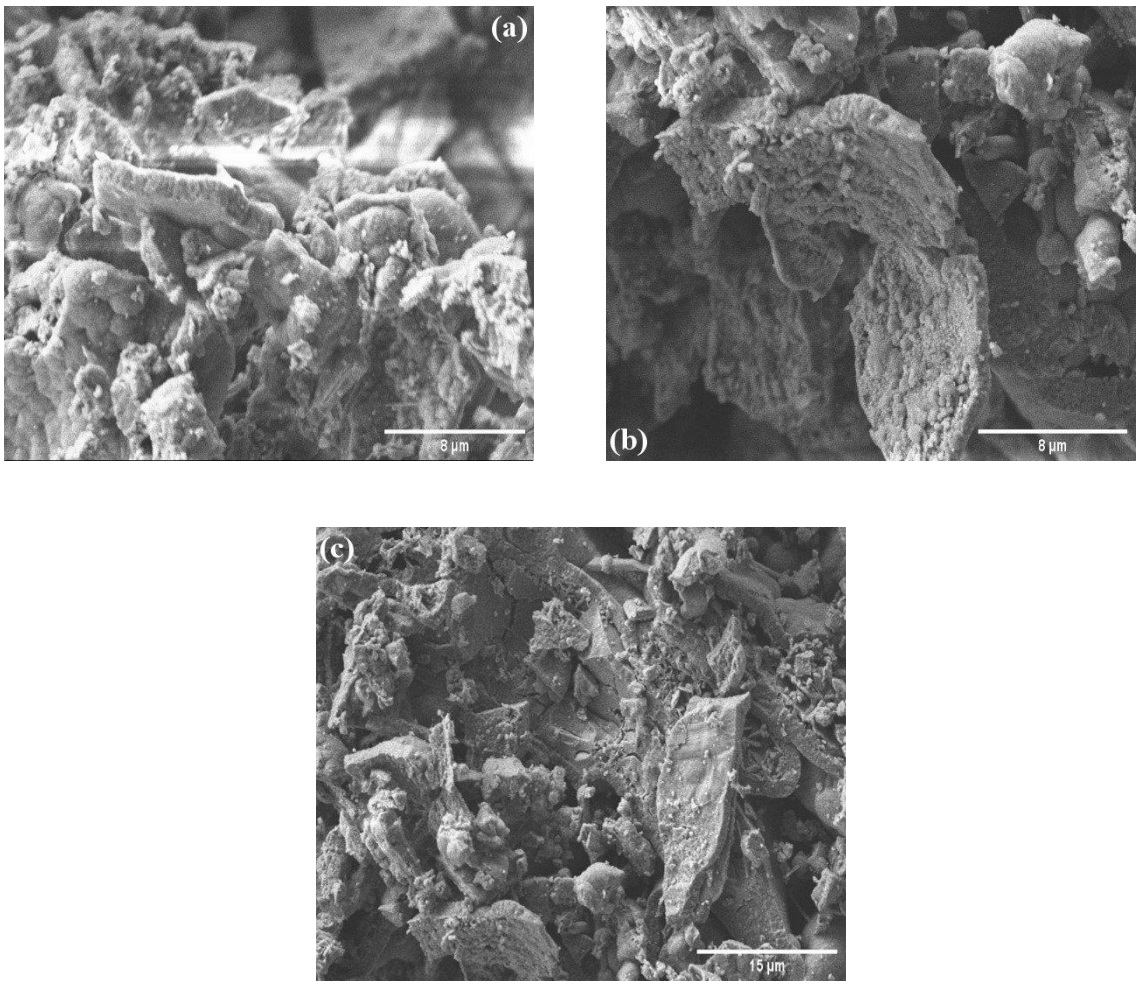

EDX (%.Wt) : Magnesium (73.5), Nitrogen (26.5)
EDX (%.Wt) : Magnesium (87.8), Nitrogen (12.2)
EDX (%.Wt) : Magnesium (67.6), Nitrogen (32.4)

Fig.5.14 Scanning electron micrographs of Mg_3N_2 powder synthesised by the nitridation reaction of Mg with N_2 gas at 700°C.

SEM images (Fig.5.14) show a brick-like chunks morphology. Uneven crystallites clumping to form 9-80 nm average size particles. It is possible that the time used for the reaction was short to allow the temperature gradient inside the pot to settle to its equilibrium state, although this seems unlikely for a furnace which takes a few hours to reach the target temperature.

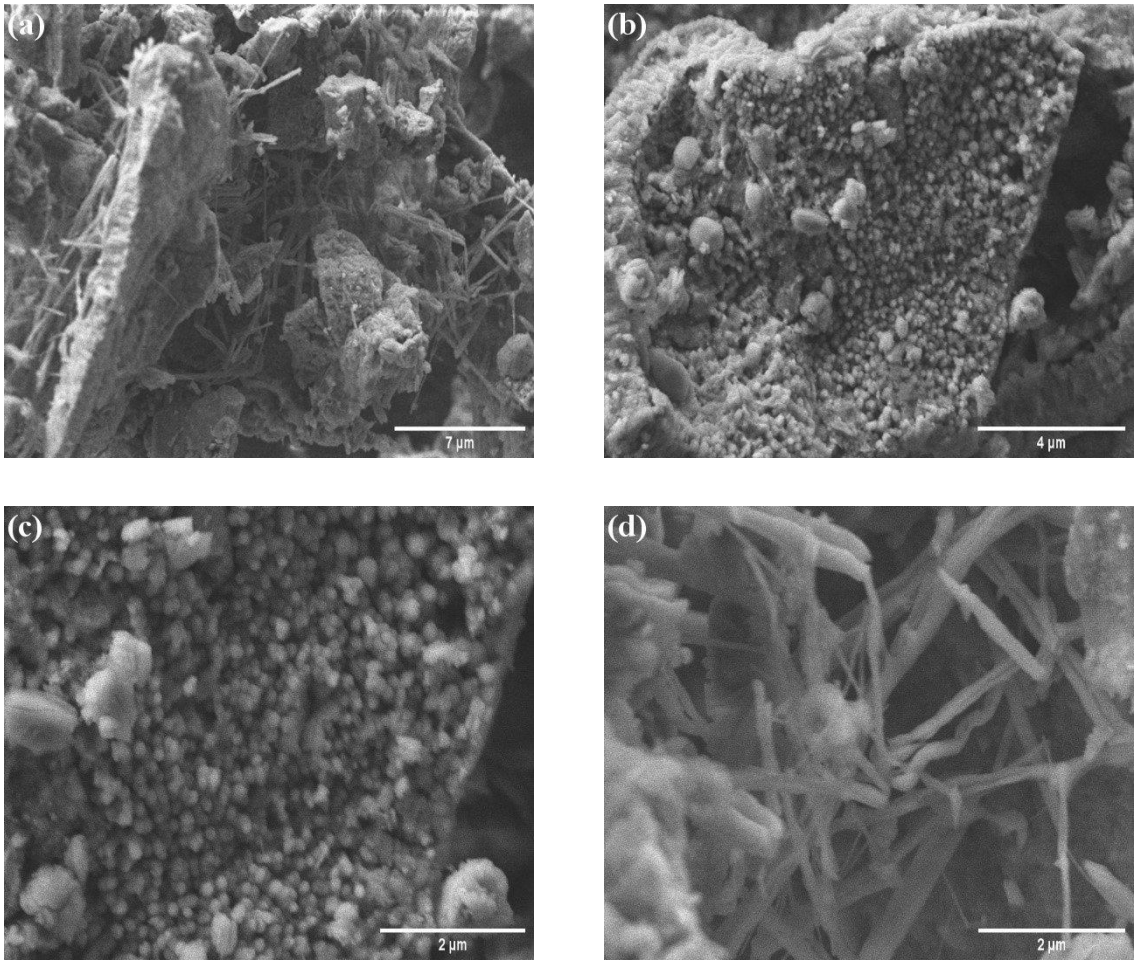

EDX (%.Wt) : Magnesium (79.6), Nitrogen (20.4)

Fig.5.15 Scanning electron micrographs of Mg_3N_2 powder synthesised by the nitridation reaction of Mg with N_2 gas at 750°C.

With an increase in reaction temperature to 750°C, a greater proportion of nanowires or nanotubes appear to be merging into one and other, they tend to be highly branched and irregular in diameter along their length (Fig.5.15-a). The surface of the largest nanowire (Fig.5.15-d) can be identified as rough and flaky and appear to have a prismatic form. The diameters were found in 250-350 nm, with lengths ranging from 2-10 µm. The sample was composed with the tendency to align in stacked arrays, evident in images (b) and (c).

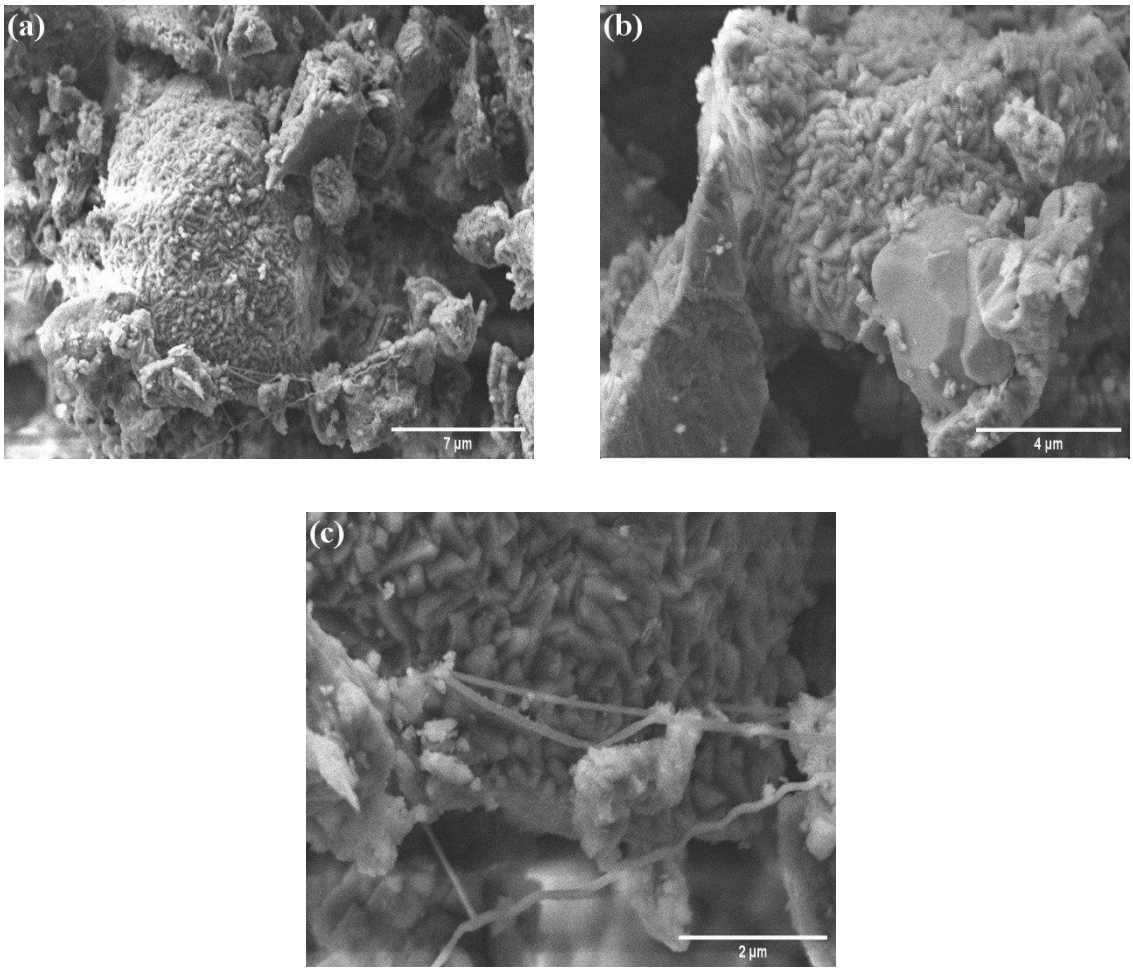

EDX (%.Wt) : Magnesium (74.4), Nitrogen (26.0)

EDX (%.Wt) : Magnesium (73.9), Nitrogen (26.1)

EDX (%.Wt) : Magnesium (75.3), Nitrogen (24.7)

Fig.5.16 Scanning electron micrographs of Mg_3N_2 powder synthesised by the nitridation reaction of Mg with N_2 gas at 800°C.

Figure 5.16 found the resulting Mg_3N_2 to be inhomogeneous. The difference in particle size is distinctly observed. Smaller and a more uniform distribution of particle size of about 3-27 nm were agglomerated over large particles. They allowed very few dangly and kinked nanowires to be synthesised, they are generally narrow and long.

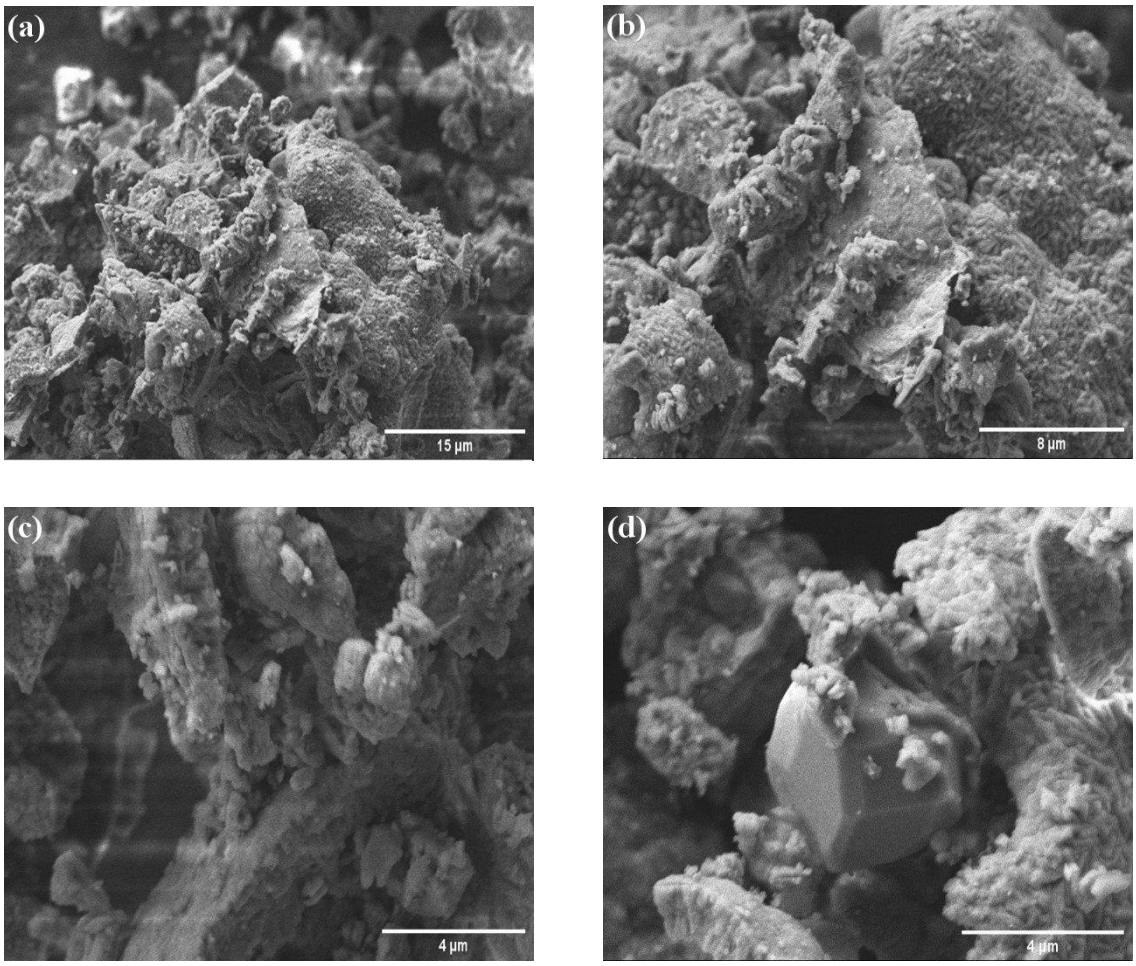

EDX (%.Wt) : Magnesium (65.8), Nitrogen (34.2)
EDX (%.Wt) : Magnesium (82.3), Nitrogen (17.7)
EDX (%.Wt) : Magnesium (71.6), Nitrogen (28.4)

Fig.5.17 Scanning electron micrographs of Mg_3N_2 powder synthesised by the nitridation reaction of Mg with N_2 gas at 850°C.

The synthesised Mg_3N_2 appears as an inhomogeneous mixture of larger pieces (with a metallic appearance (Fig.5.17-d), which is possibly caused by the melting of the product) and fine powders. However, no nanowires were observed.

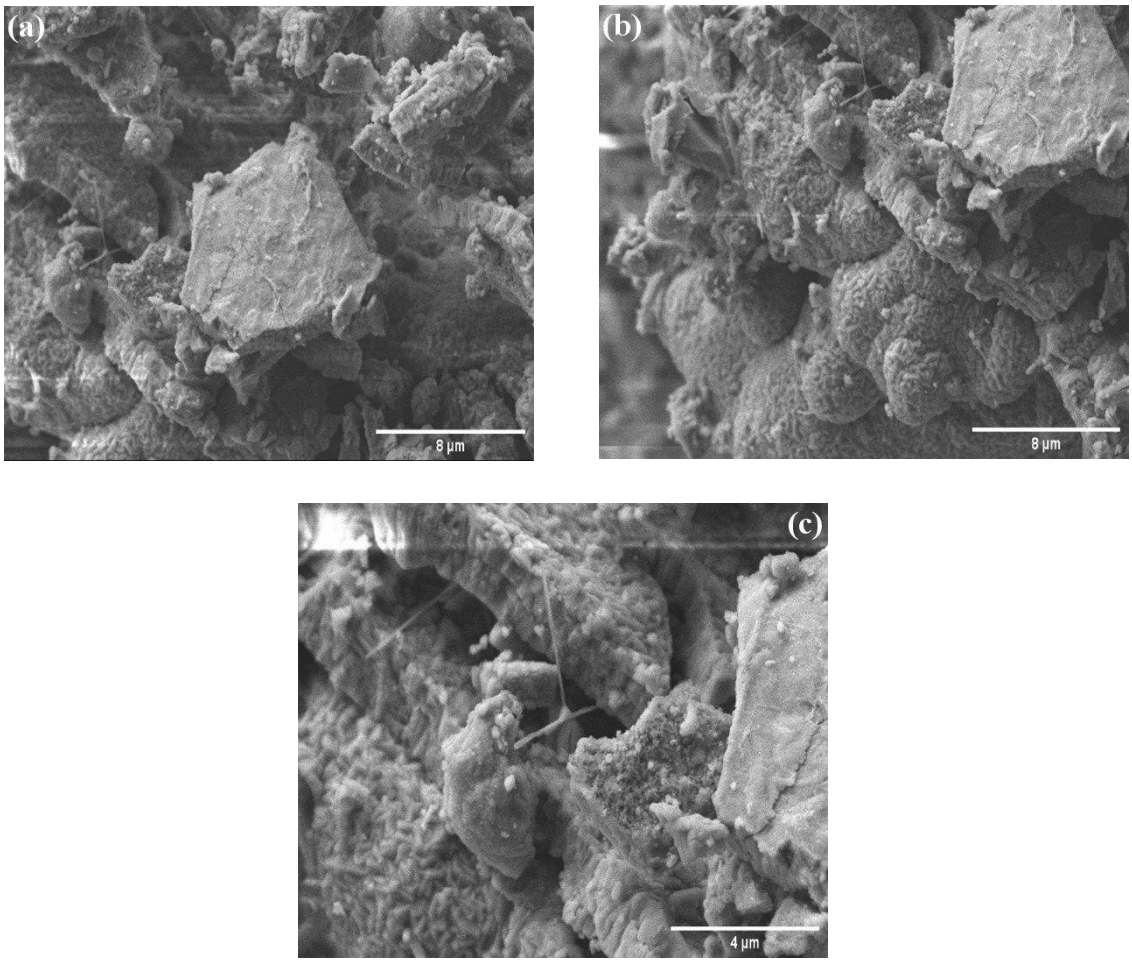

EDX (%.Wt) : Magnesium (82.7), Nitrogen (17.3)
EDX (%.Wt) : Magnesium (80.3), Nitrogen (19.7)
EDX (%.Wt) : Magnesium (80.6), Nitrogen (19.4)

Fig.5.18 Scanning electron micrographs of Mg_3N_2 powder synthesised by the nitridation reaction of Mg with N_2 gas at 900° C.

The SEM images of the ground sample (Fig.5.18) show clearly varying size of particles. Larger areas including clumping small particles of about 2-10 nm. Less big particles were found, with only few straight nanowires.

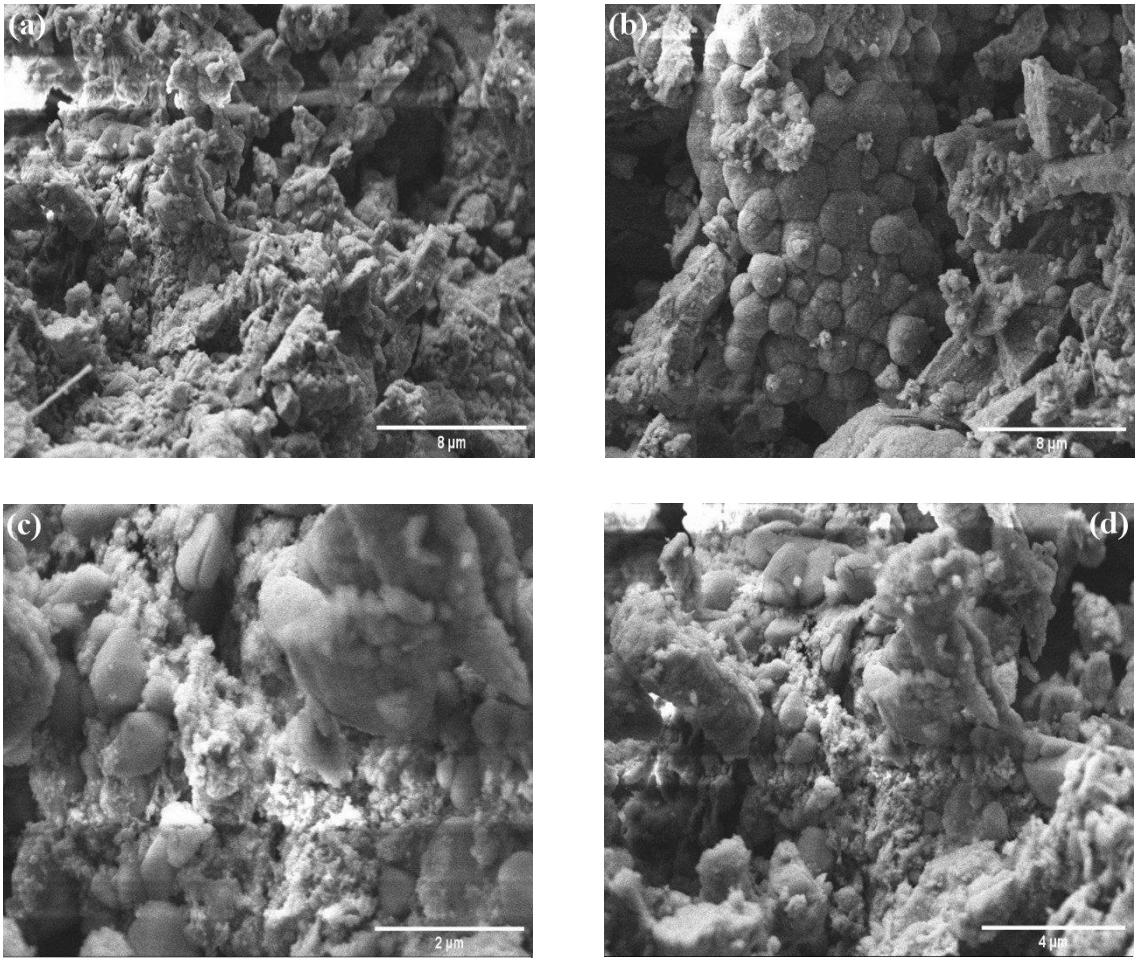

EDX (%.Wt) : Magnesium (79.6), Nitrogen (20.4)

EDX (%.Wt) : Magnesium (74.4), Nitrogen (26.0)

EDX (%.Wt) : Magnesium (73.9), Nitrogen (26.1)

Fig.5.19 Scanning electron micrographs of Mg_3N_2 powder synthesised by the nitridation reaction of Mg with N_2 gas at 950°C.

The morphology (Fig.5.19) appears to contain huge density of nanoparticles of distribution size of about 2-20 nm.

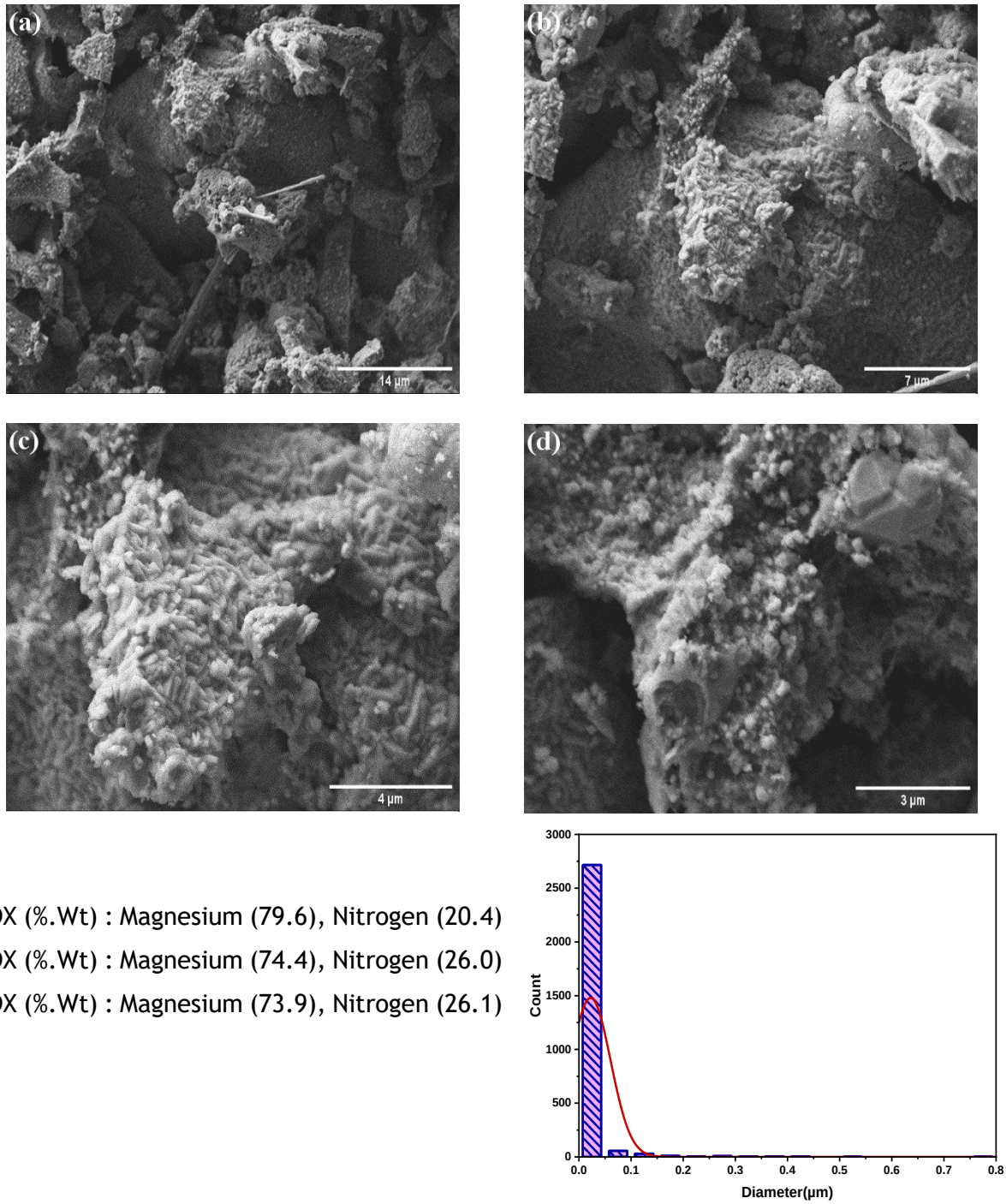

EDX (%.Wt) : Magnesium (79.6), Nitrogen (20.4)

EDX (%.Wt) : Magnesium (74.4), Nitrogen (26.0)

EDX (%.Wt) : Magnesium (73.9), Nitrogen (26.1)

Fig.5.20 Scanning electron micrographs of Mg_3N_2 powder synthesised by the nitridation reaction of Mg with N_2 gas at 1000°C.

The condensed pieces and finer particles of spheres were observed (Fig.5.20).

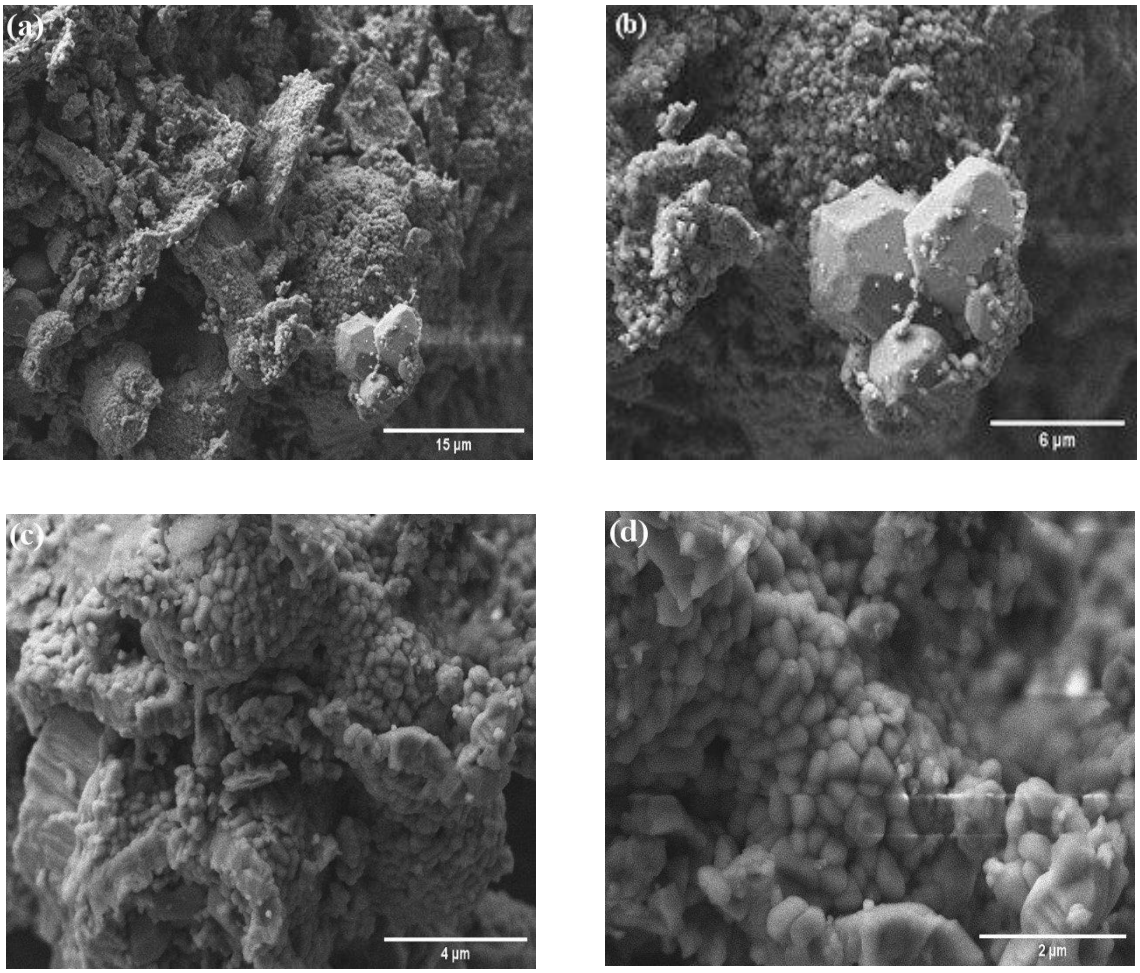

EDX (%.Wt) : Magnesium (79.6), Nitrogen (20.4)

EDX (%.Wt) : Magnesium (74.4), Nitrogen (26.0)

EDX (%.Wt) : Magnesium (73.9), Nitrogen (26.1)

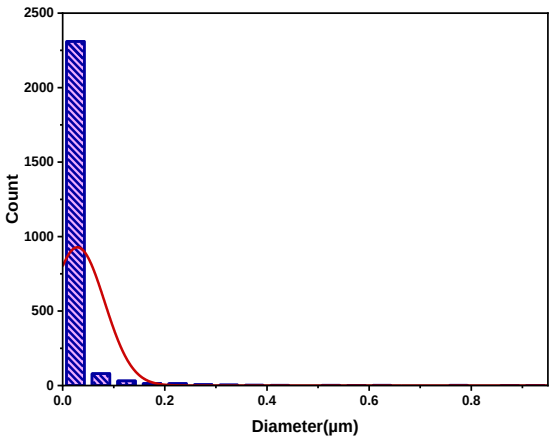

Fig.5.21 Scanning electron micrographs of Mg_3N_2 powder synthesised by the nitridation reaction of Mg with N_2 gas at 1150°C.

From the SEM results, the finest particles and the greatest homogeneity during the nitridation process. Further investigation is required looking specially at the other variables.

5.2.3 Band gap calculation

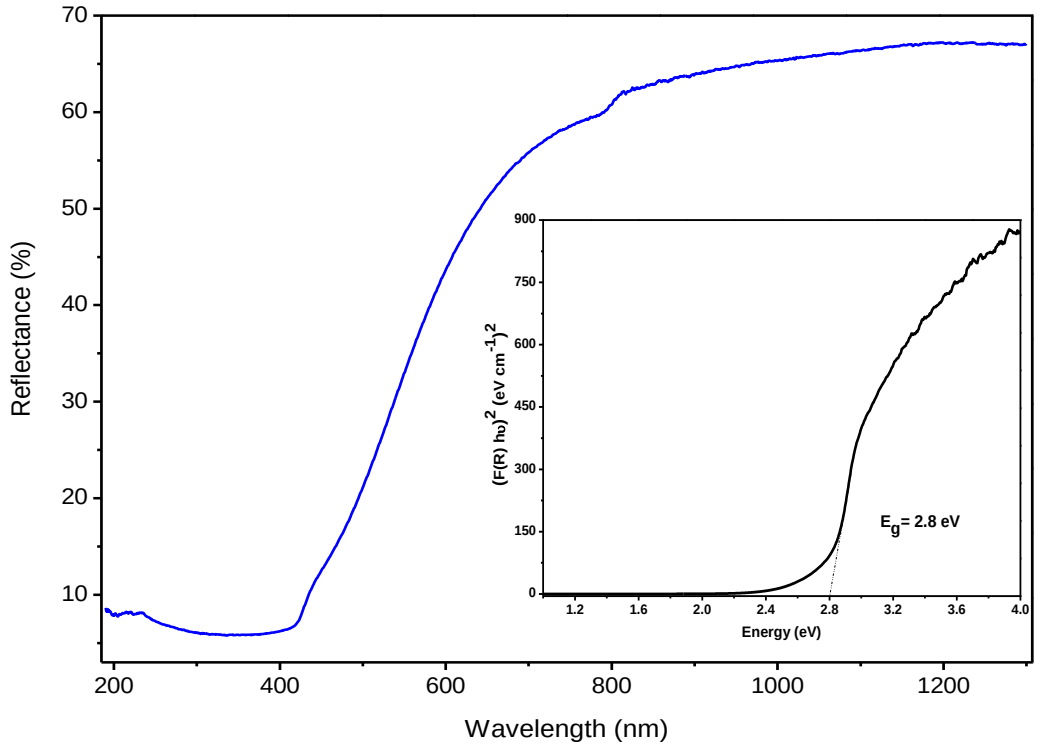

Fig.5.22 UV-Vis spectrum of Mg_3N_2 powder synthesised at 800°C with Tauc plot for band gap determination.

The optical band gap from reflectance measurements of Mg_3N_2 powder synthesised at 800°C was found to be a direct band gap semiconductor with E_g=2.8 eV (Fig.5.22), which is in good agreement with the published value [5, 6, 7].

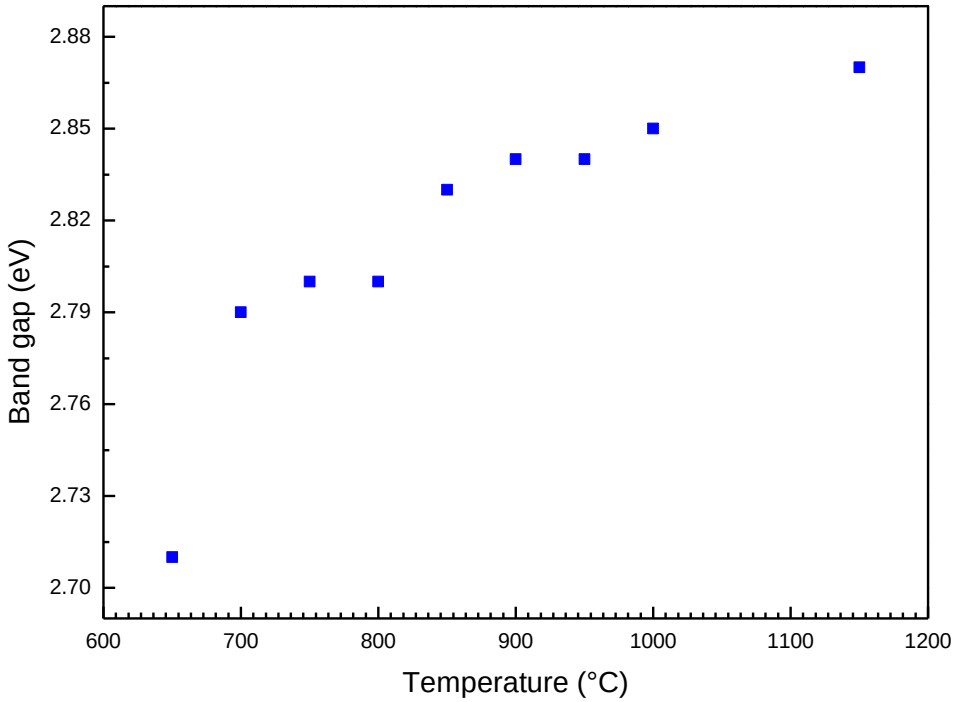

Fig.5.23 Band gap of Mg_3N_2 as a function of the nitridation temperature.

It may be noted that the band gap of synthesised Mg_3N_2 is almost equal for all samples. Slight variation, however, of the band gap with increasing nitridation temperature has been seen in Fig.5.23.

5.3 References

[1] S. Yougming, L. Yanbin, S. Jie, L. Yuzhang, P. Allen, C. Yi. Stabilized Li_3N for efficient battery cathode prelithiation. *Journal of Energy Storage Materials.*, 2017, **6**, 119-124.

[2] H. Brendecke, W. Bludau. *Journal of Applied Physics.*, 1979, **50**, 4743-4746.

[3] Brendecke, H. and W. Bludau. Optical absorption of lithium nitride. *Journal of Applied Physics.*, 1979, **50(7)**, 4743-4746.

[4] F. Zong, C. Meng, Z. Guo, F. Ji, H. Xiao, X. Zhang, J. Ma, H. Ma. *Journal of Alloys and Compounds.*, 2010, **508**, 172-176.

[5] R. C. Weast. in: CRC Handbook of Chemistry and Physics, 60th ed., CRC press, Boca Raton, FL, 1979, p. B-94.

[6] Y. Unekata, T. Uchino. Excitonic and defected-related photoluminescence in Mg_3N_2. *J. Phys. Chem. C.*, 2014, **116**, 11895-11901.

[7] D. W. Kim, T. H. Kim, H. W. Park, D. W. Park. *Appl. Surf. Sci.*, 2011, **45**, 257, 5375.

Chapter-6: STA and Post-STA Mg_3N_2 Results

6 Thermal gravimetric and differential thermal analysis

6.1 Introduction

Approximately 15 mg of Mg_3N_2 powder analysed via Simultaneous Thermogravimetric Analysis (STA). The sample was heated from room temperature up to 1000°C in a heating ramp of 5°C.min^{-1} in a furnace on an Argon glovebox. Combined flow was adjusted to 60 mL/min. Residual weight of the sample and heat flux with respect to time and temperature were recorded using NETZSCH Proteus software.

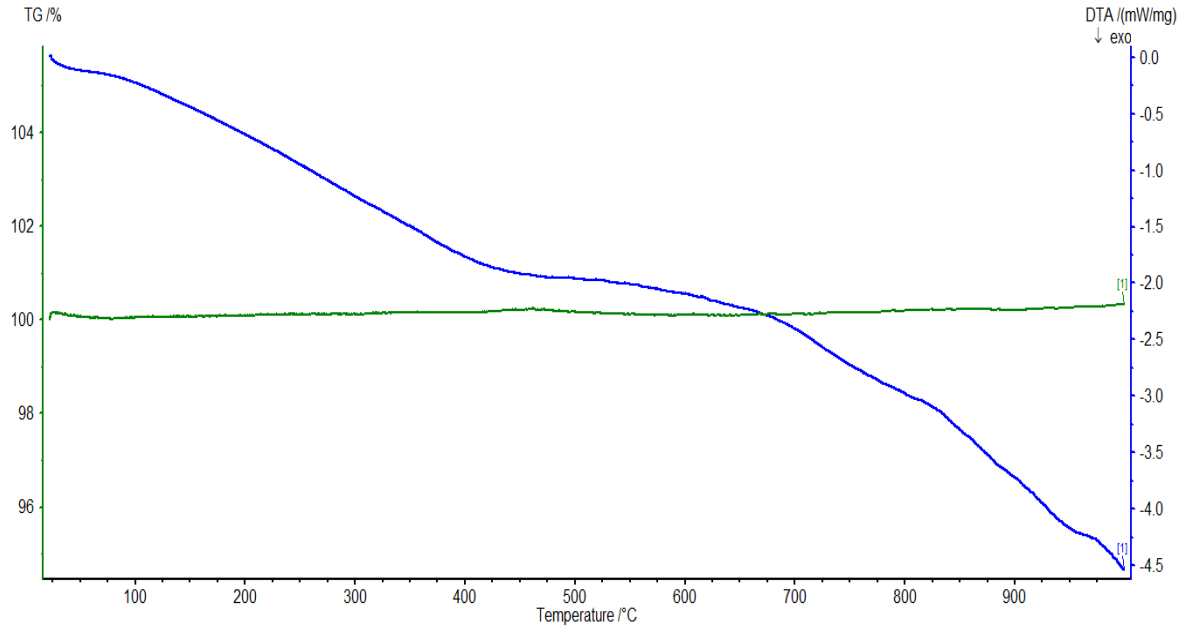

Fig.6.1 STA plot of Mg_3N_2 powder synthesised at 950°C. The sample was heated from room temperature to 1000°C under argon gas flow at 5°C.min^{-1}. TG curve (green) and DTA curve (blue).

As shown after refinement, the resulting Mg_3N_2 powder was consisted of Mg_3N_2 as a dominant phase with only small amounts of MgO. The oxygen may come from the contact with air when collected after its preparation. The formation of magnesium oxide explains the slight gain of weight observed in Fig.6.1. In order to obtain a better study, another STA analysis of the same powder was done in a heating ramp of 2°C.min^{-1}.

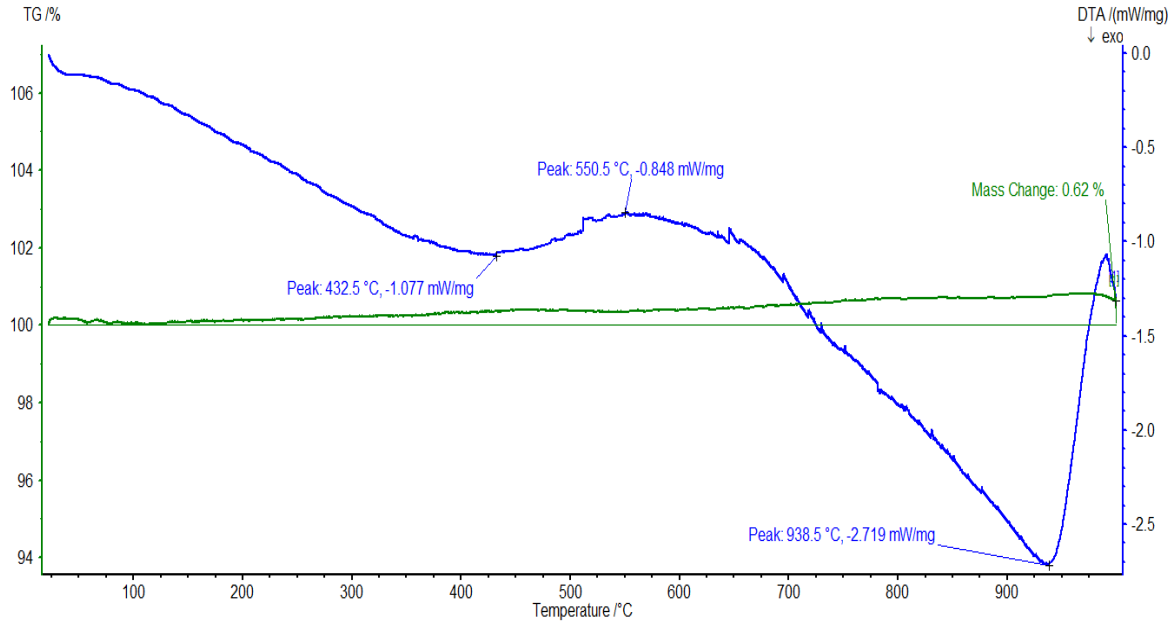

Fig.6.2 STA plot of Mg_3N_2 powder synthesised at 950°C. The sample was heated from room temperature to 1000°C under argon gas flow at 2°C.min^{-1}. TG curve (green) and DTA curve (blue).

DTA curve in Fig.6.2 shows an endothermic peak in the around of 550°C which is considerably large with decreasing heating rate to 2°C/min. The size distribution of crystallites likely occurs during large heating run. Large heat needs to melt. Mg_3N_2 has a decomposition temperature below 800°C [1]. When the temperature was further raised to 800°C and the atmosphere was changed into N_2/O_2 gases, Mg_3N_2 slowly reacts with O_2 to form MgO due to the elevated temperature.

6.2 Post-thermal treatment powder X-ray diffraction

The post STA products were X-rayed, and the structure has been refined. In all experiments, the resulting powder after the STA measurement was again a mixture of Mg_3N_2 and MgO. However, the obtained refined parameters are slightly different from data previously refined prior STA analysis. The results with selected refinement data will be shown below.

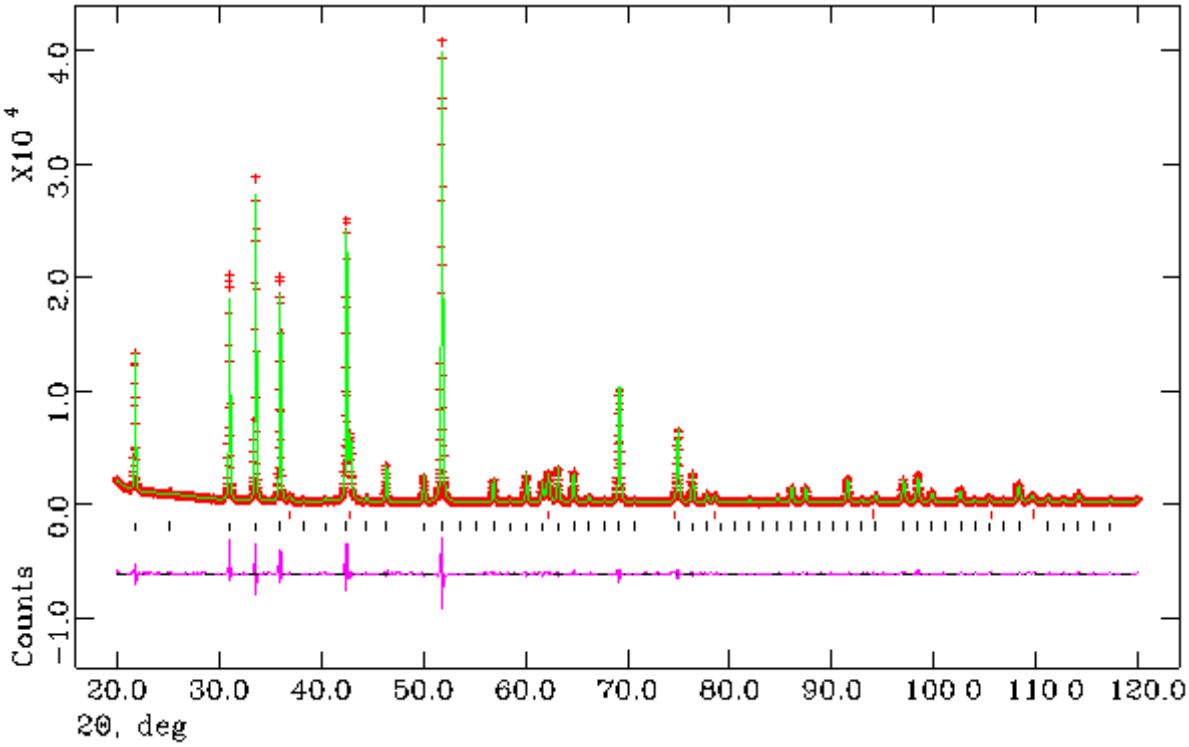

Fig.6.3 Rietveld refinement of the post-STA Mg_3N_2 powder synthesised at 650°C. Observed (crosses), calculated (solid line) and difference curves (bottom line) are shown for comparison. Vertical bars (I) correspond to Bragg positions of Mg_3N_2 (black) and MgO (red) phases respectively from bottom to top.

Table.6.1 *Selected Rietveld refinement data from PXD data of the post-STA Mg_3N_2 powder synthesised at 650°C (sample.1).*

Sample.1 - 650°C			
Phases		Mg_3N_2	MgO
Phase Fraction/wt.%		88.94(1)	11.06(6)
Crystal System		Cubic	Cubic
Space Group		*Ia-3(206)*	*Fm-3m(225)*
Unit cell parameters/Å	a	9.96936(3)	4.21496(8)
	b	9.96936(3)	4.21496(8)
	c	9.96936(3)	4.21496(8)
Volume/$Å^3$		990.836(9)	74.882(4)
Z		48	48
Formula Weight/g		1640.709	162.705
Density ρ_x/gcm^{-3}		2.750	3.608
No of observations		5983	
No of variables		72	
R_{wp}		0.0828	
R_p		0.0652	
χ^2		5.294	

Table.6.2 *Atomic parameters of Mg_3N_2 (sample.1) after thermal analysis.*

Atom/Site	**x**	**y**	**z**	**Occupancy**	**U_{iso} x 100/$Å^2$**
Mg/48e	0.38930(6)	0.15253(5)	0.38212(8)	0.988(1)	1.04(1)
N1/8b	0.25(0)	0.25(0)	0.25(0)	0.166(7)	2.66(10)
N2/24d	-0.03037(16)	0	0.25(0)	0.500(3)	1.58(4)

Table.6.3 *Atomic parameters of MgO (sample.1) after thermal analysis.*

Atom/Site	x	y	z	Occupancy	U_{iso} x 100/Å^2
Mg/4a	0	0	0	1	2.06(5)
O/4b	0.5(0)	0.5(0)	0.5(0)	1	0.77(8)

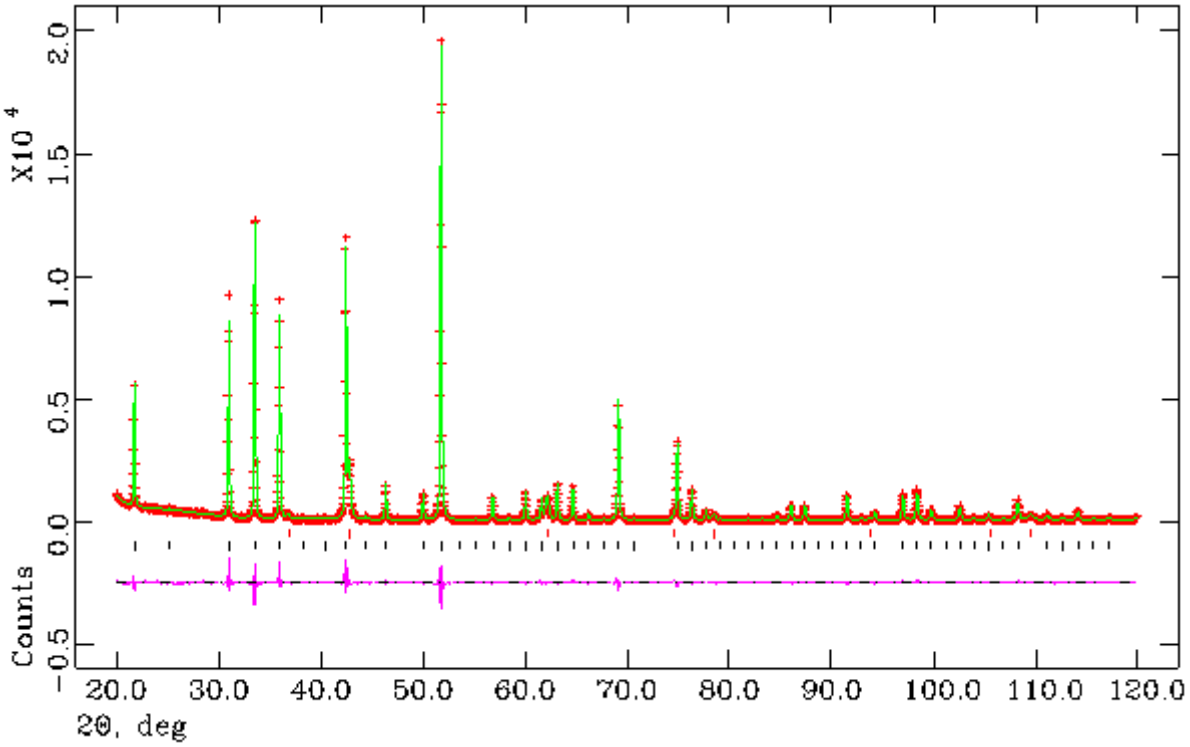

Fig.6.4 Rietveld refinement of the post-STA Mg_3N_2 powder synthesised at 700°C. Observed (crosses), calculated (solid line) and difference curves (bottom line) are shown for comparison. Vertical bars (I) correspond to Bragg positions of Mg_3N_2 (black) and MgO (red) phases respectively from bottom to top.

Table.6.4 *Selected Rietveld refinement data from PXD data of the post-STA Mg_3N_2 powder synthesised at 700°C (sample.2).*

Sample.2 - 700°C			
Phases		Mg_3N_2	MgO
Phase Fraction/wt.%		88.84(2)	11.16(9)
Crystal System		Cubic	Cubic
Space Group		*Ia-3(206)*	*Fm-3m(225)*
Unit cell parameters/Å	a	9.96752(4)	4.2167(1)
	b	9.96752(4)	4.2167(1)
	c	9.96752(4)	4.2167(1)
Volume/$Å^3$		990.28(1)	74.98(1)
Z		48	48
Formula Weight/g		1641.915	159.772
Density ρ_x/gcm^{-3}		2.753	3.538
No of observations		2991	
No of variables		71	
R_{wp}		0.0814	
R_p		0.0622	
χ^2		2.525	

Table.6.5 *Atomic parameters of Mg_3N_2 (sample.2) after thermal analysis.*

Atom/Site	**x**	**y**	**z**	**Occupancy**	**U_{iso} x 100/$Å^2$**
Mg/48e	0.38928(9)	0.15243(8)	0.38204(11)	0.992(1)	1.23(1)
N1/8b	0.25(0)	0.25(0)	0.25(0)	0.166(11)	2.85(14)
N2/24d	-0.03055(22)	0	0.25(0)	0.500(4)	1.50(6)

Table.6.6 *Atomic parameters of MgO (sample.2) after thermal analysis.*

Atom/Site	x	y	z	Occupancy	U_{iso} x 100/Å^2
Mg/4a	0	0	0	1	2.22(7)
O/4b	0.5(0)	0.5(0)	0.5(0)	1	0.87(12)

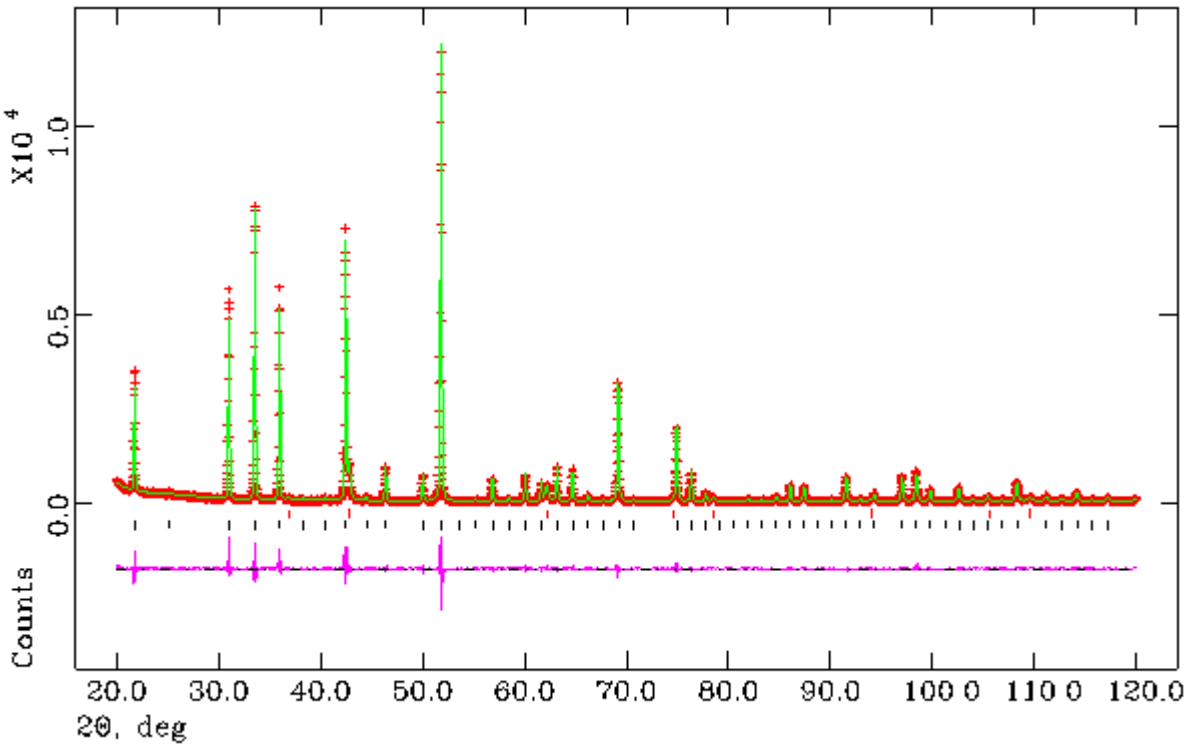

Fig.6.5 Rietveld refinement of the post-STA Mg_3N_2 powder synthesised at 750° C. Observed (crosses), calculated (solid line) and difference curves (bottom line) are shown for comparison. Vertical bars (I) correspond to Bragg positions of Mg_3N_2 (black) and MgO (red) phases respectively from bottom to top.

Table.6.7 *Selected Rietveld refinement data from PXD data of the post-STA Mg_3N_2 powder synthesised at 750°C (sample.3).*

Sample.3 - 750°C			
Phases		Mg_3N_2	MgO
Phase Fraction/wt.%		92.16(1)	7.84(8)
Crystal System		Cubic	Cubic
Space Group		*Ia-3(206)*	*Fm-3m(225)*
Unit cell parameters/Å	a	9.96816(4)	4.2152(1)
	b	9.96816(4)	4.2152(1)
	c	9.96816(4)	4.2152(1)
Volume/$Å^3$		990.47(1)	74.896(8)
Z		48	48
Formula Weight/g		1636.914	163.269
Density ρ_x/gcm^{-3}		2.744	3.620
No of observations		5983	
No of variables		73	
R_{wp}		0.1098	
R_p		0.0843	
χ^2		2.42	

Table.6.8 *Atomic parameters of Mg_3N_2 (sample.3) after thermal analysis.*

Atom/Site	**x**	**y**	**z**	**Occupancy**	**U_{iso} x 100/$Å^2$**
Mg/48e	0.38928(8)	0.15276(7)	0.38201(10)	0.994(1)	0.75(1)
N1/8b	0.25(0)	0.25(0)	0.25(0)	0.166(8)	2.35(12)
N2/24d	-0.02987(20)	0	0.25(0)	0.500(3)	1.25(6)

Table.6.9 *Atomic parameters of MgO (sample.3) after thermal analysis.*

Atom/Site	x	y	z	Occupancy	U_{iso} x 100/Å^2
Mg/4a	0	0	0	1	1.78(8)
O/4b	0.5(0)	0.5(0)	0.5(0)	1	1.39(16)

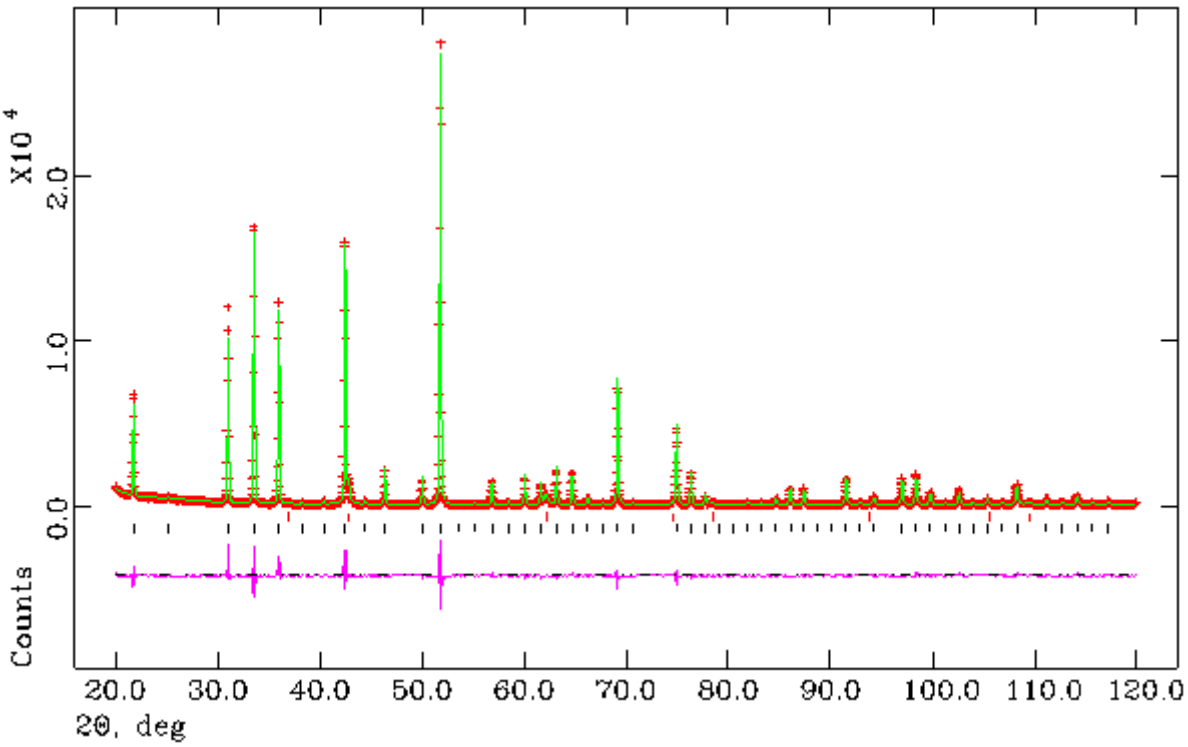

Fig.6.6 Rietveld refinement of the post-STA Mg_3N_2 powder synthesised at 800°C. Observed (crosses), calculated (solid line) and difference curves (bottom line) are shown for comparison. Vertical bars (I) correspond to Bragg positions of Mg_3N_2 (black) and MgO (red) phases respectively from bottom to top.

Table.6.10 *Selected Rietveld refinement data from PXD data of the post-STA Mg_3N_2 powder synthesised at 800°C (sample.4).*

Sample.4 - 800°C			
Phases		Mg_3N_2	MgO
Phase Fraction/wt.%		93.25(1)	6.75(9)
Crystal System		Cubic	Cubic
Space Group		*Ia-3(206)*	*Fm-3m(225)*
Unit cell parameters/Å	a	9.96812(4)	4.2175(2)
	b	9.96812(4)	4.2175(2)
	c	9.96812(4)	4.2175(2)
Volume/$Å^3$		990.46(1)	75.02(1)
Z		48	48
Formula Weight/g		1632.726	163.647
Density ρ_x/gcm^{-3}		2.737	3.622
No of observations		2991	
No of variables		65	
R_{wp}		0.1011	
R_p		0.0774	
χ^2		4.271	

Table.6.11 *Atomic parameters of Mg_3N_2 (sample.4) after thermal analysis.*

Atom/Site	x	y	z	Occupancy	U_{iso} x 100/$Å^2$
Mg/48e	0.38942(10)	0.15263(8)	0.38201(12)	0.996(1)	1.22(1)
N1/8b	0.25(0)	0.25(0)	0.25(0)	0.166(9)	2.52(15)
N2/24d	-0.03011(24)	0	0.25(0)	0.500(4)	1.34(7)

Table.6.12 *Atomic parameters of MgO (sample.4) after thermal analysis.*

Atom/Site	x	y	z	Occupancy	U_{iso} x 100/Å^2
Mg/4a	0	0	0	1	2.39(12)
O/4b	0.5(0)	0.5(0)	0.5(0)	1	1.61(21)

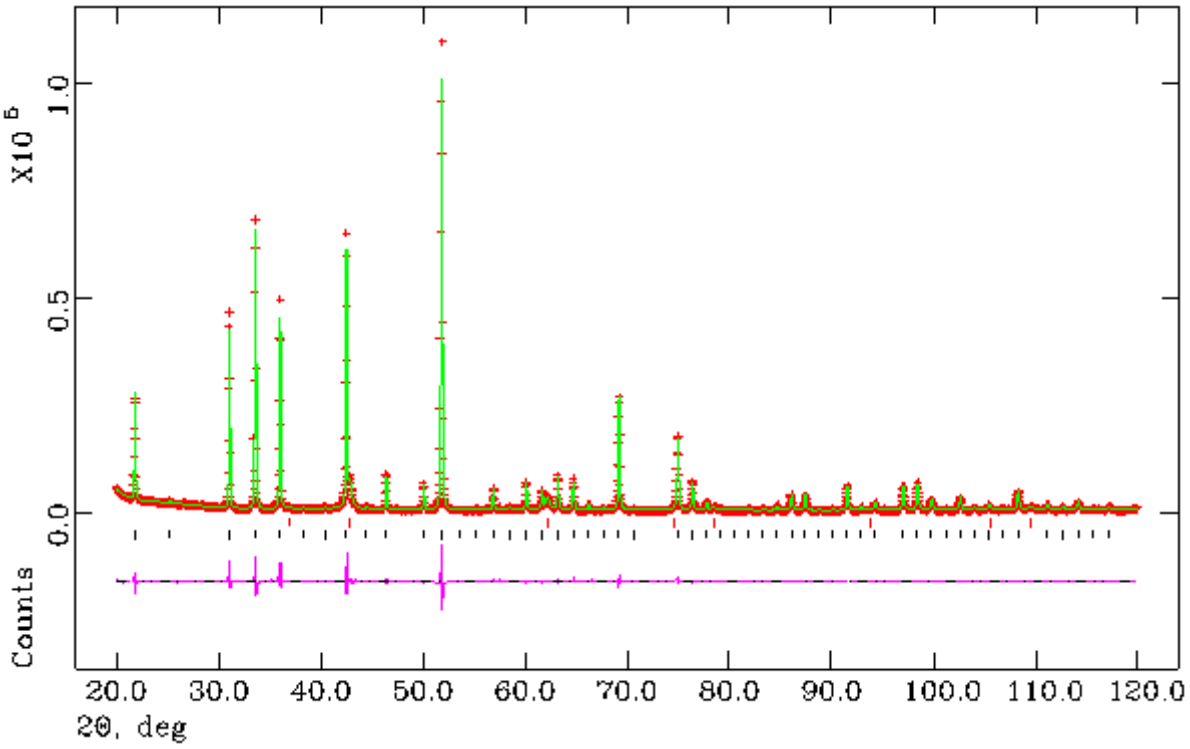

Fig.6.7 Rietveld refinement of the post-STA Mg_3N_2 powder synthesised at 850°C. Observed (crosses), calculated (solid line) and difference curves (bottom line) are shown for comparison. Vertical bars (I) correspond to Bragg positions of Mg_3N_2 (black) and MgO (red) phases respectively from bottom to top.

Table.6.13 *Selected Rietveld refinement data from PXD data of the post-STA Mg_3N_2 powder synthesised at 850°C (sample.5).*

Sample.5 - 850°C			
Phases		Mg_3N_2	MgO
Phase Fraction/wt.%		90.89(3)	9.11(13)
Crystal System		Cubic	Cubic
Space Group		*Ia-3(206)*	*Fm-3m(225)*
Unit cell parameters/Å	a	9.96724(5)	4.2174(2)
	b	9.96724(5)	4.2174(2)
	c	9.96724(5)	4.2174(2)
Volume/$Å^3$		990.20(1)	75.01(1)
Z		48	48
Formula Weight/g		1670.213	165.845
Density ρ_x/gcm^{-3}		2.801	3.671
No of observations		2991	
No of variables		54	
R_{wp}		0.0761	
R_p		0.0595	
χ^2		10.58	

Table.6.14 *Atomic parameters of Mg_3N_2 (sample.5) after thermal analysis.*

Atom/Site	**x**	**y**	**z**	**Occupancy**	**U_{iso} x 100/$Å^2$**
Mg/48e	0.38934(9)	0.15249(8)	0.38216(11)	0.989(1)	0.43(2)
N1/8b	0.25(0)	0.25(0)	0.25(0)	0.166(10)	1.66(16)
N2/24d	-0.03001(23)	0	0.25(0)	0.500(4)	1.49(8)

Table.6.15 *Atomic parameters of MgO (sample.5) after thermal analysis.*

Atom/Site	x	y	z	Occupancy	U_{iso} x 100/Å^2
Mg/4a	0	0	0	1	0.32(10)
O/4b	0.5(0)	0.5(0)	0.5(0)	1	2.08(21)

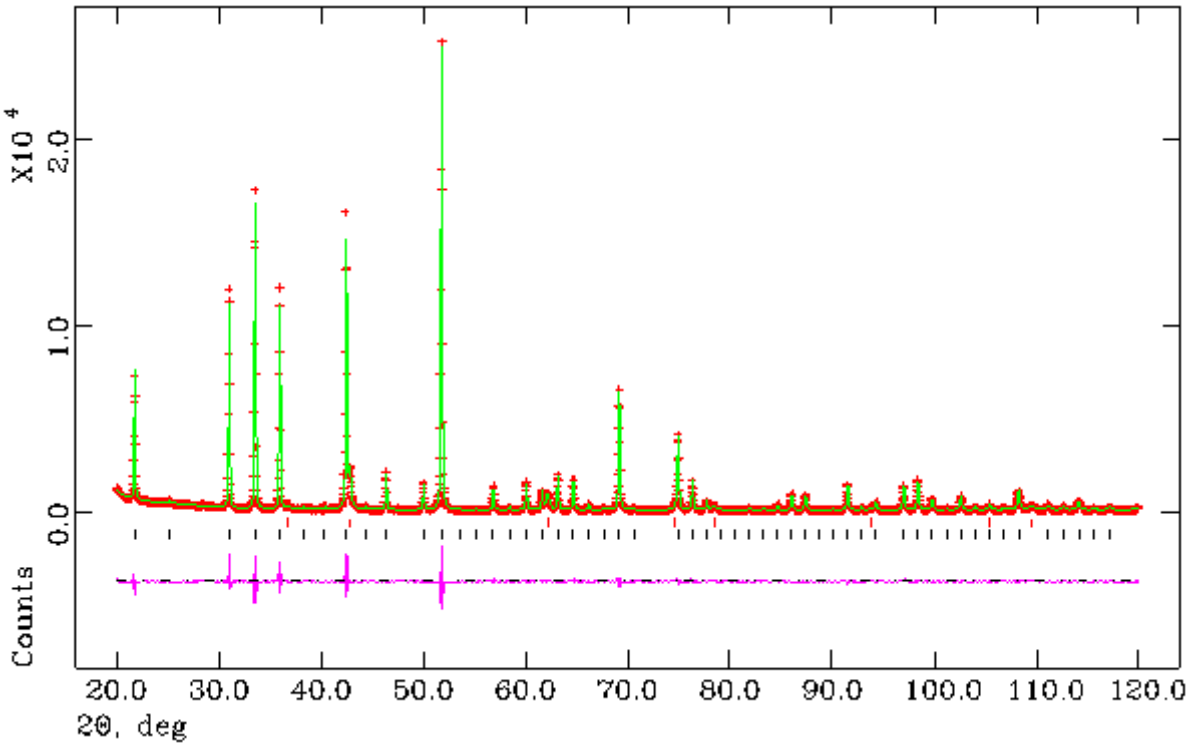

Fig.6.8 Rietveld refinement of the post-STA Mg_3N_2 powder synthesised at 900°C. Observed (crosses), calculated (solid line) and difference curves (bottom line) are shown for comparison. Vertical bars (I) correspond to Bragg positions of Mg_3N_2 (black) and MgO (red) phases respectively from bottom to top.

Table.6.16 *Selected Rietveld refinement data from PXD data of the post-STA Mg_3N_2 powder synthesised at 900°C (sample.6).*

Sample.6 - 900°C			
Phases		Mg_3N_2	MgO
Phase Fraction/wt.%		90.96(4)	9.04(18)
Crystal System		Cubic	Cubic
Space Group		*Ia-3(206)*	*Fm-3m(225)*
Unit cell parameters/Å	a	9.96684(7)	4.2169(2)
	b	9.96684(7)	4.2169(2)
	c	9.96684(7)	4.2169(2)
Volume/$Å^3$		990.08(2)	74.98(1)
Z		48	48
Formula Weight/g		1671.979	162.413
Density ρ_x/gcm^{-3}		2.804	3.597
No of observations		2991	
No of variables		51	
R_{wp}		0.0829	
R_p		0.0660	
χ^2		2.941	

Table.6.17 *Atomic parameters of Mg_3N_2 (sample.6) after thermal analysis.*

Atom/Site	**x**	**y**	**z**	**Occupancy**	**U_{iso} x 100/$Å^2$**
Mg/48e	0.38935(10)	0.15251(9)	0.38216(11)	0.996(2)	0.43(2)
N1/8b	0.25(0)	0.25(0)	0.25(0)	0.166(9)	1.59(18)
N2/24d	-0.02960(24)	0	0.25(0)	0.500(4)	1.53(9)

Table.6.18 *Atomic parameters of MgO (sample.6) after thermal analysis.*

Atom/Site	x	y	z	Occupancy	U_{iso} x 100/Å^2
Mg/4a	0	0	0	1	0.75(13)
O/4b	0.5(0)	0.5(0)	0.5(0)	1	0.99(24)

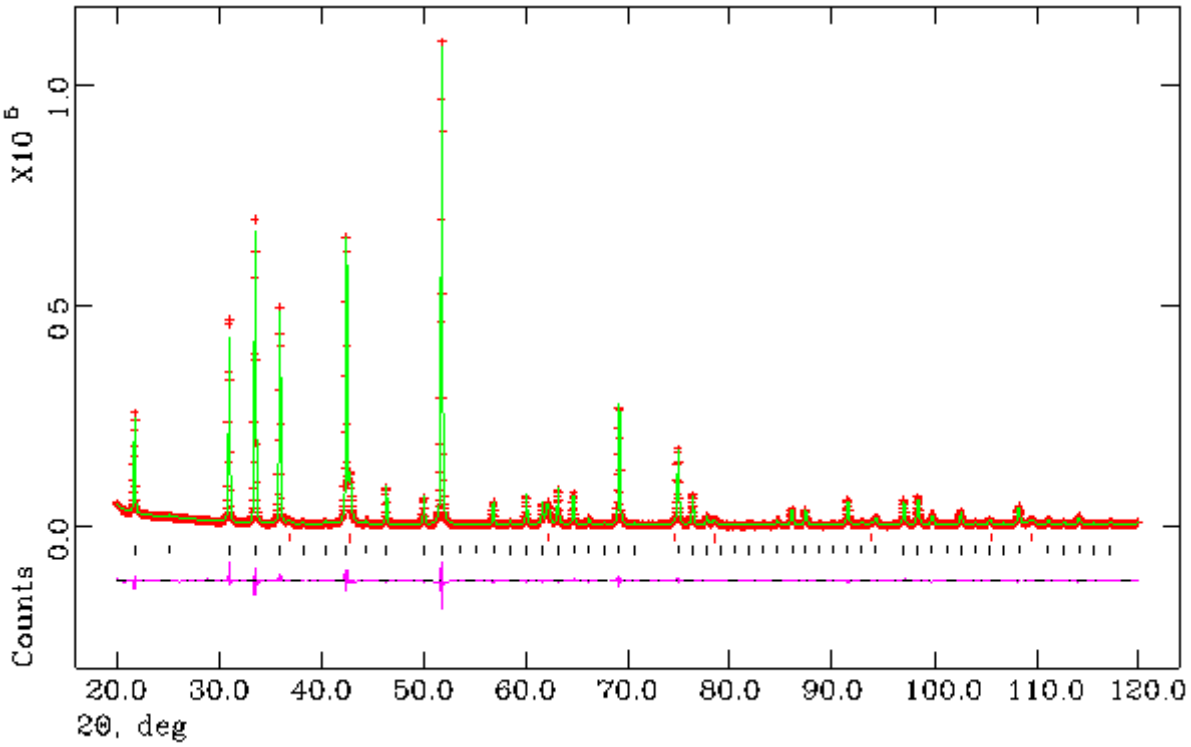

Fig.6.9 Rietveld refinement of the post-STA Mg_3N_2 powder synthesised at 950°C. Observed (crosses), calculated (solid line) and difference curves (bottom line) are shown for comparison. Vertical bars (I) correspond to Bragg positions of Mg_3N_2 (black) and MgO (red) phases respectively from bottom to top.

Table.6.19 *Selected Rietveld refinement data from PXD data of the post-STA Mg_3N_2 powder synthesised at 950°C (sample.7).*

Sample.7 - 950°C			
Phases		Mg_3N_2	MgO
Phase Fraction/wt.%		89.37(2)	10.63(1)
Crystal System		Cubic	Cubic
Space Group		*Ia-3(206)*	*Fm-3m(225)*
Unit cell parameters/Å	a	9.96849(4)	4.2165(1)
	b	9.96849(4)	4.2165(1)
	c	9.96849(4)	4.2165(1)
Volume/$Å^3$		990.57(1)	74.967(8)
Z		48	48
Formula Weight/g		1675.063	164.289
Density ρ_x/gcm^{-3}		2.808	3.639
No of observations		2991	
No of variables		60	
R_{wp}		0.0574	
R_p		0.0438	
χ^2		6.475	

Table.6.20 *Atomic parameters of Mg_3N_2 (sample.7) after thermal analysis.*

Atom/Site	**x**	**y**	**z**	**Occupancy**	**U_{iso} x 100/$Å^2$**
Mg/48e	0.38929(7)	0.15252(6)	0.38222(8)	0.994(2)	0.47(1)
N1/8b	0.25(0)	0.25(0)	0.25(0)	0.166(10)	1.68(11)
N2/24d	-0.02985(17)	0	0.25(0)	0.500(4)	1.67(6)

Table.6.21 *Atomic parameters of MgO (sample.7) after thermal analysis.*

Atom/Site	x	y	z	Occupancy	U_{iso} x 100/Å^2
Mg/4a	0	0	0	1	0.64(6)
O/4b	0.5(0)	0.5(0)	0.5(0)	1	0.95(11)

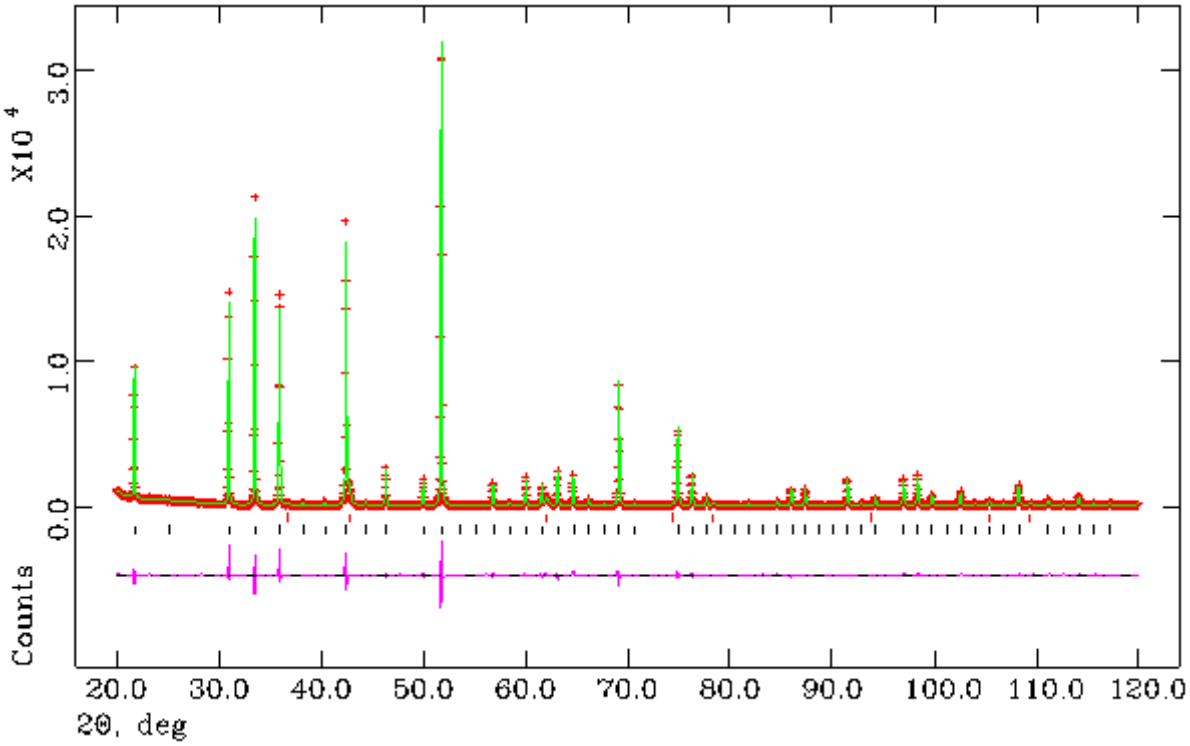

Fig.6.10 Rietveld refinement of the post-STA Mg_3N_2 powder synthesised at 1000°C. Observed (crosses), calculated (solid line) and difference curves (bottom line) are shown for comparison. Vertical bars (I) correspond to Bragg positions of Mg_3N_2 (black) and MgO (red) phases respectively from bottom to top.

Table.6.22 *Selected Rietveld refinement data from PXD data of the post-STA Mg_3N_2 powder synthesised at 1000°C (sample.8).*

Sample.8 - 1000°C			
Phases		Mg_3N_2	MgO
Phase Fraction/wt.%		93.84(1)	6.16(8)
Crystal System		Cubic	Cubic
Space Group		*Ia-3(206)*	*Fm-3m(225)*
Unit cell parameters/Å	a	9.96734(3)	4.2208(2)
	b	9.96734(3)	4.2208(2)
	c	9.96734(3)	4.2208(2)
Volume/$Å^3$		990.233(8)	75.19(1)
Z		48	48
Formula Weight/g		1644.678	177.556
Density ρ_x/gcm^{-3}		2.757	3.919
No of observations		2991	
No of variables		64	
R_{wp}		0.0929	
R_p		0.0736	
χ^2		3.517	

Table.6.23 *Atomic parameters of Mg_3N_2 (sample.8) after thermal analysis.*

Atom/Site	**x**	**y**	**z**	**Occupancy**	**U_{iso} x 100/$Å^2$**
Mg/48e	0.38939(9)	0.15245(8)	0.38211(11)	0.992(1)	1.12(1)
N1/8b	0.25(0)	0.25(0)	0.25(0)	0.166(10)	2.55(14)
N2/24d	-0.03057(22)	0	0.25(0)	0.500(4)	1.65(6)

Table.6.24 *Atomic parameters of MgO (sample.8) after thermal analysis.*

Atom/Site	x	y	z	Occupancy	U_{iso} x 100/Å^2
Mg/4a	0	0	0	1	2.12(12)
O/4b	0.5(0)	0.5(0)	0.5(0)	1	1.76(22)

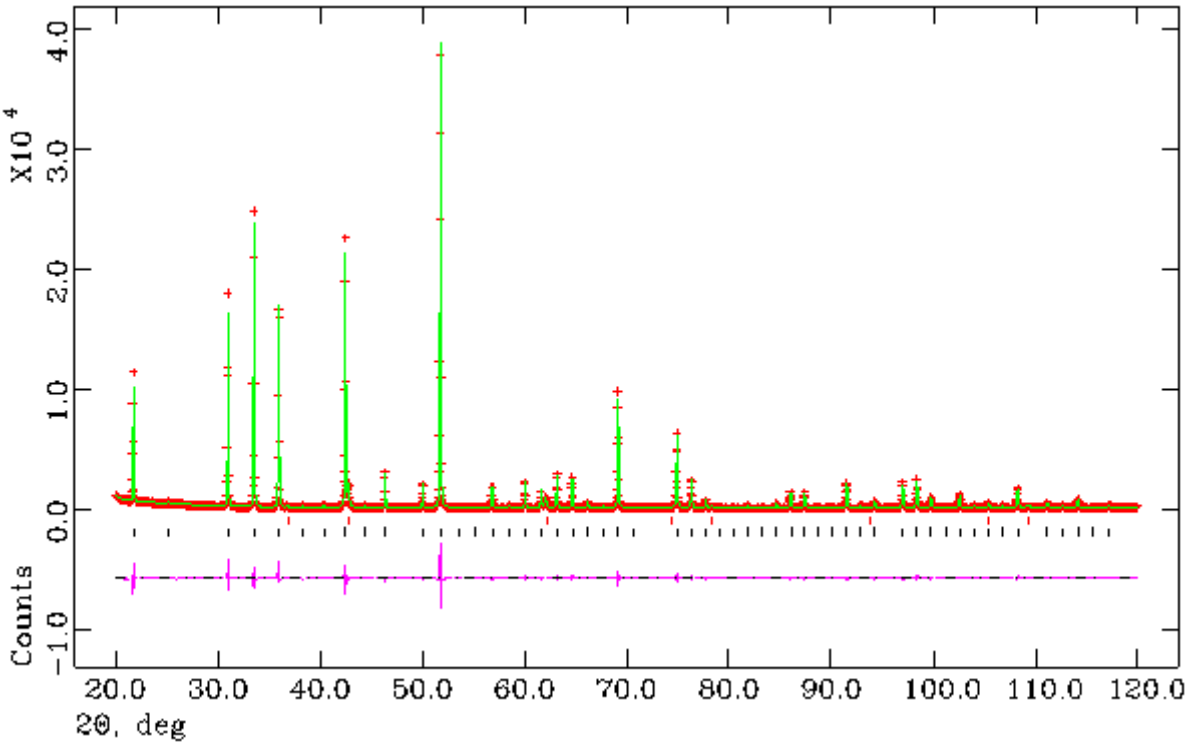

Fig.6.11 Rietveld refinement of the post-STA Mg_3N_2 powder synthesised at 1150°C. Observed (crosses), calculated (solid line) and difference curves (bottom line) are shown for comparison. Vertical bars (I) correspond to Bragg positions of Mg_3N_2 (black) and MgO (red) phases respectively from bottom to top.

Table.6.25 *Selected Rietveld refinement data from PXD data of the post-STA Mg_3N_2 powder synthesised at 1150°C (sample.9).*

Sample.9 - 1150°C			
Phases		Mg_3N_2	MgO
Phase Fraction/wt.%		94.37(1)	5.63(9)
Crystal System		Cubic	Cubic
Space Group		*Ia-3(206)*	*Fm-3m(225)*
Unit cell parameters/Å	a	9.96833(3)	4.2207(1)
	b	9.96833(3)	4.2207(1)
	c	9.96833(3)	4.2207(1)
Volume/$Å^3$		990.528(9)	75.19(1)
Z		48	48
Formula Weight/g		1668.992	162.898
Density ρ_x/gcm^{-3}		2.798	3.597
No of observations		2991	
No of variables		77	
R_{wp}		0.0949	
R_p		0.0738	
χ^2		3.660	

Table.6.26 *Atomic parameters of Mg_3N_2 (sample.9) after thermal analysis.*

Atom/Site	**x**	**y**	**z**	**Occupancy**	**U_{iso} x 100/$Å^2$**
Mg/48e	0.38926(9)	0.15243(8)	0.38219(11)	0.992(1)	0.29(1)
N1/8b	0.25(0)	0.25(0)	0.25(0)	0.166(8)	1.28(14)
N2/24d	-0.03066(24)	0	0.25(0)	0.500(3)	1.27(7)

Table.6.27 *Atomic parameters of MgO (sample.9) after thermal analysis.*

Atom/Site	x	y	z	Occupancy	U_{iso} x 100/Å^2
Mg/4a	0	0	0	1	0.75(12)
O/4b	0.5(0)	0.5(0)	0.5(0)	1	0.31(22)

6.3 References

[1] R. C. Weast. in: CRC Handbook of Chemistry and Physics, 60th ed., CRC press, Boca Raton, FL, 1979, p. B-94.

Conclusions and outlook

The work of this thesis describes very different but necessary aspects in the preparation of inorganic nitride materials. The main accomplishment of this project can be summarised in the following key points:

Reproducible synthetic methods have been established, developed and optimised to obtain high purity of several transition metal nitrides including Mn_4N, NbN, Mo_2N, TaN, ZrN, and Li_3N and Mg_3N_2 binary nitrides.

The phase formation study using X-ray diffraction data, showed that nearly single-phase powders can be obtained. The nonthermal plasma reaction proved to be an efficient route to phase-pure ZrN, a material that is extremely challenging to make at high purity by conventional methods. Rietveld refinement against PXD data confirmed the cubic structure.

Rietveld refinement produces crystallographic data according to a model with an anticipated structure and yields the structural parameters for each crystalline phase identified, and provides a quantitative determination of relative phase concentration. Several statistical factors are generated to evaluate the goodness of the fit to the model; these are defined as reliability (R) factors.

Employing the Rietveld analysis of structure refinement clearly reveals the successful of conventional heating method, which was developed in the synthesis of Li_3N. During the preparation 29.63 % of α-Li_3N has been transformed to β-Li_3N phase.

By using improved processing conditions, it was possible to synthesise Mg_3N_2 fine powders at different nitridation temperatures. Only very low MgO content could be detected with refinement. The formation of magnesium oxide can be explained also the slight gain of weight observed in thermogravimetric analysis (TG). Differential thermal analysis (DTA) showed one clear thermal event for all samples, an endothermic peak occurring around of 550°C.

The study of Mg_3N_2 with SEM showed generally wide range of inhomogeneous morphology. The difference in particle size was distinctly observed and a particle size distribution was generated from a series of SEM images.

Diffuse reflectance UV-Vis spectroscopy (DR-UV-Vis) allows a precise measurement of the optical band gap in powdered nitride materials from the different synthesis categories. The linear fitting of the slope of the Kubelka-Munk function was

performed considering a constant number of points around the respective points of inflection to improve the accuracy of the analysis.

The main findings of this study revealed promising information about the application of synthetic routes in the synthesis of inorganic nitride materials, it can also give further insight into the processes involved to overcome the problem of air sensitivity. However, several other research aspects are worth of further investigation. A number of characterisation methods would be used to investigate the nitrides produced. Getting neutron data for these materials would be ideal to confirm the formation of the phases. It would be of great interest to elucidate and understand in more detail their structures and to suggest potential application of these materials in different fields in the future especially energy storage.